UNIVERSITY OF OKLAHOMA

GRADUATE COLLEGE

OBSERVATION OF THE TRIBOSON PROCESS $pp \to W^{\pm}W^{\mp}\gamma$ AND LIMITS ON ANOMALOUS QUARTIC GAUGE COUPLINGS WITH THE ATLAS DETECTOR

A DISSERTATION

SUBMITTED TO THE GRADUATE FACULTY

in partial fulfillment of the requirements for the

Degree of

DOCTOR OF PHILOSOPHY

By

DANIEL WILBERN
Norman, Oklahoma
2023

OBSERVATION OF THE TRIBOSON PROCESS $pp \to W^{\pm}W^{\mp}\gamma$ AND LIMITS ON ANOMALOUS QUARTIC GAUGE COUPLINGS WITH THE ATLAS DETECTOR

A DISSERTATION APPROVED FOR THE
HOMER L. DODGE DEPARTMENT OF PHYSICS AND ASTRONOMY

BY THE COMMITTEE CONSISTING OF

Dr. Braden Abbott, Chair

Dr. John Stupak

Dr. Chung Kao

Dr. Lloyd Bumm

Dr. Andrew H. Fagg

Acknowledgements

First of all, I would like to thank my PhD advisor Dr. Brad Abbott for his unending support and encouragement over the last six years. I was able to explore and gain valuable experience in a diverse range of subjects, including hardware, software, and data science, under his mentorship. Brad allowed me the freedom to pursue my own research interests while benefitting from his wealth of knowledge and experience. Whenever I got stuck on a hard problem, Brad always had good suggestions for how to proceed. Wherever I end up next in my career, I can only hope for a supervisor with as excellent leadership and expertise as Brad.

Next, I would like to thank my colleagues Joseph Lambert and Dr. Muhammad Alhroob who were my collaborators on the $W^{\pm}W^{\mp}\gamma$ analysis. In addition to all of their hard work without which this thesis would be impossible, I really appreciate our long talks going deep into many physics-related and non-physics-related topics from which I learned so much. I would also like to thank Joe Muse and Marija Marjanović who were my collaborators on the vectorlike leptons analysis where it all started for Joe and I. I could not have asked for better colleagues to learn from and depend on while struggling with the very basics of the ATLAS experiment.

I would like to thank the high energy physics group at the University of Oklahoma, namely Dr. Phil Gutierrez, Dr. John Stupak, Dr. Mike Strauss, and Dr. Pat Skubic, for all of their feedback on my work and help with my presentation skills. I would also like to thank them for their financial support during my studies. Thanks also to Chad Cunningham and Alex Rybicki of the physics department's instrument shop, who taught me everything I know

about hardware. I would also like to thank Dr. Sasha Paramonov, Dr. Marco Trovato, and Dr. Jessica Metcalfe for their supervisory guidance while studying ATLAS detector hardware at Argonne National Laboratory. They are incredible people with incredible jobs. I would also like to thank my PhD advisory committee members for volunteering their time to review my work and help me graduate.

Finally, I would like to thank everyone else who prayed for and encouraged me during these difficult years. My parents Pat and John and my sister Kimmy always believed in me and supported me every step of the way any way they could; I could not be more appreciative. I am also grateful for the exceptional guidance and mentorship of my undergraduate research advisor Dr. Will Tireman at Northern Michigan University who went above and beyond his duty as an undergraduate supervisor to see me succeed. And thanks to my high school physics teacher Mr. Norten and my guidance counselor Dr. Harvey who got me started on this path. And of course many thanks to my friends and (mostly) fellow PhD students Xin, Geo, Fernando, Shadman, Burak, and Andrea (Dr. Dre) for the unforgettable great times we had together.

Table of Contents

Abstract

This thesis presents a search for evidence of $W^{\pm}W^{\mp}\gamma$ production from $p-p$ scattering with $\sqrt{s} = 13$ TeV at the Large Hadron Collider using 140 fb^{-1} of integrated luminosity. The case where the W bosons decay to opposite-flavor light leptons is considered, as other decay channels are dominated by backgrounds. Monte Carlo simulations are used to estimate the contributions of the $W^{\pm}W^{\mp}\gamma$ process as well as various background processes to the $e^{\pm}\mu^{\mp}\gamma$ channel. The contribution to the $e^{\pm}\mu^{\mp}\gamma$ channel of processes with a misidentified or non-prompt photon in the final state are estimated with data-driven methods. A machine learning algorithm trained on Monte Carlo simulations is used to further increase the purity of $W^{\pm}W^{\mp}\gamma$ events in the dataset. A maximum likelihood fit to the binned distribution of the machine learning discriminant is performed to determine the best-fit value of the $W^{\pm}W^{\mp}\gamma$ contribution to the $e^{\pm}\mu^{\mp}\gamma$ channel. From this, the expected $W^{\pm}W^{\mp}\gamma$ production cross section in a fiducial region is determined to be $10.5^{+17\%}_{-11\%}$ (theory) $\pm$ 15% (experiment) fb. The observed cross section in the fiducial region will be measured after the $e^{\pm}\mu^{\mp}\gamma$ dataset is unblinded.

Additionally, to study potential deviations from the Standard Model prediction in the $e^{\pm}\mu^{\mp}\gamma$ channel, the ATLAS run-2 dataset is used to set upper and lower limits at the 95% confidence level on 13 Wilson coefficients of an effective field theory extending the Standard Model with dimension-8 operators. Two methods to restore unitarity to the effective field theory are investigated: the clipping method as well as a dipole form factor model. The dependence of the Wilson coefficients' expected upper and lower limits on these two methods' parameters are presented.

Chapter 1

Introduction

Quantum field theory (QFT) is an invention of the 20^{th} century that provides us with a mathematical framework to study the underlying structure of the universe. Quantum fields are thought to permeate all of spacetime, and the details of the structure and interactions of these fields have been the subject of more than 100 years of research. The Standard Model (SM) of Particle Physics, a quantum field theory based on the two foundational principals of local gauge invariance and spontaneous symmetry breaking, has been subject to the most rigorous experimental tests and most precise parameter measurements in human history. Still, many physicists find it lacking as a fundamental theory of physics for a number of reasons, and so a large research effort is underway for the search of physics phenomena beyond the Standard Model (BSM). This thesis describes a search for evidence of BSM physics in the production of two $W^{\pm}$ bosons in association with a photon, $pp \to W^{\pm}W^{\mp}\gamma$, using the state-of-the-art Large Hadron Collider and the ATLAS detector located at CERN near Geneva, Switzerland.

This thesis describes a measurement of the $W^{\pm}W^{\mp}\gamma$ production cross section and an interpretation of the measurement in the context of an effective field theory (EFT), which is essentially a low-energy approximation of an unknown high-energy BSM theory. The details of the BSM theory are abstracted away by approximation (at the cost of the theory becoming unrenormalizable) allowing us to quantify experimental sensitivity to BSM phenomena without committing to search for a specific BSM model (supersymmetry, axions, etc.). An EFT interpretation also provides a framework for statistically combining the $W^{\pm}W^{\mp}\gamma$ cross section

measurement with other measurements and experiments in the context of BSM searches.

There are 13 independent EFT model parameters that can be experimentally determined from $W^{\pm}W^{\mp}\gamma$ production. Monte Carlo (MC) simulations of $W^{\pm}W^{\mp}\gamma$ production under assumptions of the EFT model, as well as MC simulations of relevant background processes, along with data-driven estimates of background with fake or non-prompt photons, were used to determine limits on the ranges of EFT parameter values consistent with data.

This thesis is organized as follows:

- Chapter 2 gives an overview of the theory of $pp \to W^{\pm}W^{\mp}\gamma$ scattering and EFTs.
- Chapter 3 describes the ATLAS detector, the experimental apparatus used to collect data for this thesis.
- Chapter 4 is an overview of the procedure used to reconstruct physics objects (e.g., electrons, muons, photons) from digitized ATLAS data, as well as the criteria used to select objects and events for this thesis. This chapter also describes the data sample collected by ATLAS as well as Monte Carlo simulation samples used in this thesis.
- Chapter 5 gives an overview of the search for $pp \to W^{\pm}W^{\mp}\gamma$ and cross section measurement.
- Chapter 6 describes the search for evidence of anomalous quartic gauge couplings in $pp \to W^{\pm}W^{\mp}\gamma$ and limits on 13 EFT parameters.

Chapter 2

Theory of $pp \to W^{\pm}W^{\mp}\gamma$ scattering

2.1 The Standard Model

The Standard Model of particle physics is a description of the known fundamental particles of nature, as well as three of the four known fundamental forces of nature. The particles of the SM are listed in Figure 2.1, grouped into families: the quarks, leptons, gauge bosons, along with a single scalar boson. The quarks and leptons are the fundamental elements of matter while the gauge bosons mediate interactions between them.

The strong nuclear force is felt by the quarks and is mediated by massless gluons. The electromagnetic force, mediated by massless photons, is felt by the quarks as well as the electron, muon, tau, and $W^{\pm}$ bosons. The weak nuclear force is felt by all quarks and leptons, and is mediated by the massive $W^{\pm}$ and Z bosons. The recently discovered[1, 2] scalar Higgs boson plays a special role in the SM, allowing for a self-consistent explanation for massive particles. The SM does not include any description of the weakest fundamental force, gravity, which to date is best described by Einstein's theory of general relativity.

The textbook of Schwartz[4] is a good reference for the following material. The SM is a QFT expressed as a Lagrangian, $\mathcal{L}_{\mathcal{SM}}$, formulated to be invariant under certain symmetry groups. A group is defined as a set of elements along with a rule to transform the elements among themselves, i.e., the group must be closed under its transformation rule. A group representation is a mapping of the group elements to linear operators that act on a vector space. In QFT, Fock space is the usual choice of vector space for symmetry group representations

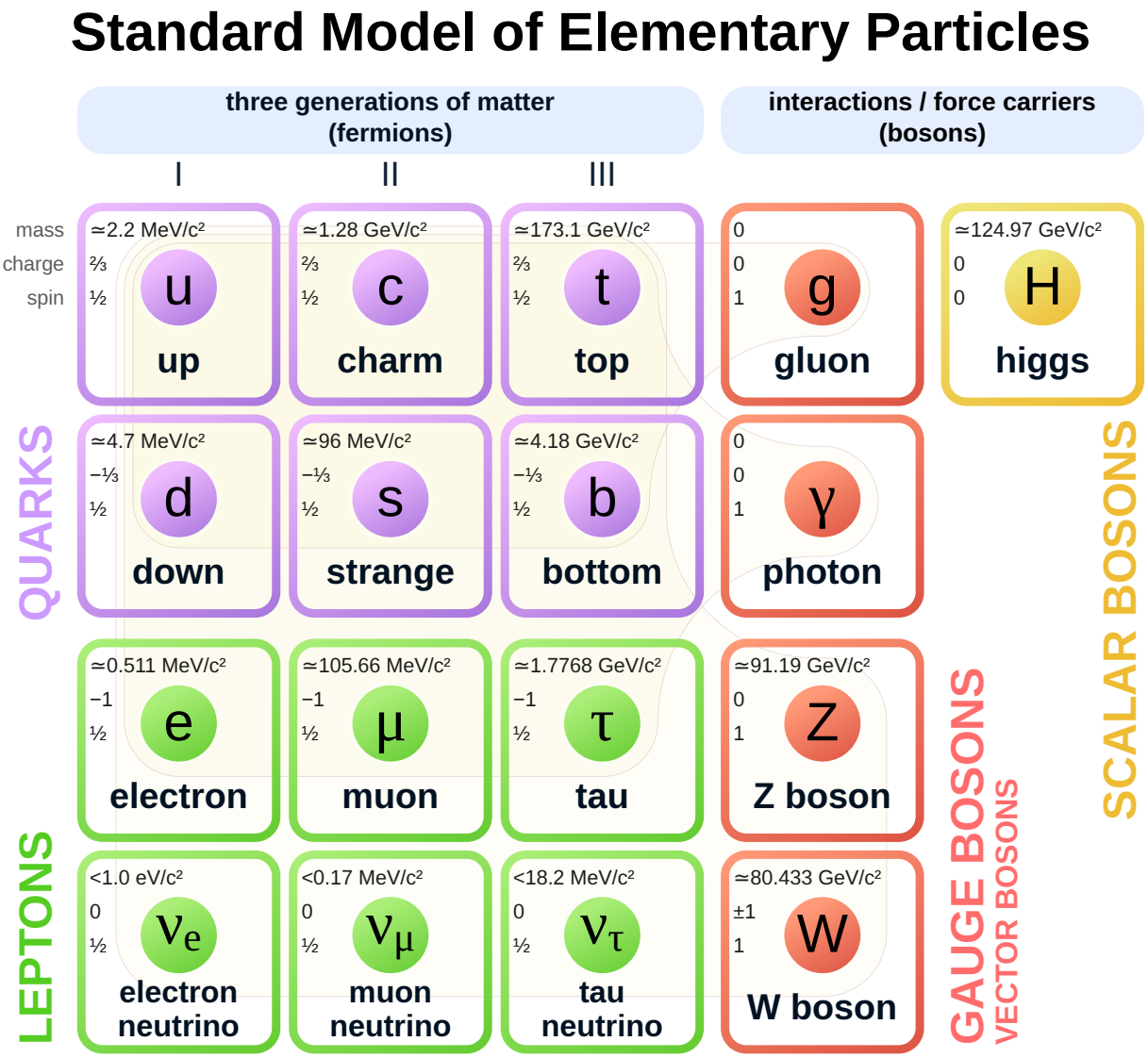

Figure 2.1: Standard Model of Elementary Particles (the leptons are not properly ordered by weak isospin). Source: [3]

to act upon. Vectors in Fock space represent multi-particle states; in Dirac bra-ket notation they are expressed as $|0\rangle$ (vacuum state), $|\psi(k)\rangle$ (single-particle state with momentum k), $|\psi_1(k_1), \psi_2(k_2)\rangle$ (two-particle state), and so on.

The SM Lagrangian is required to be invariant under spacetime translations, as well as Lorentz transformations (boosts and rotations). The linear operators associated with these transformations are representations of the Poincaré group. Furthermore, representations of the Poincaré group are required to be unitary operators in order to interpret inner-products of Fock space vectors as probabilities. In 1939, Wigner[5] showed that irreducible unitary representations of the Poincaré group are infinite-dimensional and uniquely labelled by non-negative quantum numbers m (mass, real-valued) and j (spin, half-integers). Additionally, the SM Lagrangian is subject to local gauge invariance under the symmetry group $SU(3) \otimes SU(2)_{\mathrm{L}} \otimes U(1)$.

The bedrock of the SM is Glashow, Weinberg, and Salam's (GWS) theory of electroweak unification developed in the 1960s[6, 7, 8], based on the theory of local gauge invariance by Yang and Mills[9]. A simpler theory that illustrates local gauge invariance is quantum electrodynamics (QED) under the group $U(1)$. This theory provides a QFT description of the electromagnetic interaction. The Lagrangian is

$$\mathcal{L}_{\mathrm{QED}} = -\frac{1}{4} F^{\mu\nu} F_{\mu\nu} - m\bar{\psi}\psi + i\bar{\psi}\gamma^{\mu}\partial_{\mu}\psi - q\bar{\psi}\gamma^{\mu}A_{\mu}\psi, \tag{2.1}$$

where g is a coupling constant, the $\psi, \bar{\psi}$ are Dirac spinors representing the fermions (quarks and leptons), and A^{μ} is a "gauge" boson representing the photon. The QED Lagrangian is invariant under a $U(1)$ transformation of the spinor fields $\psi \to \psi e^{i\alpha(x)}$ for some spacetime-

dependent $\alpha(x)$ provided the gauge boson transforms in turn as $A^\mu \to A^\mu - g\partial^\mu\alpha(x)$. Requiring the Lagrangian to have the property of local gauge invariance requires the presence of the gauge boson A^μ.

Dirac spinors are composed of left-handed and right-handed components,

$$\psi = \begin{pmatrix} \psi_L \\ \\ \psi_R \end{pmatrix}, \tag{2.2}$$

where "handedness" refers to whether the particle's spin is parallel or antiparallel to its momentum. The weak nuclear force is known to violate parity symmetry, i.e. left-handed and right-handed components of spinor fields transform differently under $SU(2)$. In particular, only the left-handed components of ψ (right-handed components of $\bar{\psi}$) participate in the weak interaction and thus only these components are subject to an $SU(2)$ gauge transformation. This is a problem for the mass term $m\bar{\psi}\psi$ in Equation (2.1), which will not be invariant under $SU(2)_{\mathrm{L}}$ and thus we must assume for now that the fermions are massless.

The GWS theory unifies the electromagnetic and weak interactions by requiring local gauge invariance under $SU(2)_{\mathrm{L}} \otimes U(1)$. The fermion fields transform under this group like

$$\psi_L = \begin{pmatrix} \psi_{1,L} \\ \\ \psi_{2,L} \end{pmatrix} \to \psi_L e^{iY\alpha(x)+i\boldsymbol{\sigma}\cdot\beta(x)/2}, \text{ and} \tag{2.3}$$

$$\psi_R = \psi_R \to \psi_R e^{iY\alpha(x)}, \tag{2.4}$$

where Y ("weak hypercharge") is the charge of the fermion under $U(1)$ and $\boldsymbol{\sigma}$ are the three generators of $SU(2)$ (the Pauli spin matrices). Evidently the electroweak theory contains

four gauge bosons: one corresponding to the generator of $U(1)$ and three corresponding to the generators of $SU(2)$. The Lagrangian for this theory goes like

$$\mathcal{L}_{\text{GWS}} \sim -\frac{1}{4}W_a^{\mu\nu}W^a_{\mu\nu} - \frac{1}{4}B^{\mu\nu}B_{\mu\nu} + \bar{\psi}i\gamma^\mu D_\mu\psi, \tag{2.5}$$

where the covariant derivative $D_\mu = \partial_\mu + ig_W\sigma^a W^a_\mu/2 + ig_Y Y B_\mu$ is analogous to the counteracting transformation of A^μ in QED. W^a_μ $(a = 1, 2, 3)$ are the three gauge bosons required by local gauge invariance under $SU(2)_L$, likewise B_μ is the single gauge boson required for $U(1)$, and the coupling constants g_W and g_Y are parameters of the theory that must be experimentally measured. The field strength tensors $W^a_{\mu\nu} = \partial_\mu W^a_\nu - \partial_\nu W^a_\mu + g_W\epsilon^{abc}W^b_\mu W^c_\nu$ contain a non-Abelian term which describes self-interactions among the bosons, which is quite relevant for the theory of $W^\pm W^\mp\gamma$ production.

To introduce massive fermions and gauge bosons into the theory in a gauge-invariant way (i.e. no Dirac mass terms like $m\bar{\psi}\psi$), Higgs[10] proposed to introduce a scalar $SU(2)$ doublet,

$$\Phi = \begin{pmatrix} \phi^+ \\ \phi^0 \end{pmatrix}, \tag{2.6}$$

with a charged component ϕ^+ and a neutral component ϕ^0, having a quartic potential term in the Lagrangian,

$$\mathcal{L}_{\text{Higgs}} = (D_\mu\Phi)^\dagger(D_\mu\Phi) - \underbrace{\mu^2\Phi^\dagger\Phi - \lambda(\Phi^\dagger\Phi)^2}_{\text{potential}}, \tag{2.7}$$

where D_μ is the electroweak covariant derivative, and $\mu^2 < 0$ and $\lambda > 0$ are parameters that determine the shape of the potential. This potential, sometimes called the sombrero potential

due to its shape, has a local maximum at the origin and a continuum of non-zero global minima. The shape of this potential is shown in Figure 2.2. Perturbative solutions of QFT must be expanded about a stable minimum, so we must make a choice among the infinite minima that spontaneously breaks the $SU(2)$ gauge symmetry. It is conventional to choose a gauge in which the charged component $\phi^+ = 0$, which will leave the $U(1)$ symmetry of the theory unbroken. With this, the neutral component becomes $\phi^0 = (v + H)/\sqrt{2}$ where $v = \langle 0|\phi^0|0\rangle = -\mu^2/2\lambda$, is the vacuum expectation value (vev) and H is a real-valued scalar field which appears in nature as the Higgs boson.

The covariant derivative term in Equation (2.7) can be expanded with

$$\Phi = \frac{1}{\sqrt{2}} \begin{pmatrix} 0 \\ v + H \end{pmatrix}, \tag{2.8}$$

which yields Lagrangian terms representing the $SU(2)$ gauge boson masses due to the vev as well as couplings of the $SU(2)$ gauge bosons to the Higgs boson. These bosons become the physical $W^\pm$ and Z bosons, while the gauge boson associated with the unbroken $U(1)$ symmetry is identified as the massless photon γ. Evidently, the $W^\pm$ and Z bosons "acquire" their mass due to the spontaneously broken symmetry associated with the Φ potential. This is known as the Higgs mechanism.

The fermions $\psi, \bar{\psi}$ of the theory, which were introduced as massless to preserve gauge symmetry under $SU(2)_\mathrm{L}$, also acquire their masses in this way. The left-handed and right-handed components of the fermions are coupled through the scalar field Φ,

$$\mathcal{L}_\mathrm{Yukawa} = g_f \bar{\psi}_R \Phi^\dagger \psi_L + g_f \bar{\psi}_L \Phi \psi_R, \tag{2.9}$$

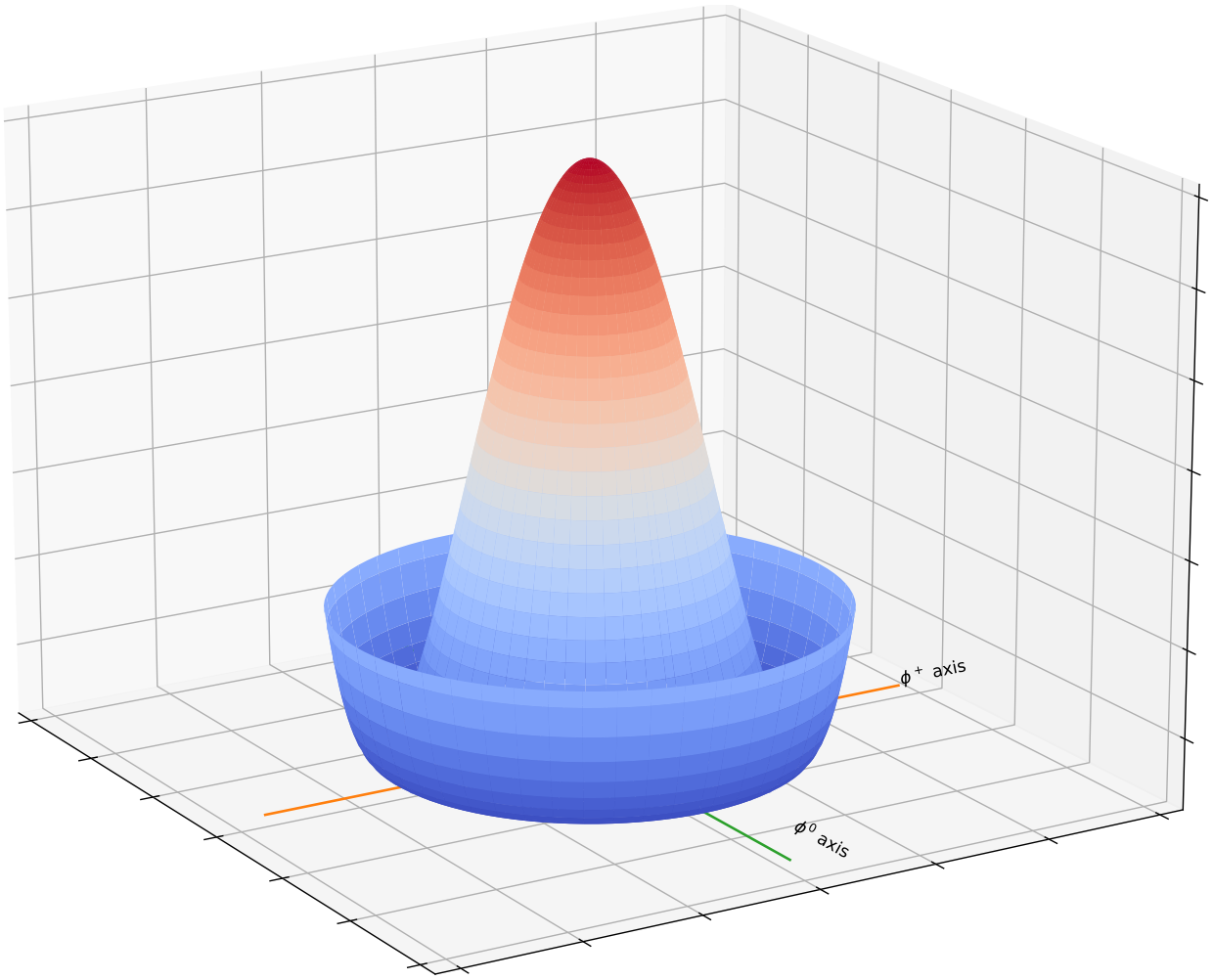

Figure 2.2: The shape of the quartic Higgs potential. Selecting one of the infinite local minima for perturbative expansion spontaneously breaks the $SU(2)_L \otimes U(1)$ gauge invariance of the Lagrangian.

and after $SU(2)$ symmetry is spontaneously broken, the Lagrangian acquires fermion mass terms and fermion-Higgs boson coupling terms.

Additionally, the theory of quantum chromodynamics (QCD) describing the strong nuclear interaction is incorporated into the SM as an $SU(3)$ gauge theory. The Lagrangian is

$$\mathcal{L}_{\text{QCD}} = -\frac{1}{4} G^a_{\mu\nu} G^{\mu\nu}_a + \sum_i \bar{\psi}_i g_{C,i} i\gamma^\mu D_\mu \psi_i, \tag{2.10}$$

where $g_{C,i}$ are coupling constants, ψ_i are the quarks, and the covariant derivative is $D_\mu = \partial_\mu - i g_S T^a G^a_\mu$, where g_S is the strong coupling constant, T^a $(a = 1, 2, \ldots, 8)$ are the generators of $SU(3)$ (Gell-Mann matrices), and G^a_μ are the eight massless gauge bosons (i.e., gluons) associated to the group generators. The summation is over the three quark generations. The gluon field strength tensor has the form

$$G^a_{\mu\nu} = \partial_\mu G^a_\nu - \partial_\nu G^a_\mu - g_S f^{abc} G^b_\mu G^c_\mu, \tag{2.11}$$

which contains the non-Abelian term $g_S f^{abc} G^b_\mu G^c_\mu$, indicating self-interaction among the eight kinds of gluon. This self-interaction is responsible for the phenomenon of confinement, which holds that quarks cannot exist as free particles but must exist in color-neutral bound states known as hadrons.

The full Lagrangian of SM is composed of the pieces discussed in this section: Equations (2.1), (2.7), (2.9) and (2.10). That is,

$$\mathcal{L}_{\text{SM}} = \mathcal{L}_{\text{GWS}} + \mathcal{L}_{\text{Higgs}} + \mathcal{L}_{\text{Yukawa}} + \mathcal{L}_{\text{QCD}}. \tag{2.12}$$

The Lagrangian formulation of the SM can be used to describe systems of interacting particles by computing matrix elements $\langle f|S|i\rangle$ of the scattering matrix S (a.k.a., the S-matrix), where $S = e^{-iHt}$. The S-matrix represents the time evolution operator, evolving the free state $|i\rangle$ into the free state $|f\rangle$. The Hamiltonian H can be derived by taking the Legendre transformation of the Lagrangian. If the S-matrix is unitary, i.e. $S^\dagger S = 1$, then as per the usual rules of quantum mechanics $|\langle f|S|i\rangle|^2$ can be interpreted as the probability for the system to transition from the initial state $|i\rangle$ to the final state $|f\rangle$ under the interactions described in the Lagrangian.

2.2 Effective Field Theories

The theoretical predictions of the SM have been rigorously tested by experiments over the last decades. Figure 2.3 summarizes many cross section measurements made by the ATLAS experiment across many orders of magnitude in diverse final particle states. Despite this success, many physicists consider the SM to be wanting as a complete theory of fundamental particles and their interactions. To name a few concerns:

- There are many unconstrained, arbitrary parameters to the SM that have no theoretical basis and must be experimentally measured,
- The SM lacks a description of gravity, one of the four fundamental forces,
- The particles of the SM (Figure 2.1) cannot account for dark matter, which is thought to be orders of magnitude more abundant than familiar matter,
- It is not known whether neutrinos are their own antiparticles (Majorana neutrinos),

and

- Strong CP problem: QCD permits violation of charge-parity (CP) symmetry, but to date no such violation has been experimentally observed.

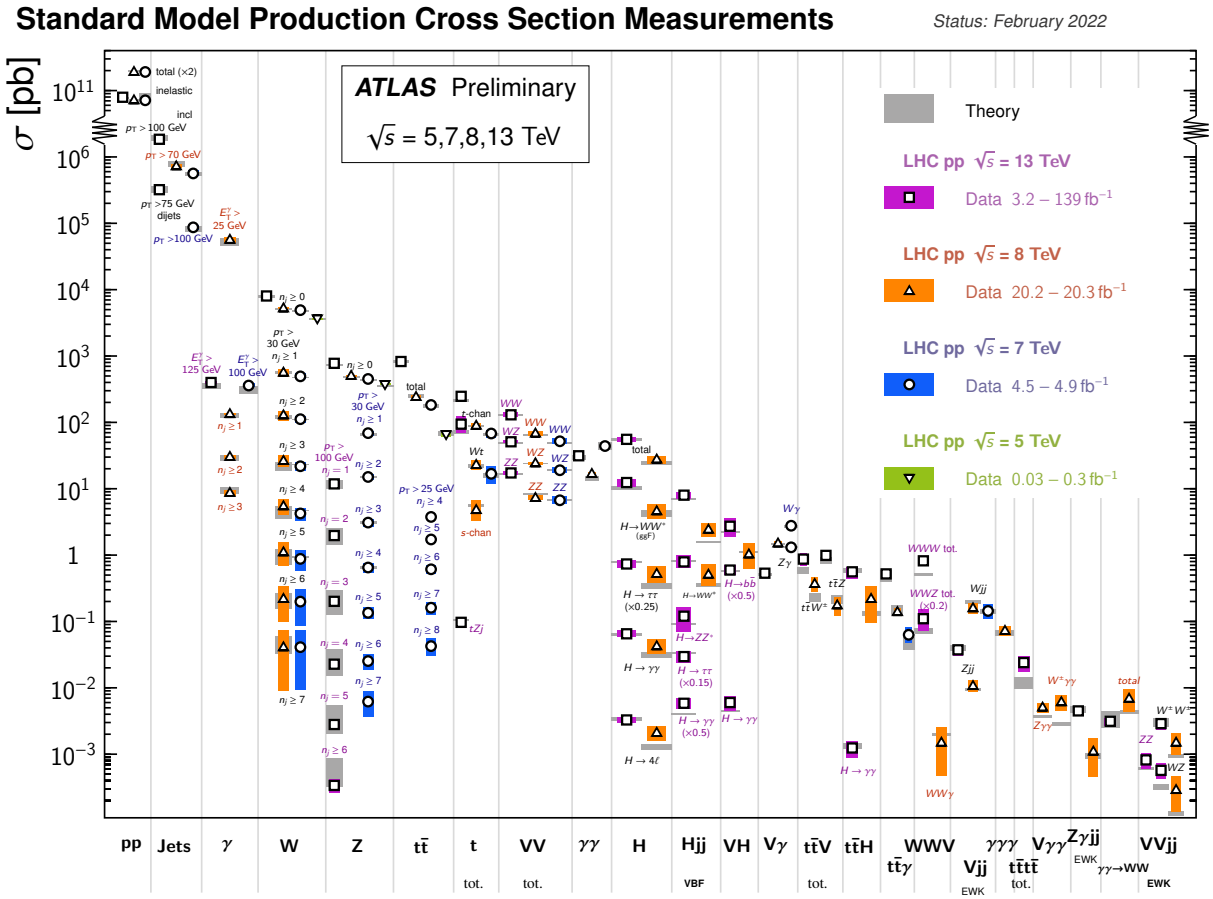

Figure 2.3: Standard Model production cross section measurements by the ATLAS experiment. Triboson production processes like $W^{\pm}W^{\mp}\gamma$ are rarer than diboson production processes by an order of magnitude or more. There is good experimental agreement with theory across many diverse final states. Source: Ref. [11].

In light of these and other issues, physicists have developed many so-called theories of physics beyond the Standard Model (BSM). Many of these theories predict the existence of undiscovered fundamental particles with masses too high to be directly produced at even the world's highest energy collider, the LHC, at 13 TeV center-of-mass energy. If one or more

of these ultra high energy theories are true, we can only hope to uncover evidence of them by making precise measurements of observable quantities predicted by the SM and look for discrepancies between measurement and theory. There are no known discrepancies between the SM and experimental measurements to date, or even any hints as to where potential discrepancies may lie.

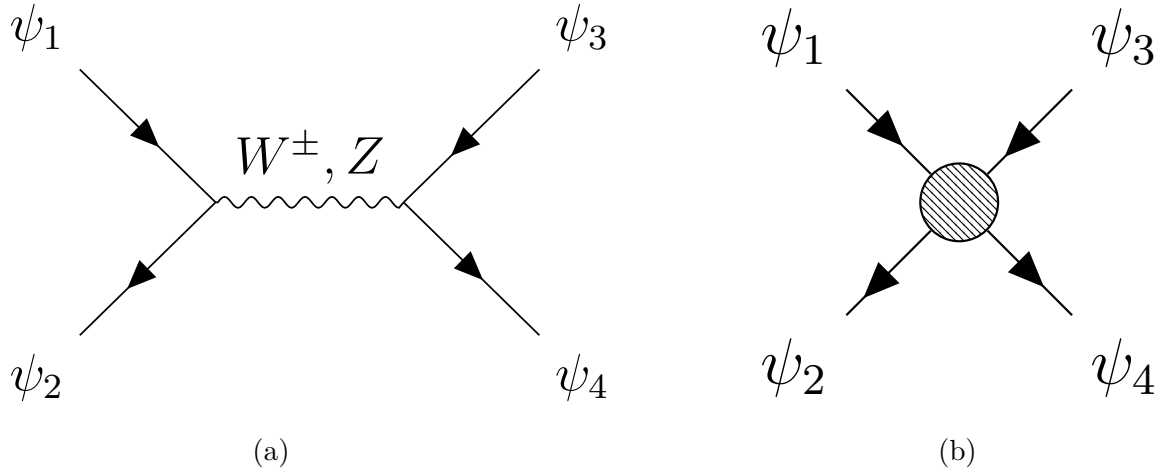

Figure 2.4: (a) Fermion-fermion scattering under the full electroweak theory. (b) Fermion-fermion scattering under Fermi's simplified weak interaction.

Effective field theories (EFTs) provide a general framework for quantifying the sensitivity of BSM theories to experimental measurements. An EFT is essentially a low-energy approximation to a high-energy theory, i.e., if BSM physics has unknown energy scale Λ, then the EFT is only valid when $\sqrt{s} \ll \Lambda$. A canonical example of an EFT is Fermi's theory of weak nuclear interactions developed in 1933[12] decades before the full electroweak theory of Glashow, Weinberg, and Salam was developed[6, 7, 8].

This theory, illustrated in Figure 2.4, approximates weak interactions as a single vertex

that couples four fermions. The Lagrangian can be expressed as

$$\mathcal{L}_{\text{Fermi}} \sim G_F(\bar{\psi}_i\Gamma_1\psi_j)(\bar{\psi}_k\Gamma_1\psi_l) + (\bar{\psi}_i\Gamma_2\psi_j)(\bar{\psi}_k\Gamma_2\psi_l) + \ldots, \tag{2.13}$$

where G_F is the Fermi coupling constant, experimentally measured to be 1.166 $\times 10^{-5}$ GeV^{-2}[13], and the Γ_i, which are in general composed of derivatives ∂^μ and Dirac matrices γ^μ, represent the specific form of the bilinear fermion couplings in the theory. In 1957, Feynman and Gell-Mann[14] incorporated the known parity symmetry violation of the weak interaction into the theory, and arrived at a "$V - A$" form for the bilinear couplings,

$$\mathcal{L}_{\text{Fermi}} \sim \frac{G_F}{4}(\bar{\psi}_i\gamma^\mu(c_V - c_A\gamma^5)\psi_j)(\bar{\psi}_k\gamma^\mu(c_V - c_A\gamma^5)\psi_l), \tag{2.14}$$

where the γ^μ term represents a vector interaction and the $\gamma^\mu\gamma^5$ term represents a parity-violating axial vector interaction. The constants c_V and c_A were experimentally measured and both turned out to have value 1, i.e., parity symmetry is maximally violated by the weak interaction. With this formulation, weak interactions can be studied without introducing the heavy (and undiscovered in Fermi's day) $W^\pm$ and Z bosons into the theory. Fermi developed this theory to explain nuclear beta decay as well as muon decay, which both occur at energy much lower than $\mathcal{O}(M_{W,Z})$.

In a similar way, we can construct an EFT in which the SM is a low-energy approximation to an unknown high-energy BSM theory. The EFT introduces new interactions between the

SM particles in the form of new operators $\mathcal{O}$:

$$\mathcal{L}_{\text{EFT}} = \mathcal{L}_{\text{SM}} + \sum_i \frac{c_i}{\Lambda^2}\mathcal{O}_i^{(6)} + \sum_i \frac{c_i}{\Lambda^4}\mathcal{O}_i^{(8)} + \ldots, \tag{2.15}$$

where Λ is the energy scale of BSM physics and the coupling constants c_i/Λ^n, known as Wilson coefficients in the context of EFT, are parameters of the theory. The vanilla operators of the SM are "dimension-4" operators, i.e., $\mathcal{L}_{\text{SM}}$ has units of GeV^4, while the new operators have higher dimensionality compensated for by the factors of Λ^n in the denominator. Operators with odd dimensionality are known to violate baryon and lepton number[15] and are therefore unphysical.

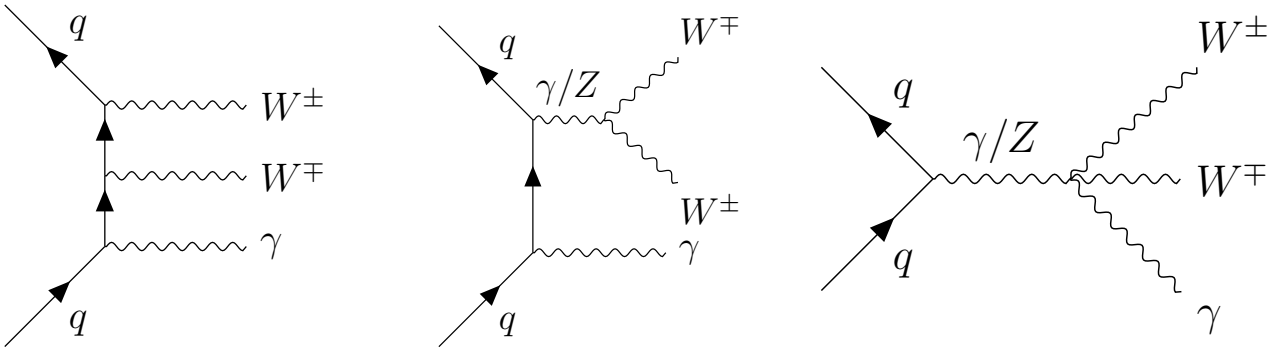

Figure 2.5: (a) $W^\pm W^\mp \gamma$ production with no gauge self-interactions. (b) $W^\pm W^\mp \gamma$ production with trilinear gauge coupling (TGC). (c) $W^\pm W^\mp \gamma$ production with quartic gauge coupling (QGC).

$W^\pm W^\mp \gamma$ production at the LHC can proceed according to the Feynman diagrams in Figure 2.5. The SM includes trilinear and quartic couplings among the electroweak gauge bosons due to the non-Abelian term in the field-strength tensors of Equation (2.5). The new EFT operators of Equation (2.15) can modify the amplitudes of the TGC and QGC diagrams. Operators of dimension-6 can affect both TGCs and QGCs, while operators of dimension-8

only affect QGCs. Wilson coefficients associated with dimension-6 operators have already been constrained tightly by previous analyses of TGCs in diboson processes using LHC run-2 data at $\sqrt{s} = 13$ TeV by ATLAS[16, 17, 18, 19] and CMS[20, 21, 22, 23, 24, 25, 26]. Cross sections of diboson processes are several orders of magnitude higher than for multiboson processes (see Figure 2.3) and therefore a study of dimension-6 operators in $W^{\pm}W^{\mp}\gamma$ production would not be competitive with these previous results. Dimension-8 operators have been studied previously using LHC run-2 data at $\sqrt{s} = 13$ TeV by CMS[27, 28, 29, 30, 31, 32] and and using LHC run-1 data at $\sqrt{s} = 8$ TeV by ATLAS[33, 34, 35, 36, 37, 38, 39] and CMS[40, 41, 42, 43, 44].

Following the parameterization of Eboli[45], we classify the dimension-8 operators into three groups: S-operators containing four covariant derivatives of the scalar field Ψ, M-operators containing a mix of $D_\mu\Phi$ and field-strength tensors, and T-operators containing

field-strength tensors only:

$$
\begin{aligned}
\mathcal{O}_{\mathrm{S0}} &= \left[(D_\mu\Phi)^\dagger D_\nu\Phi\right] \times \left[(D^\mu\Phi)^\dagger D^\nu\Phi\right], \\
\mathcal{O}_{\mathrm{S1}} &= \left[(D_\mu\Phi)^\dagger D^\mu\Phi\right] \times \left[(D_\nu\Phi)^\dagger D^\nu\Phi\right], \\
\mathcal{O}_{\mathrm{S2}} &= \left[(D_\mu\Phi)^\dagger D_\nu\Phi\right] \times \left[(D^\nu\Phi)^\dagger D^\mu\Phi\right], \\
\mathcal{O}_{\mathrm{M0}} &= \mathrm{Tr}\left[\hat{W}_{\mu\nu}\hat{W}^{\mu\nu}\right] \times \left[(D_\beta\Phi)^\dagger D^\beta\Phi\right]; & \mathcal{O}_{\mathrm{M1}} &= \mathrm{Tr}\left[\hat{W}_{\mu\nu}\hat{W}^{\nu\beta}\right] \times \left[(D_\beta\Phi)^\dagger D^\mu\Phi\right], \\
\mathcal{O}_{\mathrm{M2}} &= \left[B_{\mu\nu}B^{\mu\nu}\right] \times \left[(D_\beta\Phi)^\dagger D^\beta\Phi\right]; & \mathcal{O}_{\mathrm{M3}} &= \mathrm{Tr}\left[B_{\mu\nu}B^{\nu\beta}\right] \times \left[(D_\beta\Phi)^\dagger D^\mu\Phi\right], \\
\mathcal{O}_{\mathrm{M4}} &= \left[(D_\mu\Phi)^\dagger \hat{W}_{\beta\nu} D^\mu\Phi\right] \times B^{\beta\nu}; & \mathcal{O}_{\mathrm{M5}} &= \mathrm{Tr}\left[(D_\mu\Phi)^\dagger \hat{W}_{\beta\nu} D^\nu\Phi\right] \times B^{\beta\mu}, \\
\mathcal{O}_{\mathrm{M6}} &= \left[(D_\mu\Phi)^\dagger \hat{W}_{\beta\nu}\hat{W}^{\beta\nu} D^\mu\Phi\right]; & \mathcal{O}_{\mathrm{M7}} &= \mathrm{Tr}\left[(D_\mu\Phi)^\dagger \hat{W}_{\beta\nu}\hat{W}^{\beta\mu} D^\nu\Phi\right], \\
\mathcal{O}_{\mathrm{T0}} &= \mathrm{Tr}\left[\hat{W}_{\alpha\mu}\hat{W}^{\mu\beta}\right] \times \mathrm{Tr}\left[\hat{W}_{\alpha\beta}\hat{W}^{\alpha\beta}\right]; & \mathcal{O}_{\mathrm{T1}} &= \mathrm{Tr}\left[\hat{W}_{\alpha\nu}\hat{W}^{\mu\beta}\right] \times \mathrm{Tr}\left[\hat{W}_{\mu\beta}\hat{W}^{\alpha\nu}\right], \\
\mathcal{O}_{\mathrm{T2}} &= \mathrm{Tr}\left[\hat{W}_{\alpha\mu}\hat{W}^{\mu\beta}\right] \times \mathrm{Tr}\left[\hat{W}_{\beta\nu}\hat{W}^{\nu\alpha}\right]; & \mathcal{O}_{\mathrm{T5}} &= \mathrm{Tr}\left[\hat{W}_{\mu\nu}\hat{W}^{\mu\nu}\right] \times B_{\alpha\beta}B^{\alpha\beta}, \\
\mathcal{O}_{\mathrm{T6}} &= \mathrm{Tr}\left[\hat{W}_{\alpha\nu}\hat{W}^{\mu\beta}\right] \times B_{\mu\beta}B^{\alpha\nu}; & \mathcal{O}_{\mathrm{T7}} &= \mathrm{Tr}\left[\hat{W}_{\alpha\mu}\hat{W}^{\mu\beta}\right] \times B_{\beta\nu}B^{\nu\alpha}, \\
\mathcal{O}_{\mathrm{T8}} &= B_{\mu\nu}B^{\mu\nu}B_{\alpha\beta}B^{\alpha\beta}; & \mathcal{O}_{\mathrm{T9}} &= B_{\alpha\mu}B^{\mu\beta}B_{\beta\nu}B^{\nu\alpha},
\end{aligned}
\tag{2.16}
$$

where $\hat{W}_{\mu\nu} = \sum_j W^j_{\mu\nu}\frac{\sigma^j}{2}$ (σ^j are the Pauli spin matrices). It turns out that two of the operators as originally formulated are redundant: $\mathcal{O}_{\mathrm{S2}}$ is the Hermitian conjugate of $\mathcal{O}_{\mathrm{S0}}$ and $\mathcal{O}_{\mathrm{M6}} = \frac{1}{2}\mathcal{O}_{\mathrm{M0}}$. The $WW\gamma\gamma$ and $WWZ\gamma$ QGC vertices relevant for $W^\pm W^\mp\gamma$ production is affected by 13 of these operators: $\mathcal{O}_{\mathrm{M0}}$, $\mathcal{O}_{\mathrm{M1}}$, $\mathcal{O}_{\mathrm{M2}}$, $\mathcal{O}_{\mathrm{M3}}$, $\mathcal{O}_{\mathrm{M4}}$, $\mathcal{O}_{\mathrm{M5}}$, $\mathcal{O}_{\mathrm{M7}}$, $\mathcal{O}_{\mathrm{T0}}$, $\mathcal{O}_{\mathrm{T1}}$, $\mathcal{O}_{\mathrm{T2}}$, $\mathcal{O}_{\mathrm{T5}}$, $\mathcal{O}_{\mathrm{T6}}$, and $\mathcal{O}_{\mathrm{T7}}$. In this thesis we seek to set experimental limits on the 13 associated Wilson coefficients.

EFTs with higher dimension operators are not UV complete, in particular generalizing the low-energy EFT to arbitrarily high energy results in a theory with a non-unitary S-matrix.

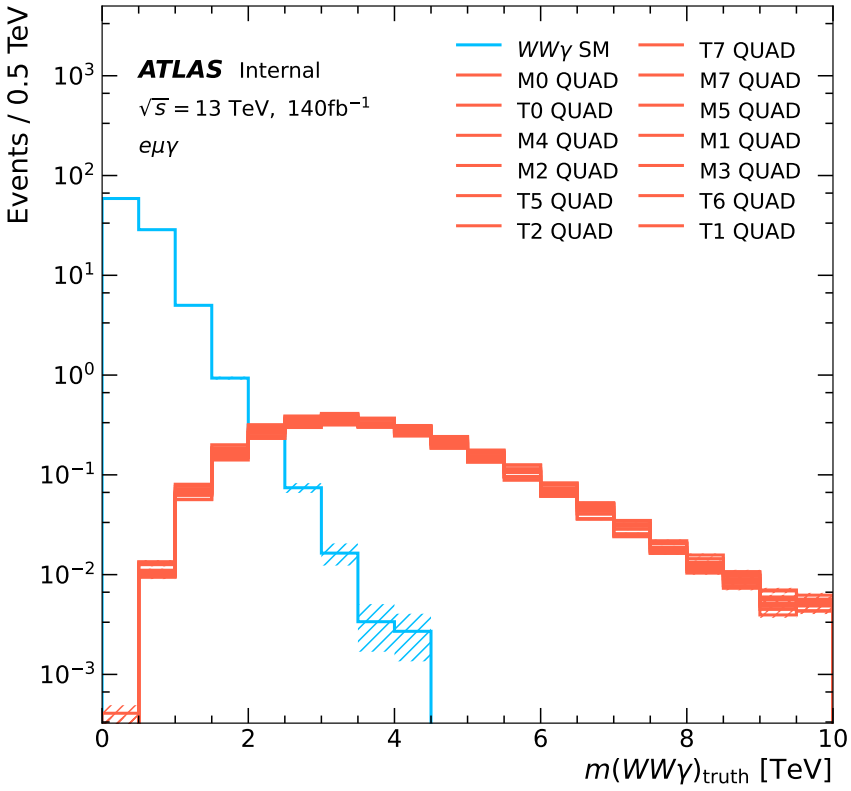

Figure 2.6: Distribution of $m(W^{\pm}W^{\mp}\gamma)$ in the MC samples (see Section 4.3) at truth-level for $e^{\pm}\mu^{\mp}\gamma$ events (see Section 4.2 for the full region definition). This quantity is a proxy for $\sqrt{s}$ at parton-level.

This is not surprising, considering that the EFT is a perturbation series in the BSM energy scale Λ. However, as it turns out, unitarity is violated at sufficiently high $\sqrt{s}$ even for $\sqrt{s} < \Lambda$. This is because of $\sqrt{s}$ dependence in the matrix element when expanded in partial waves[46]. This can be seen in Figure 2.6 where $m(W^{\pm}W^{\mp}\gamma)$ drops off much more slowly for EFT events compared to SM events. Conservation of momentum requires $m(W^{\pm}W^{\mp}\gamma) = \sqrt{s}$ of the underlying partons. It is not known by what mechanism nature preserves unitarity of these operators, so to restore unitarity to the EFT we must impose some additional model-dependence. In Section 6.4 two methods of restoring unitarity to the theory are incorporated into the experimental limits on Wilson coefficients.

In general, higher values of Wilson coefficient result in unitarity violation at lower $\sqrt{s}$. In Ref. [46] unitarity bounds on dimension-8 Wilson coefficients are computed by expanding the matrix element for $VV \to VV$ scattering in partial waves and imposing the optical theorem on the leading-order term. Their results are tabulated in Table 2.1 along with the unitarity bound evaluated at $\sqrt{s} = 3$ TeV, which is near the peak of the $m(W^{\pm}W^{\mp}\gamma)$ distributions for the EFT distributions in Figure 2.6.

Wilson coefficient	Unitarity bound	Bound @ $\sqrt{s} = 3$ TeV
$\lvert f_{S0}\rvert$	$32\pi s^{-2}$	1.24 TeV^4/Λ^4
$\lvert f_{S1}\rvert$	$\frac{96}{7}\pi s^{-2}$	0.532 TeV^4/Λ^4
$\lvert f_{S2}\rvert$	$\frac{96}{5}\pi s^{-2}$	0.744 TeV^4/Λ^4
$\lvert f_{M0}\rvert$	$\frac{32}{\sqrt{6}}\pi s^{-2}$	0.506 TeV^4/Λ^4
$\lvert f_{M1}\rvert$	$\frac{128}{\sqrt{6}}\pi s^{-2}$	2.03 TeV^4/Λ^4
$\lvert f_{M2}\rvert$	$\frac{16}{\sqrt{2}}\pi s^{-2}$	0.439 TeV^4/Λ^4
$\lvert f_{M3}\rvert$	$\frac{64}{\sqrt{2}}\pi s^{-2}$	1.75 TeV^4/Λ^4
$\lvert f_{M4}\rvert$	$32\pi s^{-2}$	1.24 TeV^4/Λ^4
$\lvert f_{M5}\rvert$	$64\pi s^{-2}$	2.48 TeV^4/Λ^4
$\lvert f_{M7}\rvert$	$\frac{256}{\sqrt{6}}\pi s^{-2}$	4.05 TeV^4/Λ^4
$\lvert f_{T0}\rvert$	$\frac{12}{5}\pi s^{-2}$	0.0930 TeV^4/Λ^4
$\lvert f_{T1}\rvert$	$\frac{24}{5}\pi s^{-2}$	0.186 TeV^4/Λ^4
$\lvert f_{T2}\rvert$	$\frac{96}{13}\pi s^{-2}$	0.286 TeV^4/Λ^4
$\lvert f_{T5}\rvert$	$\frac{8}{\sqrt{3}}\pi s^{-2}$	0.179 TeV^4/Λ^4
$\lvert f_{T6}\rvert$	$\frac{48}{7}\pi s^{-2}$	0.266 TeV^4/Λ^4
$\lvert f_{T7}\rvert$	$\frac{32}{\sqrt{3}}\pi s^{-2}$	0.229 TeV^4/Λ^4
$\lvert f_{T8}\rvert$	$\frac{3}{2}\pi s^{-2}$	0.058 TeV^4/Λ^4
$\lvert f_{T9}\rvert$	$\frac{24}{7}\pi s^{-2}$	0.133 TeV^4/Λ^4

Table 2.1: Unitarity bounds of dimension-8 EFT operators at $\sqrt{s} = 3$ TeV. Source: Ref.[46].

Chapter 3

Experimental Apparatus

The ATLAS experiment is a large general-purpose particle detector built and operated by a collaboration of ∼5500 people including ∼2900 publishing authors from 183 institutions in 38 countries (as of 2018)[47]. The experiment is located at CERN near Geneva, Switzerland. The ATLAS detector collects data about high energy proton-proton collisions delivered by the Large Hadron Collider (LHC), and the data is analyzed to experimentally test the Standard Model of particle physics and beyond.

3.1 The Large Hadron Collider

The LHC[48] is the largest and highest energy particle accelerator in the world. It is a circular accelerator of circumference 27 km located 50-175 m underground in the vicinity of Geneva, Switzerland and extends across the border into France. The LHC consists of two counter-propagating proton beams that collide at eight designated interaction points, four of which are occupied by the ATLAS, CMS, LHCb, and ALICE experiments. The LHC has completed two data-taking runs to date: run-1 from 2008-2013 with $\sqrt{s} = 8$ TeV and run-2 from 2015-2018 with $\sqrt{s} = 13$ TeV. LHC run-3 began in 2022 with $\sqrt{s} = 13.6$ TeV and is expected to conclude in 2026, and LHC run-4 is planned to start in 2029 at $\sqrt{s} = 14$ TeV with significantly higher luminosity.

Refer to Figure 3.1 for an overview of the CERN accelerator complex. Protons from a bottle of hydrogen are first accelerated to energy 450 GeV by smaller accelerators in the complex and are then injected into the LHC, which accelerates them to the target energy of

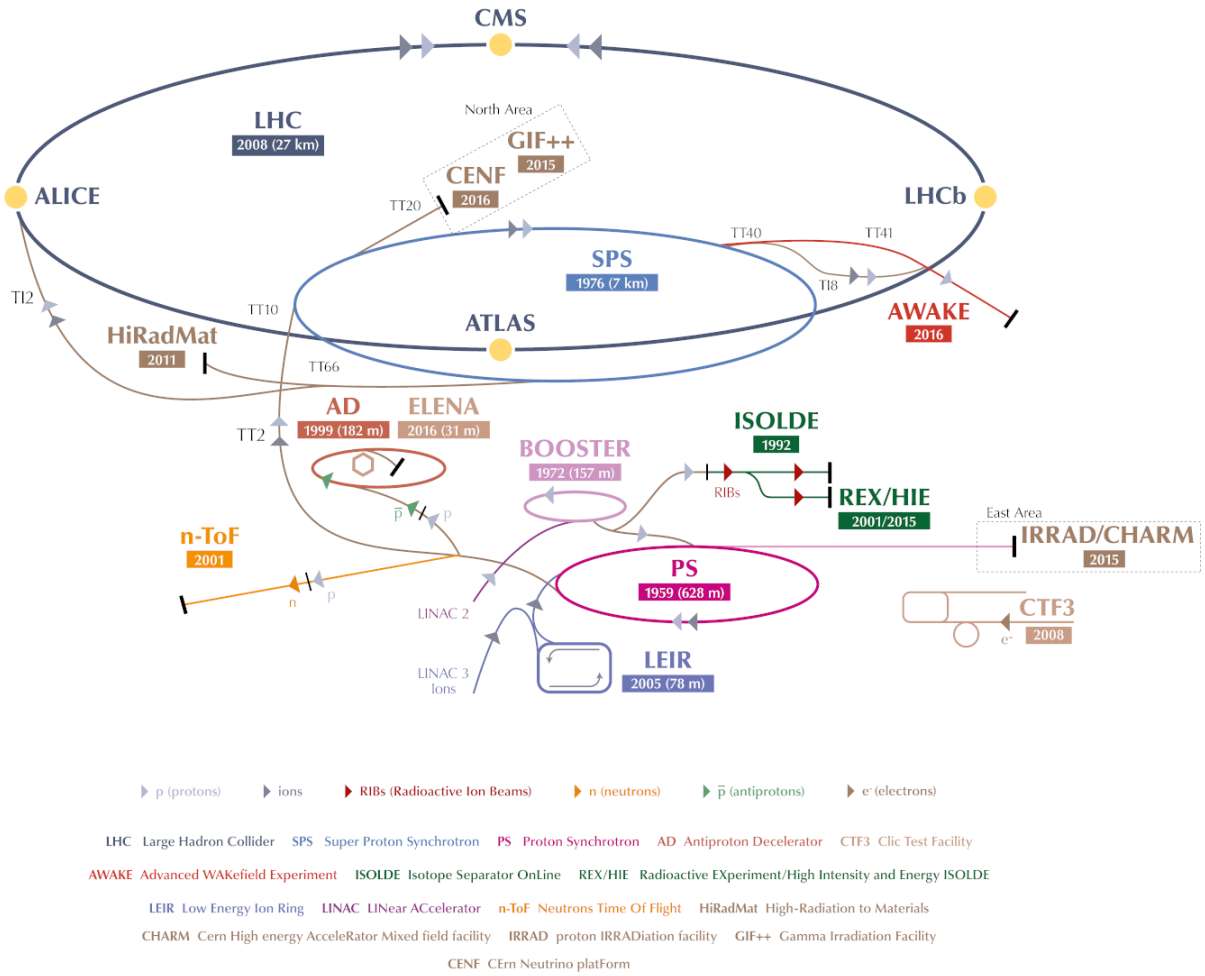

Figure 3.1: The CERN accelerator complex. Source: Ref. [49].

6.5 TeV. Powerful electric fields oscillating in RF cavities with frequency 400 MHz accelerate the protons with several megavolts, and the beams are steered around the circular ring by powerful superconducting NbTi dipole magnets with magnetic fields of over 8 T. In total there are 1,232 dipole magnets along the ring, each ∼15 m long and operated at a temperature of 1.9 K. The LHC and its four detectors consume about 120 MW of power while running, which is about 20% of the power consumed by the nearby city of Geneva.

The LHC delivers protons to the experiments in bunches of $\mathcal{O}(10^{11})$ at a rate of 40 MHz, or every 25 ns. This event rate is related to the cross section σ and instantaneous luminosity

$\mathcal{L}$ as

$$\frac{dN}{dt} = \sigma\mathcal{L}. \tag{3.1}$$

The luminosity quantifies the "intensity" of the LHC and can be studied as a function of beam parameters. The cross section is essentially the probability for $p-p$ collisions to occur. The instantaneous luminosity delivered to the ATLAS experiment for run-1 and run-2 data-taking years is plotted in Figure 3.2. LHC run-2 lasted for three years and in this time, a total integrated luminosity of $\int \mathcal{L}dt = 140$ fb^{-1} was delivered to the ATLAS experiment. Typically, $\sim$30 proton-proton collisions occur per bunch crossing in the ATLAS detector (see Figure 3.3). Usually only one collision per bunch crossing is interesting (the "hard scattering") and the others are referred to as pileup.

3.2 The ATLAS Detector

The ATLAS detector[52] is one of the two "general-purpose" detectors recording data about $p-p$ collisions provided by the LHC; it is pictured in Figure 3.4. The cylinder-shaped detector is 44 m long, 25 m wide, 25 m tall, weights 7,000 tonnes, and is located 100 m underground near CERN's main site in Switzerland. The detector is comprised of four main subsystems: the inner tracker, the electromagnetic calorimeter, the hadronic calorimeter, and the muon spectrometer. The products of $p-p$ collisions propagate through these layers and have their properties measured.

One of the main functions of the ATLAS detector is to measure the four-momentum of particles produced in $p-p$ collisions. The ATLAS experiment uses a spherical polar coordinate system in which particles' four-momenta are parameterized by $(p_{\mathrm{T}}, \eta, \phi, E)$ where p_{T} is the

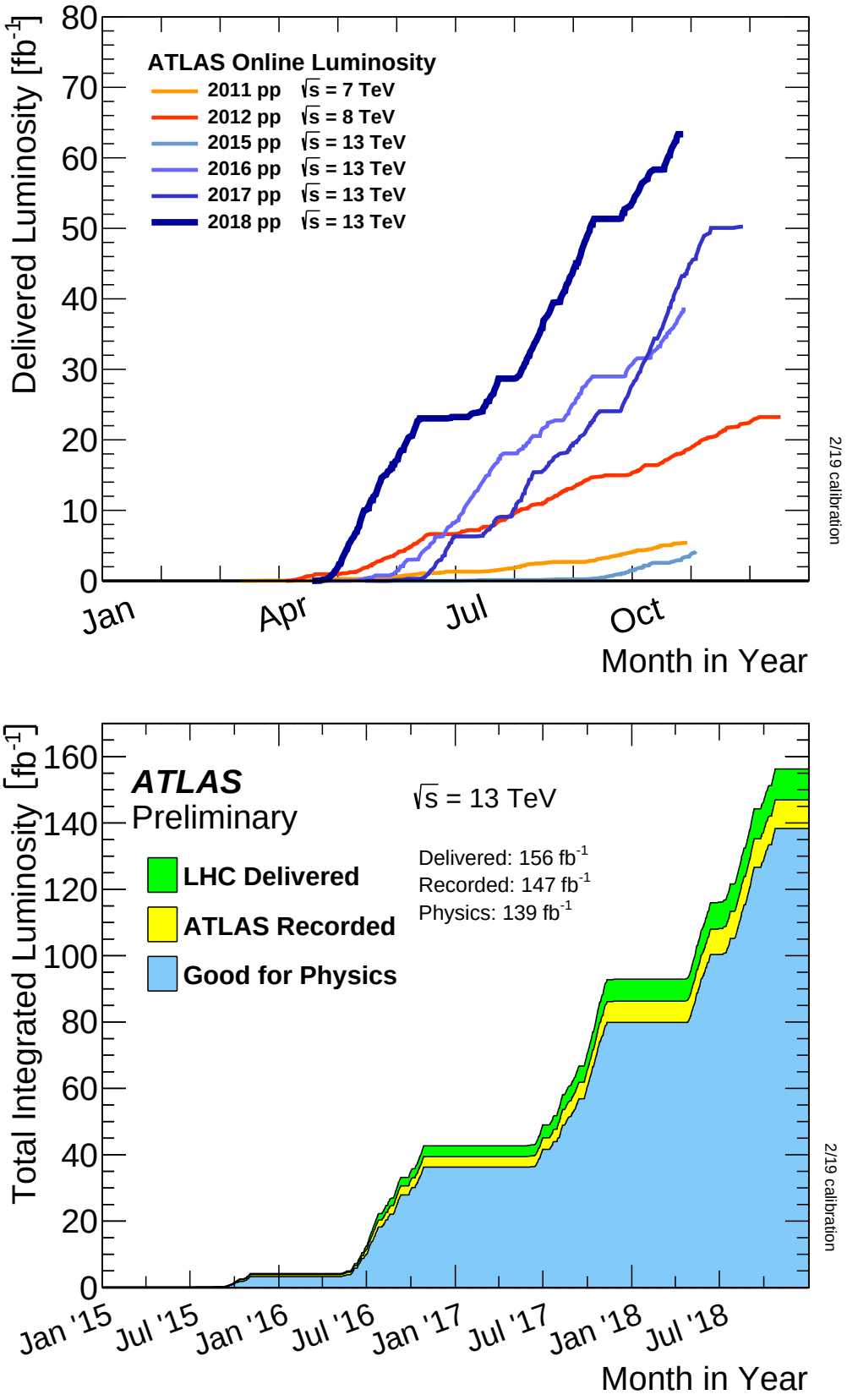

Figure 3.2: Instantaneous luminosity delivered to ATLAS per data-taking year. The full run-2 dataset recorded by ATLAS comprises about 140 fb^{-1} of integrated luminosity. Source: Ref. [50].

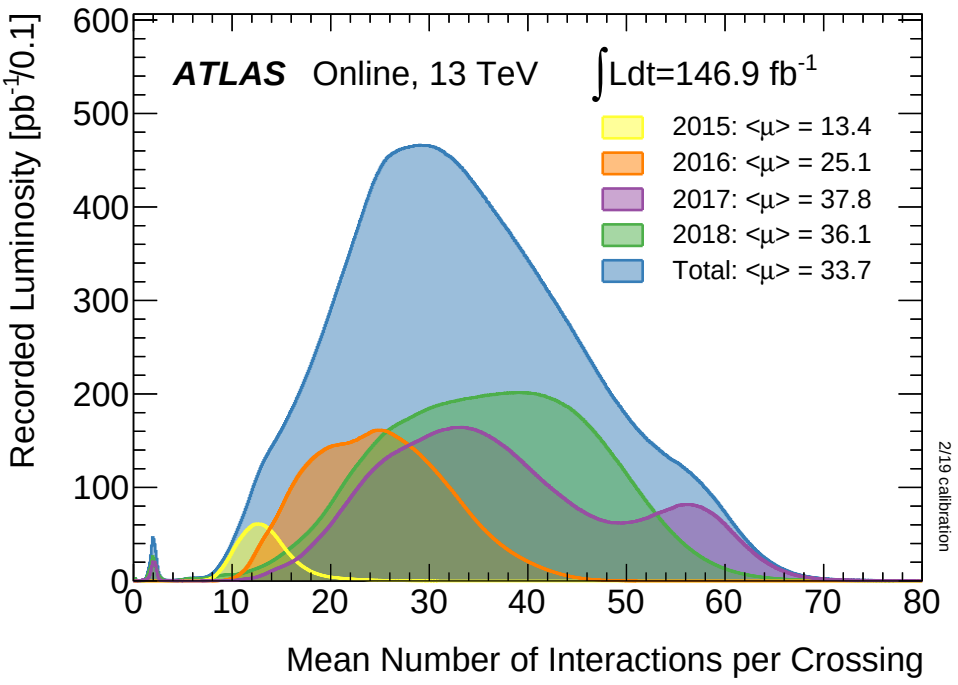

Figure 3.3: Mean p−p interactions per bunch crossing in the ATLAS detector during LHC run-2. 30-40 p−p collisions are expected per event. Source: Ref. [50].

transverse component of momentum, η is the "pseudorapidity", ϕ is the azimuth angle, and E is the energy. The cylindrical ATLAS detector is azimuthally symmetric. Pseudorapidity is defined as

$$\eta = -\ln \tan\left(\frac{\theta}{2}\right), \tag{3.2}$$

where θ is the zenith angle. Pseudorapidity is the massless limit of rapidity,

$$y = \frac{1}{2}\ln\left(\frac{E + p_z}{E - p_z}\right), \tag{3.3}$$

where the z-axis points along the beamline. Pseudorapidity is essentially the rapidity of a particle as if it were massless. Even though particles such as electrons and muons have mass, they are produced by LHC p−p collisions with orders of magnitude more energy than their

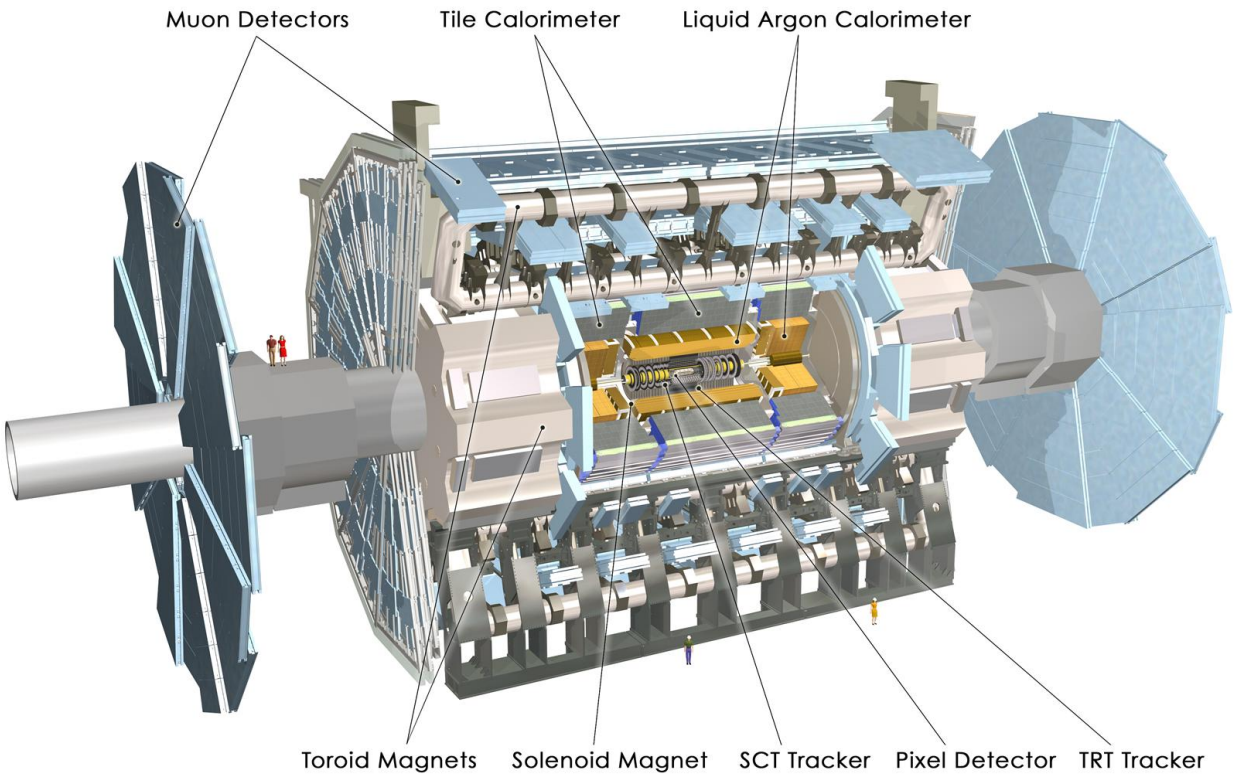

Figure 3.4: The ATLAS detector. Source: Ref. [51].

rest-mass energy and therefore pseudorapidity is approximately the same as rapidity. This approximation breaks down for high-mass jets and other very massive objects, so studies of those objects usually make use of rapidity instead of pseudorapidity. Particles travelling very forward down the beamline with $|\eta| > 2.5$ are typically discarded from analysis, and also particles in the "crack" region $1.37 < |\eta| < 1.52$ where the barrel and endcap regions of the detector meet and there is no sensitive detector material.

Figure 3.5 shows how the different detector subsystems work together to accomplish the task of particle identification. A particle's charge can be determined from the curvature of its track in the inner detector, and its status as hadronic/not-hadronic can be determined based on which calorimeter the particle showered in. Muons do not shower in the calorimeters and instead are tracked on the way out by the muon spectrometer. Ghostly neutrinos pass

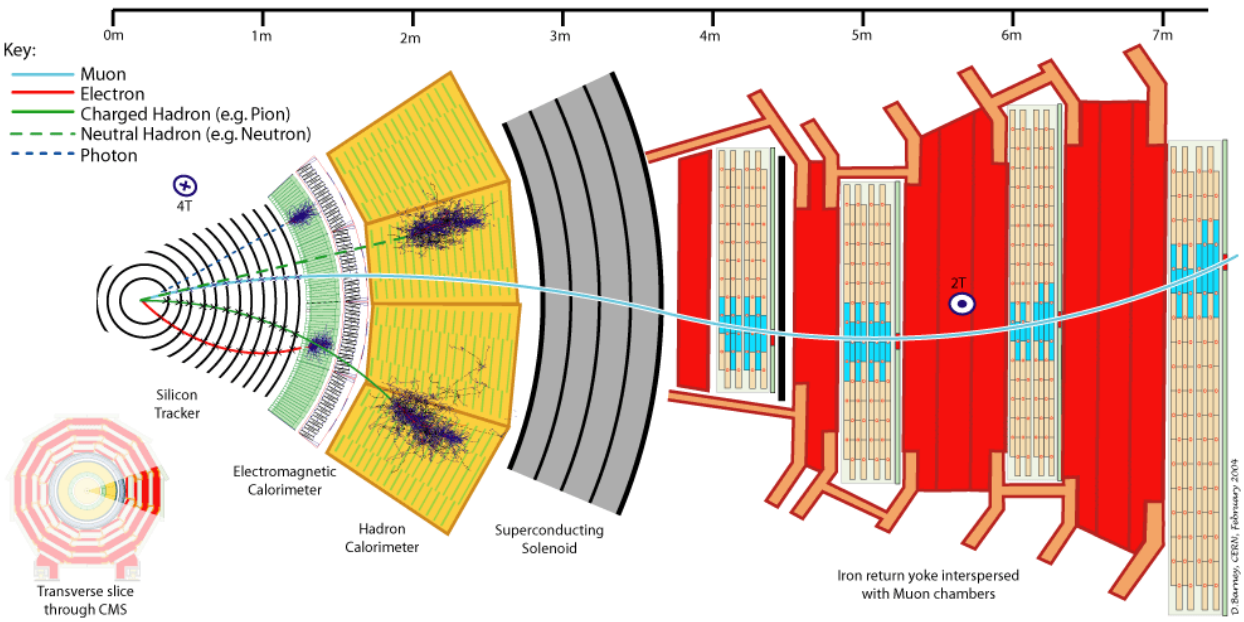

Figure 3.5: Particle ID in the CMS experiment. Particle ID in ATLAS is largely the same. Source: Ref. [53].

through all detector subsystems without interacting, so their presence can only be inferred from apparent violations of conservation of momentum based on measurements of visible particles.

3.2.1 ATLAS trigger system

The ATLAS detector produces about 1.6 Mb of raw data per $p-p$ bunch crossing[54], which totals to tens of Tb per second at a bunch crossing rate of 40 MHz. It is impractical to transfer and store such a large volume of data, but fortunately (or unfortunately?) most $p-p$ collisions are so-called "soft QCD" events which don't need to be recorded in great numbers. To reduce the bandwidth and data storage demand of the ATLAS experiment, the detector implements a trigger system[55] that performs fast online analysis of raw data and decides which events are interesting enough to record to disk for later offline analysis.

The trigger system consists of two stages: the hardware-based L1 trigger and software-based high-level trigger (HLT). The L1 trigger reduces the event rate from 40 MHz to about 100 kHz, and the HLT further reduces it to 1 kHz. With this system, ATLAS records about 1.5 Gb/s to disk or about 3.2 Pb per year. This dataset is further reduced in size by offline data processing; the data used in this thesis was reduced to $\mathcal{O}$(10 Tb) after central data processing and $\mathcal{O}$(100 Gb) after our first processing step.

3.2.2 Inner tracker

The inner tracker or inner detector (ID)[56] comprises the innermost layers of ATLAS and is designed to non-destructively measure particles' momentum as they propagate from the collision point. See Figure 3.6 for a diagram of the sublayers of the ID and their distances from the collision point. The ID consists of three subsystems: the pixel detector, the semiconductor tracker (SCT), and the transition radiation tracker (TRT). A magnetic field of 2 T is provided by a solenoid magnet located between the ID and electromagnetic calorimeter, and the Lorentz force causes charged particles' trajectories to curve as they propagate through the ID with curvature proportional to their momentum. Particles are tracked in space as they propagate through the sublayers, and their trajectories are fit to a helix in order to determine the momentum.

The pixel detectors make up the innermost layers of ATLAS $\mathcal{O}$(1 cm) from the beamline. There were three pixel layers during LHC run-1, and a fourth (the "insertible B-layer" or IBL) was added for run-2. Each layer is a cylindrical stave of 10 cm^2 pixel modules having pixel pitch 50 μm $\times$ 250 μm in the IBL and 50 μm $\times$ 400 μm in the other three layers. There are 1744 modules in total covering 1.7 m^2 with about 80 million readout channels. High-resolution

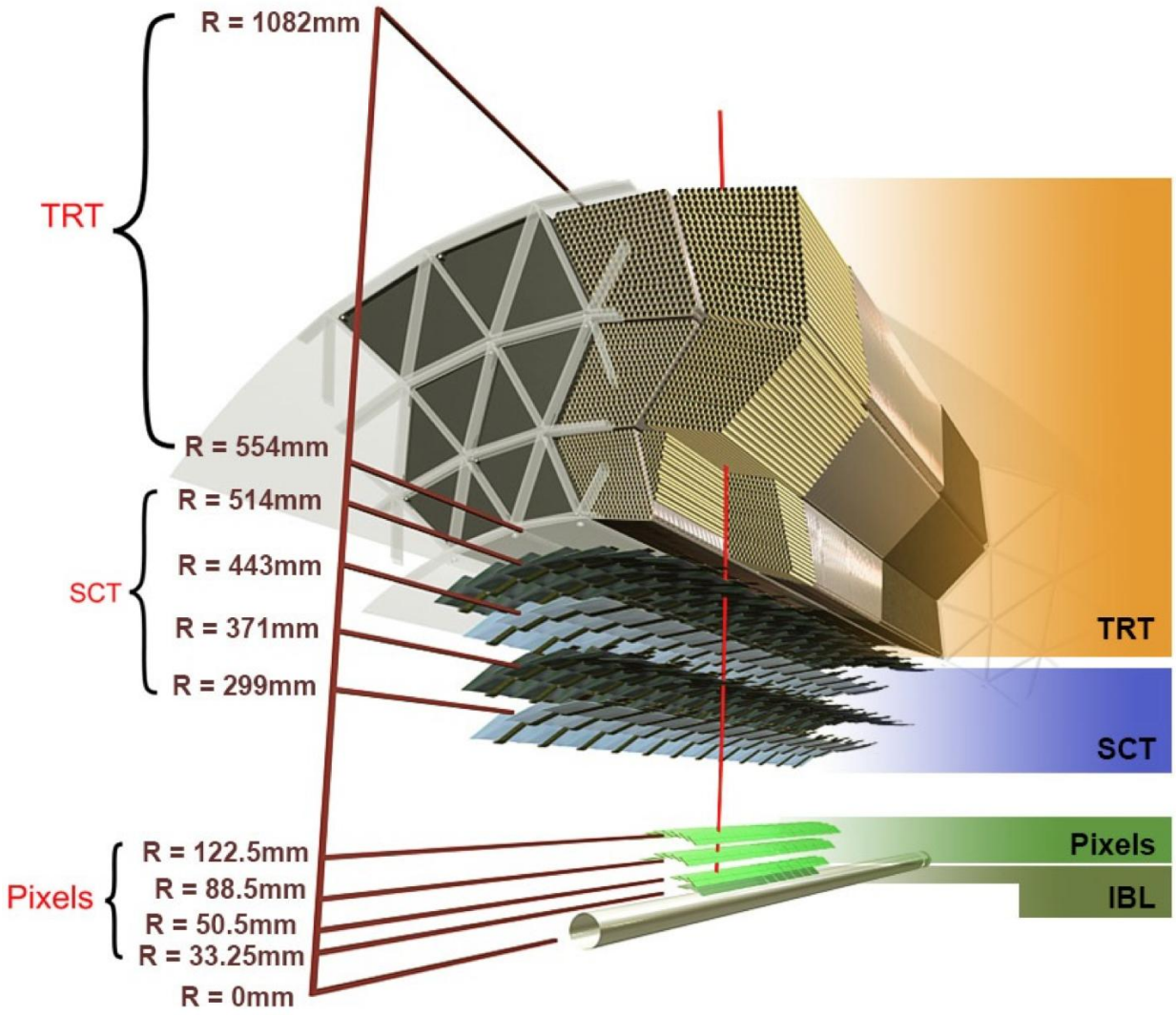

Figure 3.6: Cross section of the ATLAS inner detector. Source: Ref. [51].

data from the pixel detector is essential for reconstructing the primary collision vertex as well as any secondary vertices in $p-p$ collision events.

The SCT[57] is composed of silicon strip detectors with pitch 80 μm in the transverse direction. The strips are tilted somewhat to allow for measurements in the longitudinal direction. The SCT covers 60 m^2 with about 6 million readout channels.

The TRT consists of "straw tube" detectors which are 4 mm-diameter pipes with a 0.03 mm-diameter gold-plated tungsten wire running down the center. The tubes are filled with argon gas and a high voltage is applied between the wire and the tube. Particles passing through the TRT ionize the gas, resulting in measurable signals on the wire from which the particle's position can be deduced based on the timing of the signals. Despite the TRT's resolution being the worst of the inner detector subsystems, it contributes a lot to track fitting due to its longer lever-arm. The spaces between the tubes are filled with a polymer of a certain dielectric constant, causing transition radiation as high energy particles pass through. The transition radiation intensity depends on the Lorentz γ-factor, which in turn depends on the particle's mass. This data helps with the task of particle identification. The TRT comprises 350,000 readout channels.

3.2.3 Calorimeters

The two calorimeter subsystems of ATLAS are designed to destructively measure particles' energy as they are stopped in the detector material. ATLAS's calorimeters are sampling calorimeters composed of alternating layers of sensitive detector material and heavy absorber material. As particles pass through the calorimeter, they ionize the absorber material causing a shower of daughter particles to propagate through the layers. The shower is sampled at

each layer of detector material, and the data is compared with calibrations to determine the energy of the particle. The calorimeters are segmented into "cells" in the η-ϕ plane, allowing for analysis of the shower shape as it proceeds through the layers of the calorimeter.

Electrons and photons shower via a repeated process of bremsstrahlung and pair production. Electrons passing through the absorber material will emit photons as bremsstrahlung radiation and photons passing through the absorber material will pair-produce e^+e^- pairs, which themselves undergo bremsstrahlung and the cycle repeats until the incident particle's energy is depleted. The characteristic length scale for an electromagnetic shower is called the radiation length. Hadronic showers on the other hand proceed by hadronization of quarks and gluons, with a characteristic length scale called the nuclear interaction length. Typically nuclear interaction lengths of materials are much longer than radiation lengths, hence the separate electromagnetic and hadronic calorimeter subsystems. The electromagnetic calorimeter (ECal) uses liquid argon as its detector material and lead as its absorber material. The hadronic calorimeter (HCal) uses plastic scintillator as its detector material and iron as its absorber material. The calorimeters together comprise about 200,000 readout channels.

The energy resolution ΔE of a sampling calorimeter can be decomposed into three components:

$$\frac{\Delta E}{E} = \sqrt{\left(\frac{a}{\sqrt{E}}\right)^2 + b^2 + \left(\frac{c}{E}\right)^2}, \tag{3.4}$$

where the first term, called the stochastic term, arises from statistical fluctuations obeying a Poisson distribution, the constant term arises from instrumental effects, and the third term arises from electronic noise, as well as noise from background radiation present in the ATLAS cavern.

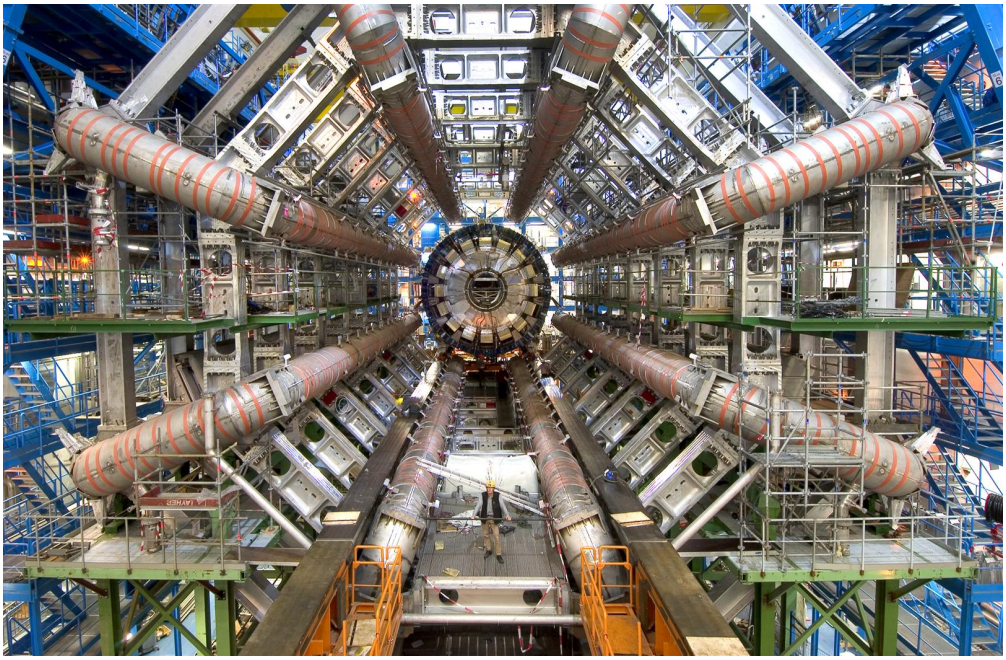

Figure 3.7: Photo of ATLAS's characteristic toroid magnets. Source: Ref. [58].

3.2.4 Muon spectrometer

The muon spectrometer, comprising the outermost layers of the ATLAS detector, is designed to track muons as they exit the detector. The MS, depicted in Figure 3.8, is comprised of gas-filled detectors that detect and localize ionizing particles as they pass through. Muons are much more massive than electrons and as a result tend to lose energy to ionization rather than bremsstrahlung in matter. Muons therefore typically don't create showers in the calorimeter and instead pierce all the way through. Toroid magnets, pictured in Figure 3.7, provide a peak magnetic field of 4 T[59], which curves the charged muons' trajectories enabling measurements of their momenta. Tracking data from the ID and MS are combined to improve the resolution of the measurements.

The MS comprises four subsystems with slightly different functions. Monitored drift tubes (MDTs) cover much of the central region of the detector and consist of 3 cm pipes

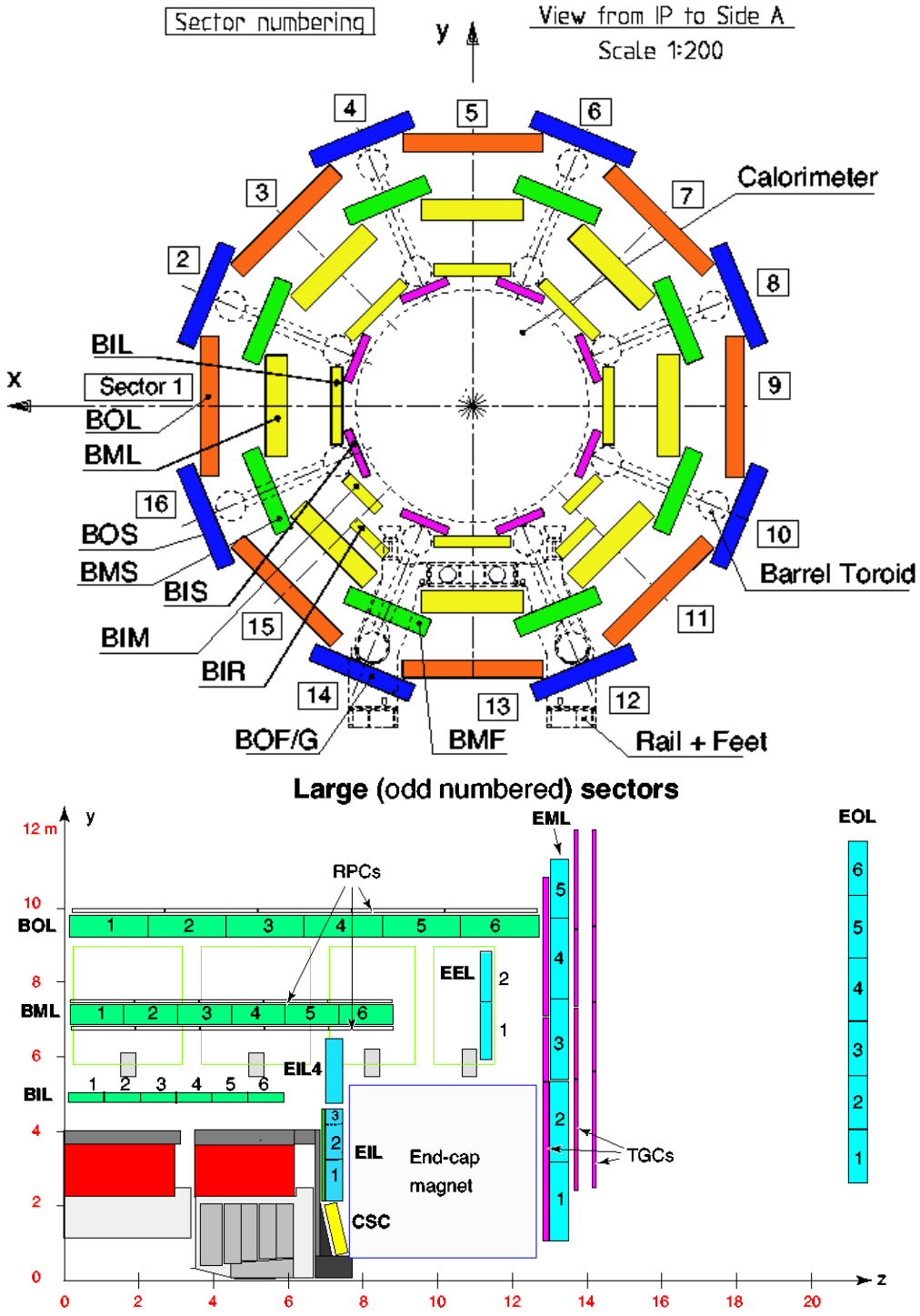

Figure 3.8: The ATLAS muon spectrometer in the (top) x-y plane and (bottom) y-z plane. Source: Ref. [52].

filled with pressurized gas and a central wire with a high potential difference applied. In the forward region ($2.0 < |\eta| < 2.7$) cathode strip chambers (CSCs) are used instead, which are gas-filled chambers containing layers of anode wires and cathode strips. The CSCs have a higher resolution and faster readout rate than the MDTs. Additionally, resistive plate chambers (RPCs) and thin gap chambers (TGCs) are used to help the trigger system identify muons. These subsystems have lower precision but faster readout rate. RPCs are used in the central region while TGCs are used in the forward region. Overall there are about 2 million readout channels associated with the MS.

Chapter 4

Data and Simulations

4.1 Event reconstruction

This section gives an overview of the process of identifying and reconstructing physics objects from raw digitized data aggregated from the ATLAS detector subsystems. The relevant physics objects for the $W^{\pm}W^{\mp}\gamma$ analysis are electrons, photons, muons, jets (specifically b-jets), and missing transverse energy ($E_{\mathrm{T}}^{\mathrm{miss}}$). Each of these objects have their four-momentum ($p_{\mathrm{T}}, \eta, \phi, E$) measured, as well as various other properties such as electric charge and scattering impact parameter.

Many reconstruction algorithms provide their output in the form of a discriminant, which is essentially a confidence score that indicates the reliability of the measurement. There is a trade-off between signal acceptance efficiency and background rejection efficiency; high discriminant values usually result in a more pure dataset but fewer data points while low discriminant values usually result in higher signal acceptance but more background contamination. The terminology of loose, medium, and tight "working points" (WPs) refers to the discriminant threshold used for object/event selection.

4.1.1 Tracks and vertices

Charged particles such as electrons ionize the sensitive detector material of the ID subsystems, and their trajectories ("tracks") can be reconstructed from this data[61]. Raw data from the pixels and SCT strips are processed into 3D space points[62], and sets of three space points are considered track seeds. After track seeds are identified, a combinatorial Kalman filter[63]

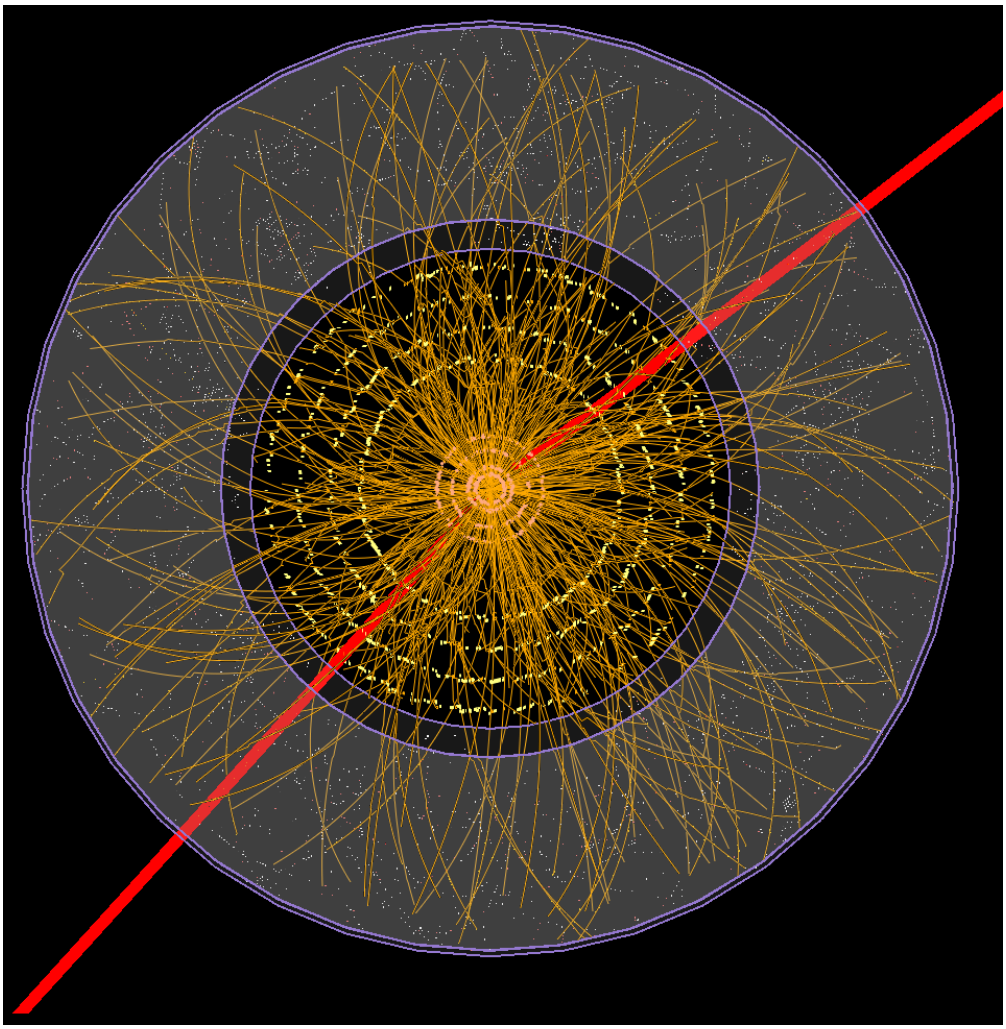

Figure 4.1: Reconstructed tracks of a $Z \to \mu^+\mu^-$ candidate event recorded by ATLAS on June 14, 2015. The red lines represent the reconstructed muons. Source: Ref. [60]

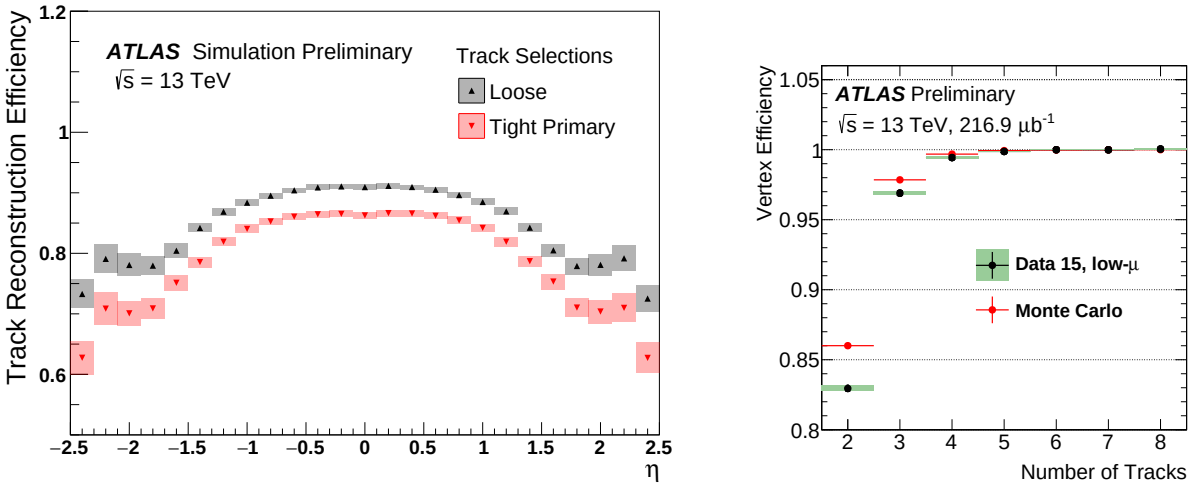

Figure 4.2: (Left) Track reconstruction efficiency vs. η; efficiency is about 85-90% in the central region of the detector. Source: Ref. [64]
(Right) Vertex reconstruction efficiency vs. # of tracks; efficiency exceeds 95% when at least 3 tracks are present. Source: Ref. [65]

is used to generate track candidates by combining them with additional space points from other layers. Since there may be multiple track candidates associated with each seed, an ambiguity solver algorithm based on χ^2 minimization is used to choose the most optimal track candidate. The tracks are then extended with data from the TRT. An event display of the tracks of a typical ATLAS event is shown in Figure 4.1.

Once the tracks are reconstructed and disambiguated, the tracks are extrapolated back to the interaction point in order to reconstruct the primary vertex of the original $p-p$ collision as well as any pileup verticies present in the event[66]. An iterative algorithm is used to reconstruct the primary vertex, seeded from the densest cluster of points where extrapolated tracks approach closest to the beamline. Each track's compatibility with the vertex is computed, and tracks with low compatibility are removed and used to seed a new vertex. This is repeated until all tracks are assigned to a vertex or no new verticies can be formed of the remaining tracks. After this procedure, the vertex with the highest squared

sum of track p_{T} is identified as the primary vertex and the other vertices are identified as pileup vertices. Figure 4.2 shows the performance of the track and vertex reconstruction algorithms. Once the primary vertex has been identified, the transverse and longitudinal components of each track's scattering impact parameter, d_0 and $z_0 \sin\theta$ respectively, can be computed from the point of closest approach to the vertex. High values of impact parameter can indicate particles originating from a secondary vertex in the event, e.g. from the decay of a relatively long-lived B meson.

4.1.2 Calorimeter clusters

The topo-cluster algorithm[67, 68] is used to build 3D energy "clusters" from the signals arising from energy deposition in calorimeter cells. Proto-clusters are seeded by calorimeter cells with high signal-to-noise significance $\zeta = E_{\mathrm{cell}}/\sigma_{\mathrm{noise,cell}}$ where $\sigma_{\mathrm{noise,cell}}$ is the expected noise in the cell as determined by calibrations. Neighboring cells that pass a ζ threshold are then iteratively added to the proto-clusters, and proto-clusters that share cells are merged. After this iterative process, clusters with multiple local maxima are split by another iterative algorithm. The algorithm is seeded by the local maxima, and neighboring cells are iteratively added to the freshly split clusters until they have all been assigned. Some cells can be assigned to two clusters; in which case the shared cell's contributions to the two proto-clusters is weighted by

$$w_1 = \frac{E_1}{E_1 + rE_2},\ w_2 = 1 - w_1,\ r = e^{d_1 - d_2}, \tag{4.1}$$

where E_1 and E_2 are the energies of the proto-clusters and d_1, d_2 are the distances from the cell to the centroids of the proto-clusters. Proto-clusters that pass a minimum energy

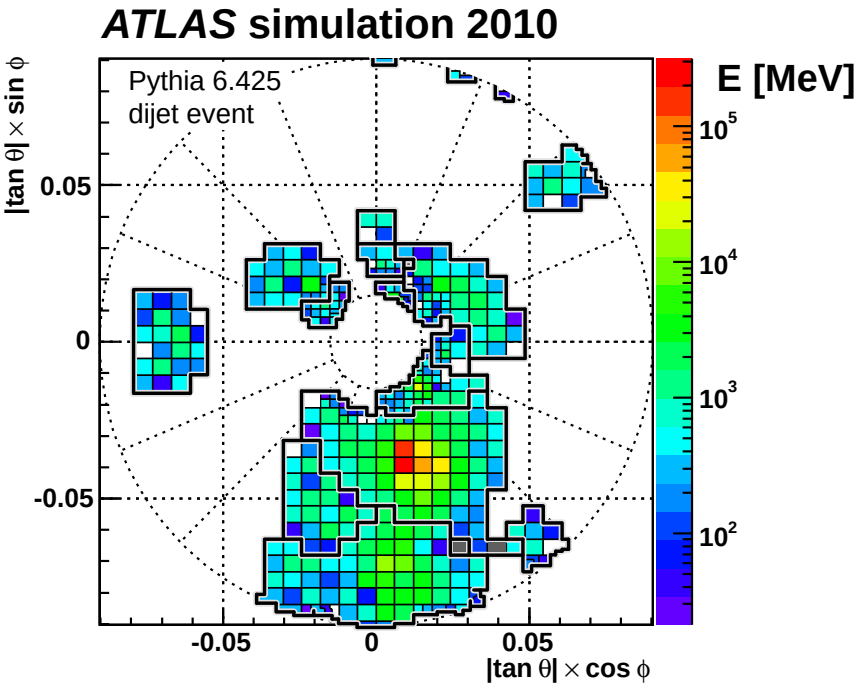

Figure 4.3: Reconstructed topo-clusters in the $\theta - \phi$ "plane" from a simulated dijet event. Source: Ref. [68]

threshold are selected as the final clusters. Figure 4.3 shows an example of the output of the topo-clustering algorithm in the θ-ϕ plane.

4.1.3 Electrons and photons

Due to the nature of electromagnetic interactions with detector material, the reconstruction processes for electrons and photons are intimately linked[69, 70]. Electrons can undergo bremsstrahlung radiation while traversing ID material and emit photons, and photons can undergo pair-production into a e^+e^- pair in the ID ("photon conversion"). These secondary particles are usually reconstructed as the same ECal cluster as the primary, so a Gaussian sum filter based[71] track refitting is performed taking ECal information into account.

After the track refitting, the ECal topo-clusters are reprocessed to build "superclusters" designed to encompass the energy cluster of primary electrons/photons along with their

associated secondaries. The supercluster algorithm is seeded by the highest-E_{T} ECal topo-clusters. Neighboring topo-clusters ("satellite clusters") are iteratively added to supercluster candidates if they pass energy threshold and track-matching requirements. Electron-based and photon-based superclusters are built separately from the same topo-cluster seeds using track-matching criteria described in Figure 4.4. Electron and photon superclusters that share the same seed topo-cluster are disambiguated based on further track quality criteria. Some superclusters can not be disambiguated and the final classification decision is done on a per-analysis basis. Figure 4.6 shows the reconstruction efficiency for electrons and photons vs. transverse energy E_{T}.

The electron/photon energy scales are calibrated[72] with data from $Z \to e^+e^-$ decays and the energy resolution is corrected to match Monte Carlo simulations. The η-dependent energy scale corrections,

$$E^{\mathrm{data,corr}} = E^{data}/(1+\alpha_1), \text{ and } \left(\frac{\sigma_E}{E}\right)^{\mathrm{MC,corr}} = \left(\frac{\sigma_E^{MC}}{E}\right)^{\mathrm{MC}} \oplus c_i, \tag{4.2}$$

where $\oplus$ denotes a sum in quadrature, are plotted in Figure 4.5 with associated uncertainties.

The $W^{\pm}W^{\mp}\gamma$ analysis requires "prompt" (i.e., originating promptly from $W^{\pm}W^{\mp}\gamma$ and not later from some secondary process) electrons and photons originating from hard-scatter vertices. To reject electrons from pileup, a likelihood-based discriminant is used. The disciminant is computed from various parameters comprising information about supercluster-track matching as well as energy deposition in the ECal and HCal layers. Figure 4.6 (left) shows the electron reconstruction efficiency for three working points associated with the discriminant. Photons from pileup are identified and rejected by cuts on shower shape

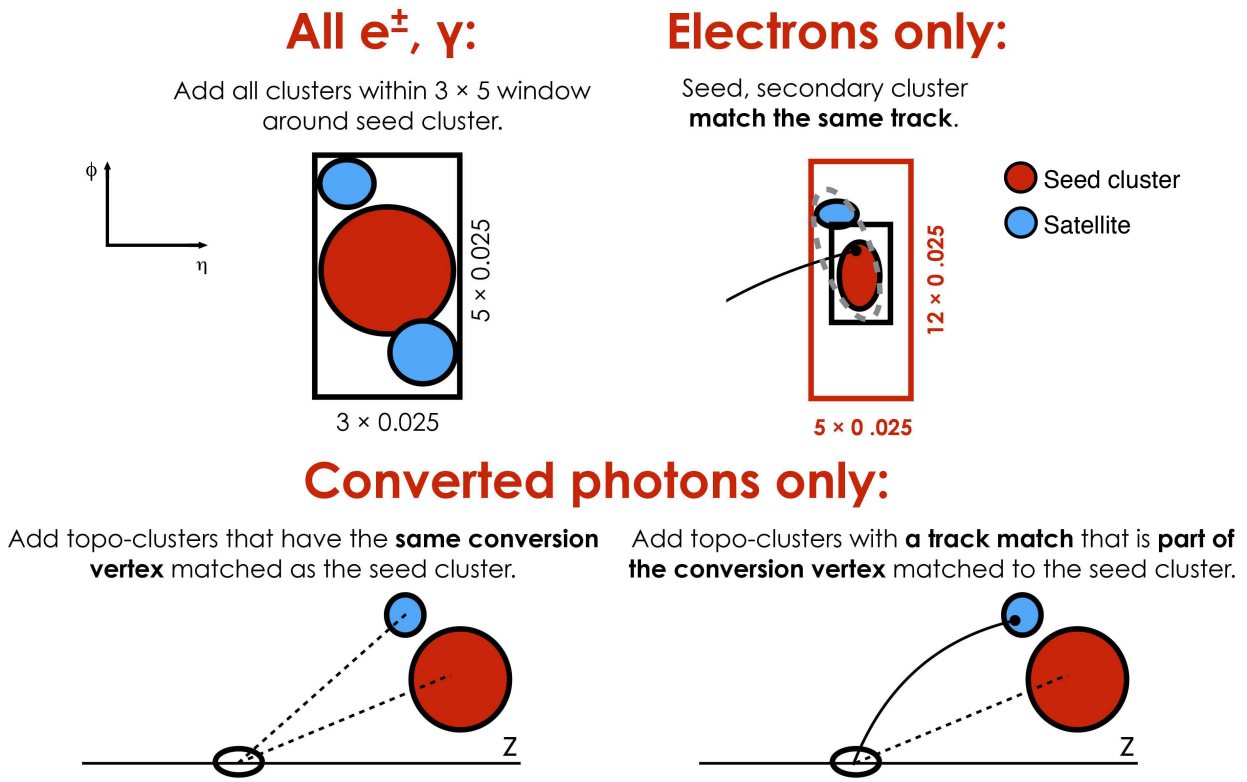

Figure 4.4: Track-matching criteria used for EM supercluster-building. Source: Ref. [70]

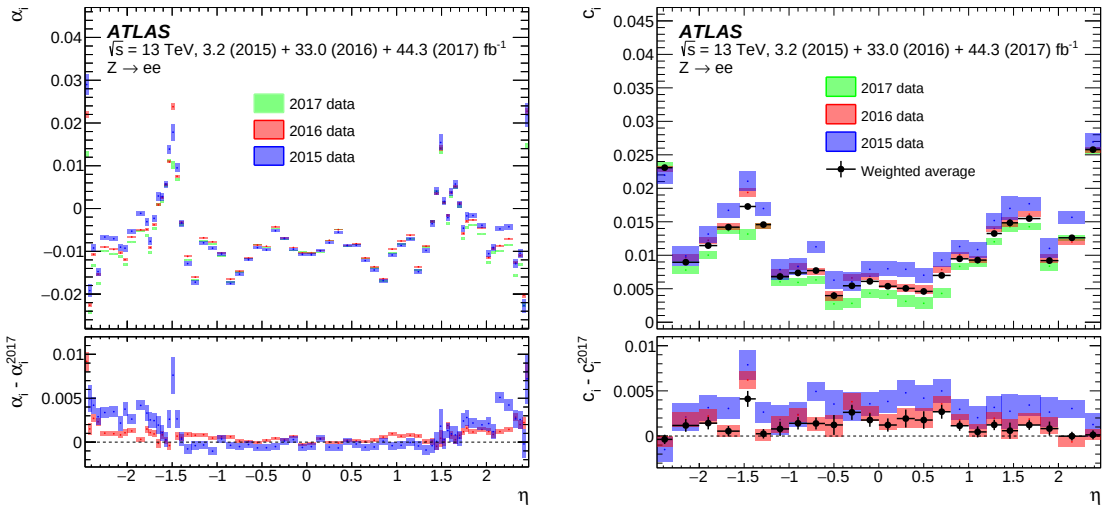

Figure 4.5: Electron energy scale corrections as defined in Equation (4.2), these corrections are of $\mathcal{O}(1\%)$. Source: Ref. [70]

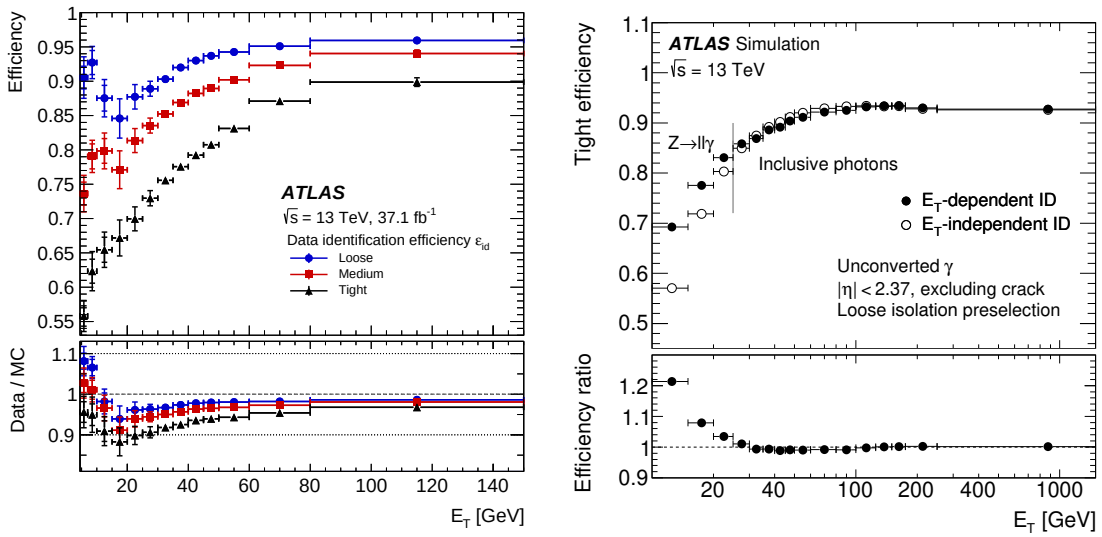

Figure 4.6: (Left) Electron reconstruction efficiency in e^+e^- events for three working points; at high E_{T} the efficiency approaches 90-95%.
(Right) Unconverted photon reconstruction efficiency in $\ell^+\ell^-\gamma$ events; at high E_{T} efficiency approaches 90%. Source: Ref. [70]

	Electrons	Photons
p_{T}	> 20 GeV	> 20 GeV
$\lvert\eta\rvert$	< 2.47, veto crack region	< 2.37, veto crack region
ID WP	`TightLH`	`Tight`
Isolation WP	`PLVTight`	`FixedCutTight`
$\lvert d_0/\sigma_{d_0}\rvert$	< 5.0	–
$\lvert z_0 \sin\theta\rvert$	< 0.5 mm	–

Table 4.1: Electron and photon selection criteria for the $W^{\pm}W^{\mp}\gamma$ analysis.

variables. To further suppress contributions from pileup, isolation requirements based on information about tracks and clusters in a cone around candidate electrons and photons are imposed. For photons, cuts on the sums of p_{T} and E_{T} of tracks in a cone around the photon candidates are used, while for electrons a multivariate discriminant called prompt lepton veto (PLV) based on these cone variables is used. In the $W^{\pm}W^{\mp}\gamma$ analysis we chose tight working points for these selections. The selection criteria for electrons and photons in the $W^{\pm}W^{\mp}\gamma$ analysis is summarized in Table 4.1.

4.1.4 Muons

The reconstruction and identification of muons is based on data from all subsystems of the ATLAS detector[73]. Muon track candidates are reconstructed separately in the ID and MS subsystems and are combined with a global fit, including information from the calorimeters. The ID tracks are built like for any other particle (see Section 4.1.1) and tracks from the MS are built from combinations of track segments in each of the MS subsystems. Reconstructed muon candidates are classified according to four categories:

- Combined muons (CB): CB muons are reconstructed with a combined fit to hits in both the ID and MS. The combined tracks are formed either by extrapolating tracks from the MS to the ID or vice versa. These are considered the highest quality muons.

- Segment-tagged muons (ST): ID tracks are classified as ST muons if they match to at least one track segment in the MDT or CSC subsystems of the MS. These muons typically have low p_{T} or are outside the nominal acceptance region of the MS.

- Calorimeter-tagged muons (CT): ID tracks are classified as CT muons if they are associated with an energy deposit in the calorimeter consistent with a muon. These are considered the lowest quality muons.

- Extrapolated muons (ME): MS tracks are classified as ME muons if they don't match to an ID track, useful for muon reconstruction in space not covered by the ID especially at high $|\eta|$.

Final muons are selected from muon candidates based on the χ^2 of the combined track fit, as well as the differences in charge and p_{T} between the ID and MS tracks. These

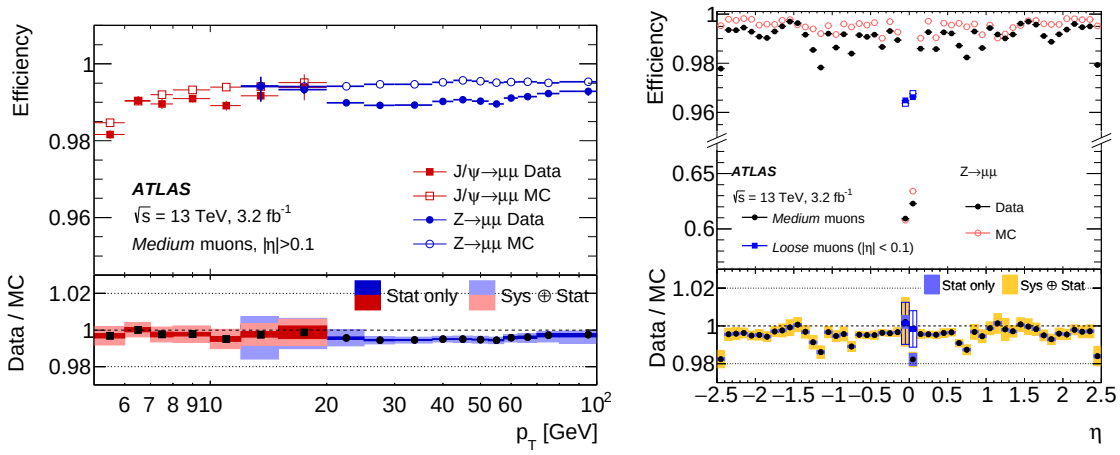

Figure 4.7: Muon reconstruction efficiency in data and MC simulations is about 99%. Source: Ref. [74]

criteria are designed to discriminate prompt signal muons from background mainly due to charged hadrons decaying to muons in-flight. Additionally, isolation requirements based on the sum of ID track p_{T} in a cone around muon candidates is imposed to further select for prompt muons. For the $W^{\pm}W^{\mp}\gamma$ analysis the `Medium` working point for identification and `PflowTight_FixedRad` isolation working point are used. The `Medium` WP selects CB and ME muon candidates with some additional quality requirements. Muon momentum in Monte Carlo simulations is corrected to match the distribution in data using $Z \to \mu^{+}\mu^{-}$ and $J/\Psi \to \mu^{+}\mu^{-}$ events. Muon reconstruction efficiency for the medium working point is shown in Figure 4.7; muon p_{T} resolution is about 2% for central muons and about 3% for forward muons.

4.1.5 Jets and b-tagging

Quarks and gluons produced in $p-p$ collisions quickly hadronize to form color-neutral combinations, namely baryons and mesons. This process results in a cone-shaped spray of particles that leave tracks and energy clusters in the ATLAS detector subsystems. The

	Muons
p_{T}	> 20 GeV
$\lvert\eta\rvert$	< 2.5
Quality WP	`Medium`
Isolation WP	`PflowTight_FixedRad`
$\lvert d_0/\sigma_{d_0}\rvert$	< 3.0
$\lvert z_0 \sin\theta\rvert$	< 0.5 mm

Table 4.2: Muon selection criteria for the $W^{\pm}W^{\mp}\gamma$ analysis.

particle flow algorithm[75] is used to reconstruct jets using data from the ID and calorimeters. Charged tracks from the ID (excluding those already matched to electrons and muons) are matched to topo-clusters in the calorimeters, and any unmatched clusters are assumed to be due to neutral particles. The anti-k_t algorithm[76] is then used to combine the tracks and unmatched clusters into a single jet. The algorithm is based on the distance measures

$$d_{ij} = \min(k_{t,i}^{-2}, k_{t,j}^{-2})\frac{\Delta_{ij}^2}{R^2};\ d_{iB} = k_{t,i}^{-2}, \tag{4.3}$$

where k_t is the transverse momentum, $\Delta_{ij} = \sqrt{(\eta_i - \eta_j)^2 + (\phi_i - \phi_j)^2}$ is a distance measure between two objects in the η-ϕ plane, and R is a fixed jet radius parameter equal to 0.4 in the $W^{\pm}W^{\mp}\gamma$ analysis. d_{ij} represents the minimum-inverse-momentum weighted distance between objects and d_{iB} represents the distance of an object to the beamline. The anti-k_t algorithm iteratively merges the pairs of objects that minimize d_{ij} until an object has $d_{iB} < d_{ij} \forall j$, in which case the object i is removed from the iterations and is considered a jet candidate.

Jet candidates are calibrated[77] in order to correct for inaccuracy in the jet reconstruction algorithm, noise, losses in inactive detector material, and the possibility of high energy jets piercing all the way through HCal. These calibrations are based on Monte Carlo simulations

	Jets
p_{T}	> 20 GeV
$\lvert\eta\rvert$	< 2.5
JVT	< 0.59
ID	`PFlow`
b-tagging WP	`DL1r` 85%

Table 4.3: Jet selection criteria for the $W^{\pm}W^{\mp}\gamma$ analysis.

as well as data from dijet events. A cut on the jet vertex tagger (JVT)[78] discriminant is also imposed, which scores how likely the jet was to have originated from the primary vertex as opposed to pileup. JVT is based on the fraction of total p_{T} from jet-associated tracks originating from the primary vertex. The fraction of reconstructed jet energy to energy of corresponding MC truth jets is plotted in Figure 4.8 (left). Jet selection criteria for the $W^{\pm}W^{\mp}\gamma$ analysis are summarized in Table 4.3.

The main background physics process in the $W^{\pm}W^{\mp}\gamma$ analysis is $t\bar{t}\gamma$ production, largely due to the $\sim$20% branching fraction of $t \to \ell^{\pm}b$[13]. Therefore to suppress $t\bar{t}\gamma$ events containing a b-quark are vetoed. The `DL1r` discriminant[79] is used to tag jets originating from b-quarks. B mesons have a relatively long lifetime and can travel several millimeters from the primary vertex before decaying, so a key signature of a b-jet is a vertex displaced in space from the primary vertex. The `DL1r` discriminant is the output of a deep neural network trained on $t\bar{t}$ and $Z \to q\bar{q}$ events. The parameters to the neural network include jet p_{T} and $|\eta|$ along with the output of several more primitive b-tagging routines based on impact parameters and identification of displaced vertices. The `DL1r` disciminant is plotted in Figure 4.8 (right) for light jets, charm jets, and b-jets. For the $W^{\pm}W^{\mp}\gamma$ analysis a tight `DL1r` WP with 85% b-jet efficiency is used.

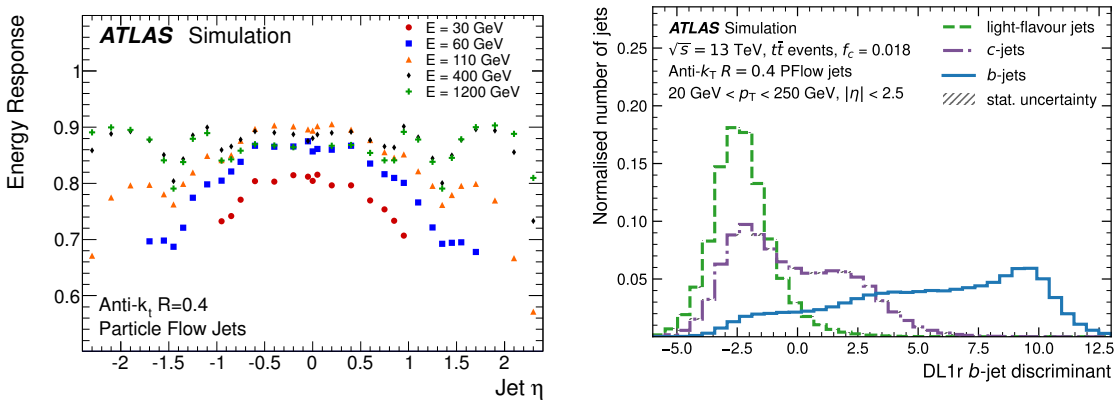

Figure 4.8: (Left) $E_{\text{reco}}/E_{\text{truth}}$ for anti-k_t particle flow jets; for jets with $E \geq 60$ GeV energy response is about 85-90% in the central region of the detector. Source: Ref. [75]
(Right) `DL1r` b-tagging discriminant for different species of jet. Source: Ref. [79]

4.1.6 Missing transverse energy

Leptonic decays of $W^{\pm}$ bosons emit neutrinos that usually pass straight through the whole ATLAS detector without interacting. The energy carried away from these neutrinos is called "missing energy" and can be inferred from apparent violations of conservation of momentum based on asymmetry of tracks and energy clusters in the event. The missing transverse energy[80] is defined as $E_{\text{T}}^{\text{miss}} = \sqrt{(E_x^{\text{miss}})^2 + (E_y^{\text{miss}})^2}$ where

$$E_{x(y)}^{\text{miss}} = \sum p_{x(y)}(e) + \sum p_{x(y)}(\mu) + \sum p_{x(y)}(\text{jet}) + \sum p_{x(y)}(\text{track}), \tag{4.4}$$

where the first three terms ("hard terms") are based on the reconstructed and calibrated electrons, muons, and jets selected for analysis and the last term ("soft term") is based on all other tracks unassociated to these objects. Jets only contribute if they do not overlap with an electron or muon, and if they pass certain quality criteria. The resolution of $E_{\text{T}}^{\text{miss}}$ is plotted in Figure 4.9.

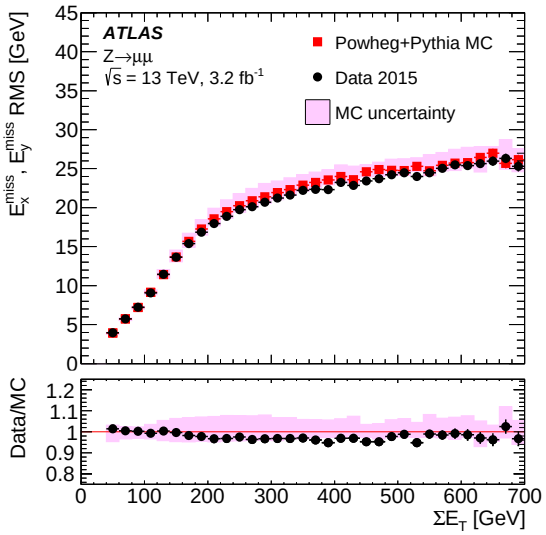

Figure 4.9: $E_{\mathrm{T}}^{\mathrm{miss}}$ resolution vs. $E_{\mathrm{T}}^{\mathrm{miss}}$; resolution is about 5-7%. Source: Ref. [81]

4.2 Phase space region definitions

Events are assigned to phase space regions based on criteria discussed in this section. The main regions for the $W^{\pm}W^{\mp}\gamma$ cross section measurement are summarized in Table 4.4. Event yields attributed to the $W^{\pm}W^{\mp}\gamma$ signal and background processes are listed in Table 4.5.

Common cuts				
Exactly 1 photon Leading lepton $p_{\mathrm{T}} > 27$ GeV $E_{\mathrm{T}}^{\mathrm{miss}} > 20$ GeV				
Cut	$e^{\pm}\mu^{\mp}\gamma$ SR	$t\bar{t}\gamma$ CR	$Z\gamma$ CR	VV CR
Lepton pair	$e^{\pm}\mu^{\mp}$	$e^{\pm}\mu^{\mp}$	$\boldsymbol{e^{\pm}e^{\mp}}$ **or** $\boldsymbol{\mu^{\pm}\mu^{\mp}}$	$e^{\pm}\mu^{\mp}$
$\lvert m(e,\gamma) - 90\ \mathrm{GeV}\rvert$	> 5 GeV	> 5 GeV	–	$<$ **5 GeV**
$m(\ell\ell\gamma)$	–	–	$<$ **100 GeV**	–
Number of b-jets	0	**1**	0	0

Table 4.4: The main phase space regions used to determine the $W^{\pm}W^{\mp}\gamma$ cross section.

$\boldsymbol{e^{\pm}\mu^{\mp}\gamma}$ **SR** The $e^{\pm}\mu^{\mp}\gamma$ signal region (SR) is designed to maximize acceptance of $W^{\pm}W^{\mp}\gamma$ events and minimize acceptance of background processes. In this analysis we are concerned

Process	$e^{\pm}\mu^{\mp}\gamma$ SR	$t\bar{t}\gamma$ CR	$Z\gamma$ CR	VV CR
$W^{\pm}W^{\mp}\gamma$	240 ± 11	18 ± 2.2	42 ± 1.9	15 ± 0.7
$t\bar{t}\gamma$	400 ± 40	1550 ± 60	40 ± 5	31 ± 3.4
$Z\gamma$	150 ± 26	21 ± 11	25000 ± 2800	3.6 ± 2.5
$VZ\gamma$	30 ± 6	4 ± 0.8	30 ± 7	2 ± 0.5
$j \to \gamma$ fakes	70 ± 50	100 ± 60	200 ± 90	3.9 ± 2.1
$e \to \gamma$ fakes	42 ± 3.1	9.5 ± 1.2	20 ± 7	90 ± 6
Total	900 ± 60	1700 ± 90	25000 ± 2900	150 ± 8

Table 4.5: Signal and background processes' contributions to the signal and main control regions.

with leptonic decays of the $W^{\pm}$ boson, i.e. $W^{\pm} \to \ell^{\pm}\nu$, due to large backgrounds in hadronic channels with $W^{\pm} \to jj$. Furthermore, opposite-flavor leptons are required due to the large $Z\gamma$ background in the same-flavor channels (see the $Z\gamma$ CR). Hence, the final state studied in this thesis is $pp \to W^{\pm}W^{\mp}\gamma \to e^{\pm}\mu^{\mp}\gamma\nu\bar{\nu}$.

The $e^{\pm}\mu^{\mp}\gamma$ SR therefore contains exactly one electron, one muon, and one photon, with the electron and muon required to have opposite charge. Due to the neutrinos in the final state, $E_{\mathrm{T}}^{\mathrm{miss}} > 20$ GeV is required. Additionally, events with at least one b-jet are vetoed to reject background from $t\bar{t}\gamma$. Events having $m(e,\gamma)$ within 5 GeV of the Z boson mass (∼90 GeV) are vetoed to reject background from diboson events in which an electron was misidentified as a photon (see the VV CR). Leading lepton p_{T} is required to exceed 27 GeV in all phase space regions in order to ensure all events cleanly passed trigger requirements (see Section 4.3). Distributions of kinematic variables relevant to the analysis in the $e^{\pm}\mu^{\mp}\gamma$ SR are plotted in Figure 4.10.

***$t\bar{t}\gamma$* CR** The $t\bar{t}\gamma$ control region (CR) is designed to be a pure sample of $t\bar{t}\gamma$ events in similar phase space to the $e^{\pm}\mu^{\mp}\gamma$ SR. $t\bar{t}\gamma$ represents the dominant background in the $e^{\pm}\mu^{\mp}\gamma$ SR so

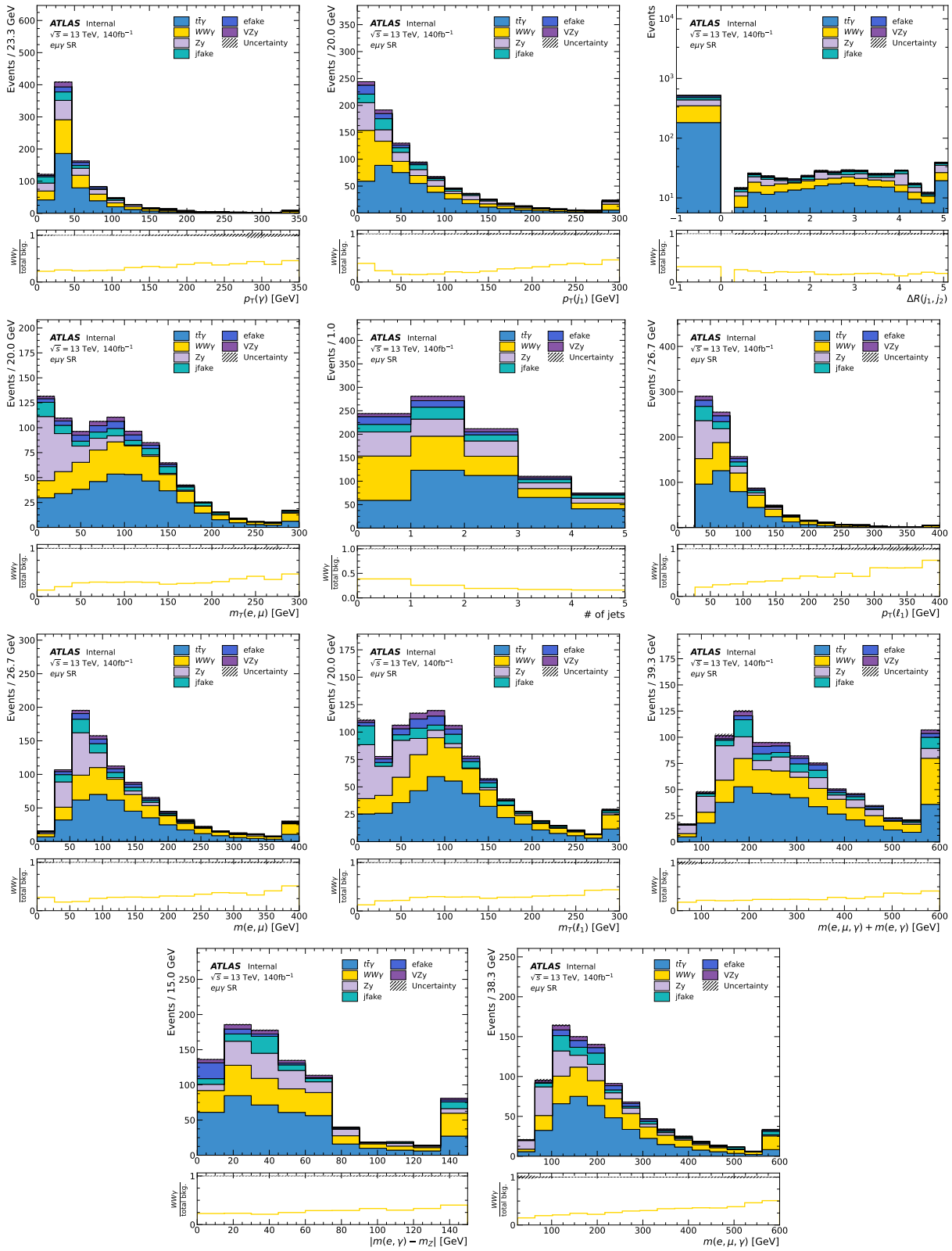

Figure 4.10: Various kinematic distributions in the $e^{\pm}\mu^{\mp}\gamma$ SR. Uncertainty is statistical only. Last bin includes overflow. $\Delta R(j_1, j_2) < 0$ indicates < 2 jets in the event.

an accurate estimation of its contribution in an independent sample is essential. Top quarks almost always undergo $t \to Wb$ decay. As such, this region is defined with the same criteria as the $e^{\pm}\mu^{\mp}\gamma$ SR except instead of a b-jet veto, exactly one b-jet is required. Distributions of kinematic variables relevant to the analysis in the $t\bar{t}\gamma$ CR are plotted in Figure 4.11.

***Zγ* CR** The $Z\gamma$ CR is designed to be a pure sample of $Z\gamma$ events in similar phase space to the $e^{\pm}\mu^{\mp}\gamma$ SR. Z bosons decay to opposite-charge same-flavor lepton pairs (including τ leptons) about 84% of the time [13], so the $Z\gamma$ control region is defined to be almost identical to the $e^{\pm}\mu^{\mp}\gamma$ SR but requiring same-flavor lepton pairs instead of opposite-flavor (i.e., $e^{+}e^{-}$ or $\mu^{+}\mu^{-}$ instead of $e^{\pm}\mu^{\mp}$). Furthermore, the cut on $m(e,\gamma)$ is dropped because of the negligible contribution from $e \to \gamma$ fakes in this region. Additionally, a cut requiring $m(\ell\ell\gamma) > 100$ GeV is imposed because $Z\gamma$ events with non-prompt photons tend to have high $m(\ell\ell\gamma)$. The photons of $Z\gamma$ events in the $e^{\pm}\mu^{\mp}\gamma$ SR are mostly prompt photons. The vetoed events are repurposed to estimate the contribution of photons from misidentified jets. Distributions of kinematic variables relevant to the analysis in the $Z\gamma$ CR are plotted in Figure 4.12.

***VV* CR** Diboson events, particularly $pp \to WZ \to \mu^{\pm}\nu e^{\pm}e^{\mp}$, can enter the $e^{\pm}\mu^{\mp}\gamma$ SR when an electron is misidentified as a photon ("fake photon") or an electron radiates a photon (non-prompt photon). Most of these events are vetoed by requiring $m(e,\gamma)$ at least 5 GeV away from the Z mass. The remaining contribution of this process is estimated with a data-driven method (Section 5.1.2). Additionally, the VV CR is defined with the $m(e,\gamma)$ cut inverted in order to normalize the estimate to data. Distributions of kinematic variables relevant to the analysis in the VV CR are plotted in Figure 4.13.

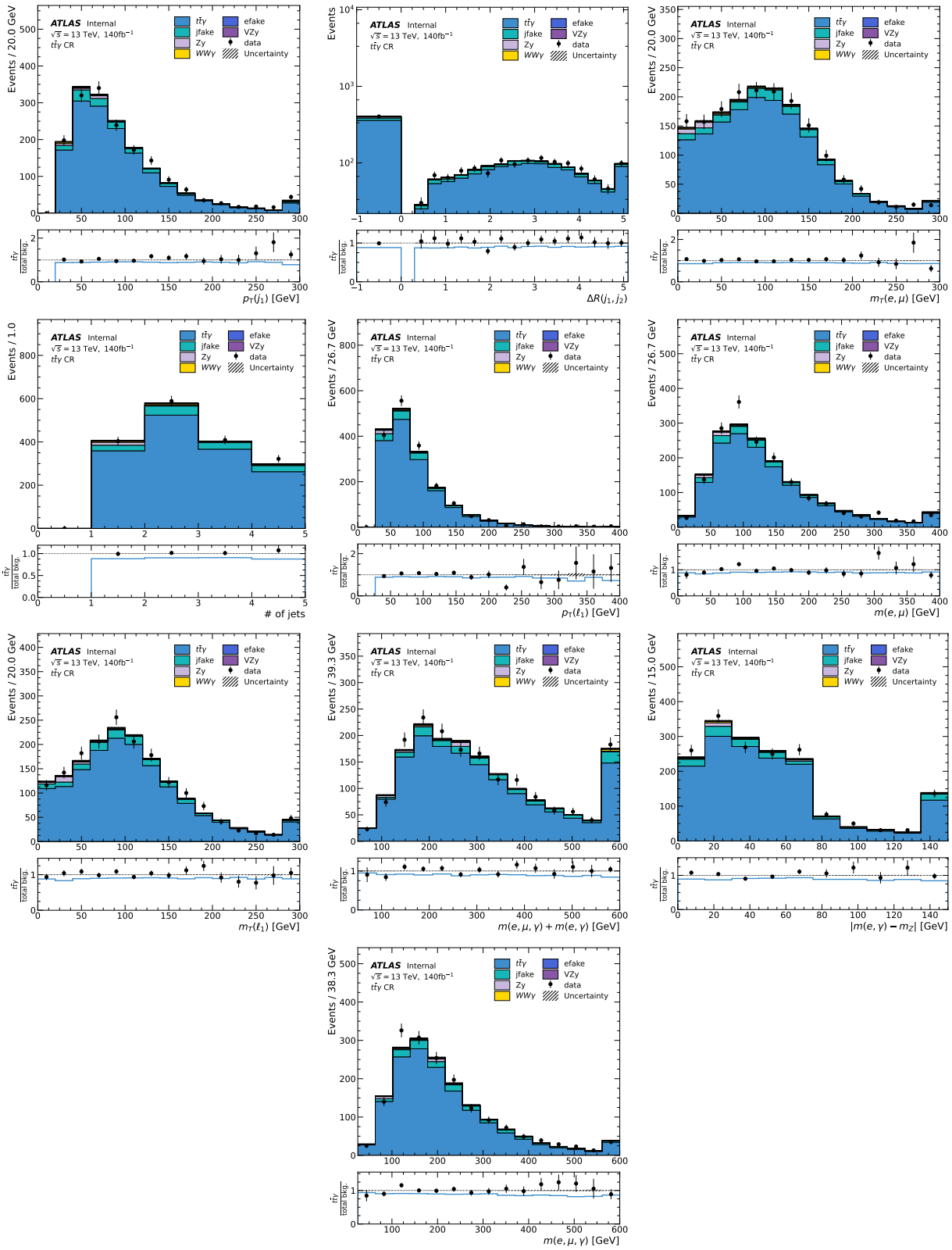

Figure 4.11: Various kinematic distributions in the $t\bar{t}\gamma$ CR. Uncertainty is statistical only. Last bin includes overflow. $\Delta R(j_1, j_2) < 0$ indicates < 2 jets in the event.

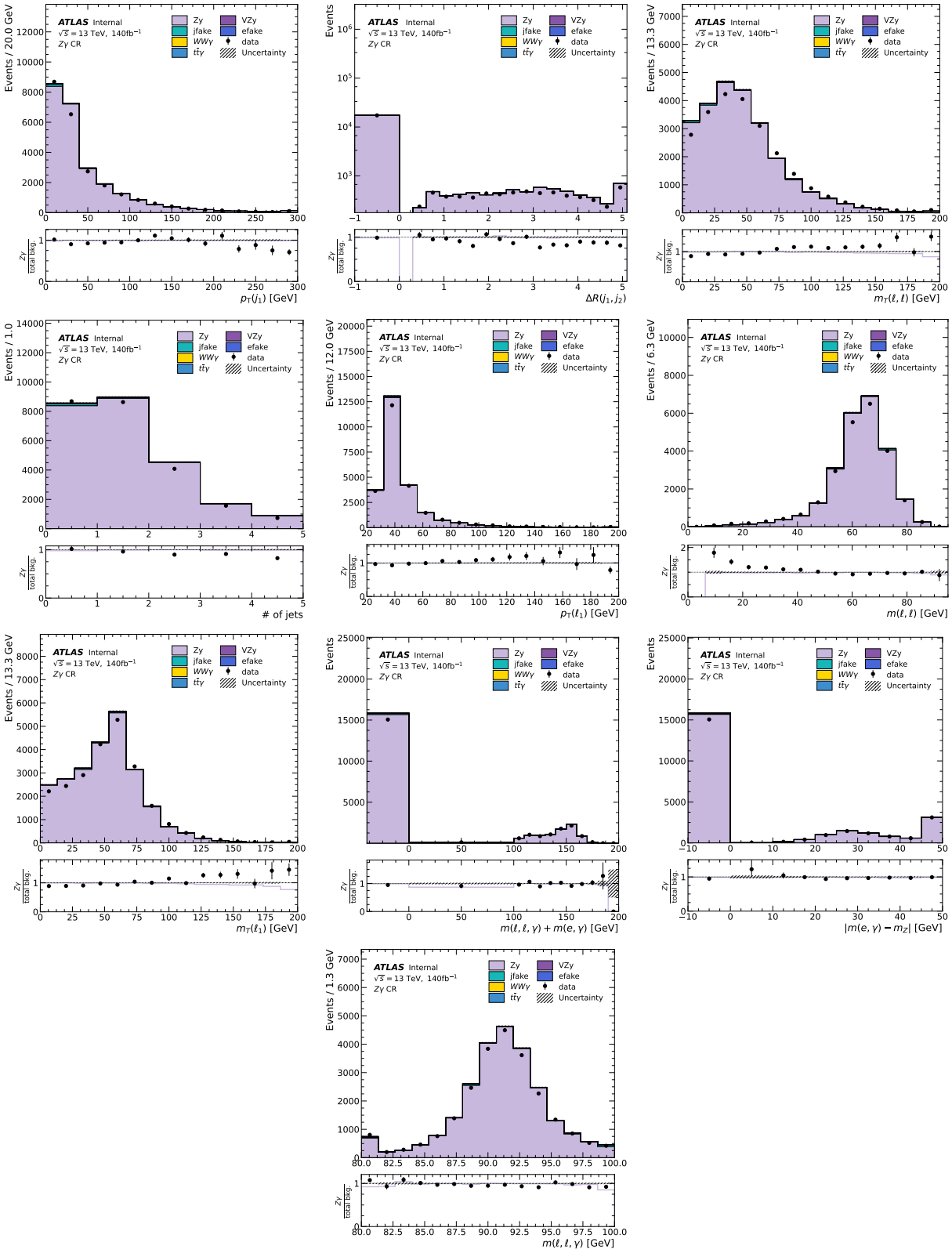

Figure 4.12: Various kinematic distributions in the $Z\gamma$ CR. Uncertainty is statistical only. Last bin includes overflow. $\Delta R(j_1, j_2) < 0$ indicates < 2 jets in the event. $m(e, \mu, \gamma) + m(e, \gamma) < 0$ and $|m(e, \gamma) - m_Z| < 0$ indicate $\mu^{\pm}\mu^{\mp}$ events.

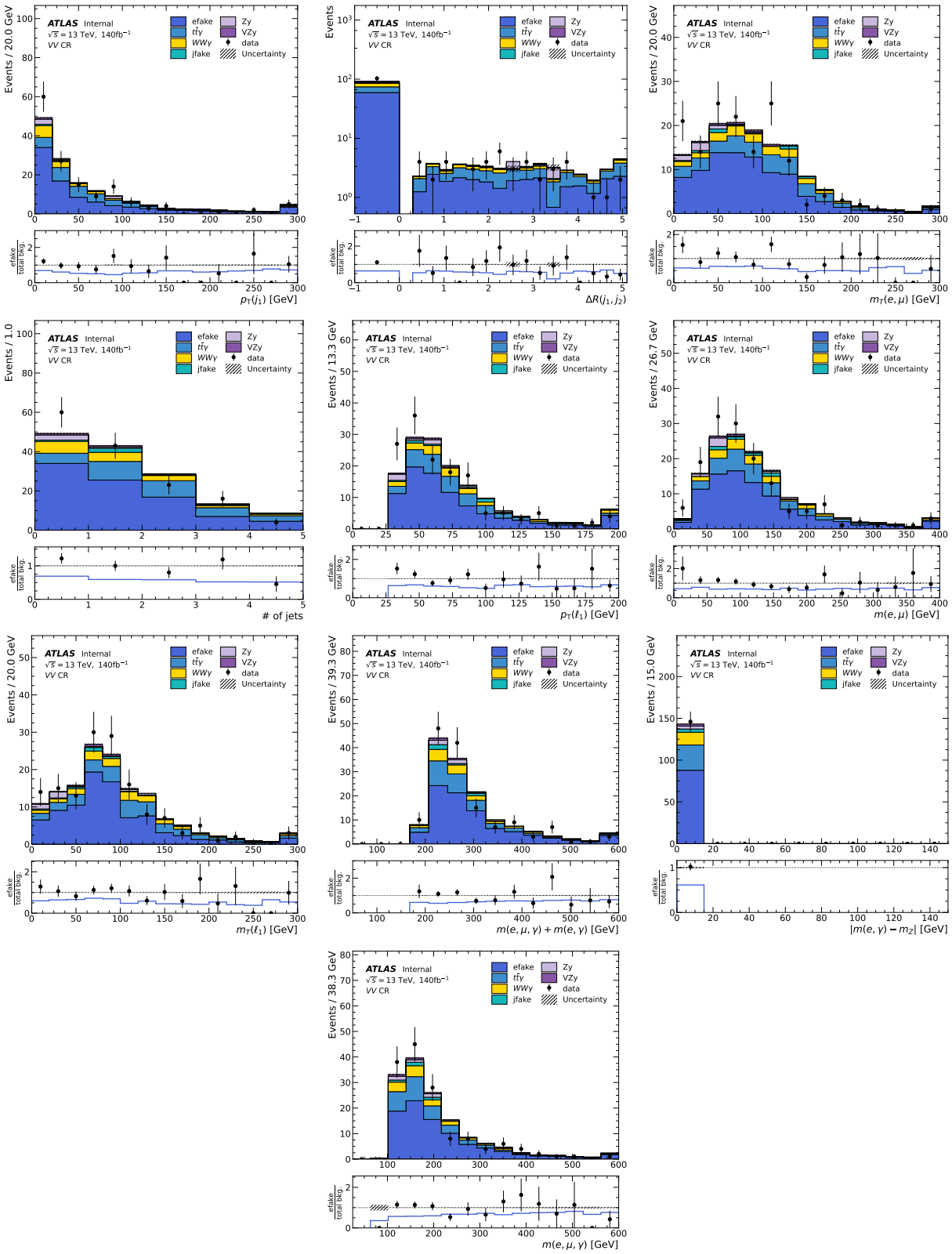

Figure 4.13: Various kinematic distributions in the VV CR. Uncertainty is statistical only. Last bin includes overflow. $\Delta R(j_1, j_2) < 0$ indicates < 2 jets in the event.

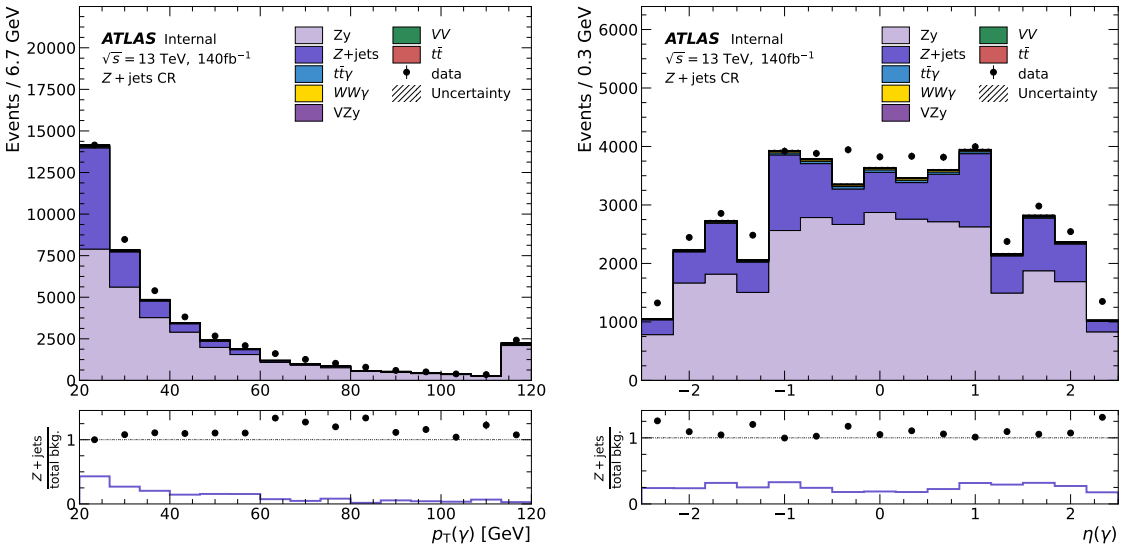

Figure 4.14: Kinematic distributions in the Z + jets CR. Uncertainty is statistical only. Last bin includes overflow.

Z + jets CR The $e^{\pm}\mu^{\mp}\gamma$ SR contains a small contribution from jets misidentified as photons, which is estimated with a data-driven method (Section 5.1.1). We assume that the fake photon processes are independent of the associated leptons in the event, so the events vetoed from the $Z\gamma$ CR with high $m(\ell\ell\gamma)$ form the Z + jets CR in which the data-driven estimate is performed. The Z + jets CR is defined with the same criteria as the $Z\gamma$ CR but with the $m(\ell\ell\gamma)$ cut inverted. Despite the cut inversion, this region is still dominated by the $Z\gamma$ process with prompt photons. Distributions of kinematic variables relevant to the analysis in the Z + jets CR are plotted in Figure 4.14.

$e\gamma$ and $e^{\pm}e^{\mp}$ CRs The data-driven estimate of fake/non-prompt photons from electrons is performed using events in the $e\gamma$ and $e^{\pm}e^{\mp}$ CRs, defined in Table 4.6. These regions are designed to be pure samples of $Z \to e^{\pm}e^{\mp}$ events, with the $e\gamma$ CR containing events in which one of the electrons was misidentified as a photon. Distributions of kinematic variables relevant to the analysis in the $e\gamma$ and $e^{\pm}e^{\mp}$ CRs are plotted in Figure 4.15.

	$e\gamma$ CR	$e^{\pm}e^{\mp}$ CR
# of electrons	1	2
# of photons	1	0
Leading lepton p_{T}	> 27 GeV	> 27 GeV
# of b-jets	0	0
$\lvert m(e,\gamma) - m_Z \rvert$	≤ 30 GeV	–
$\lvert m(e,e) - m_Z \rvert$	–	≤ 30 GeV

Table 4.6: Definitions of the $e\gamma$ and $e^{\pm}e^{\mp}$ CRs.

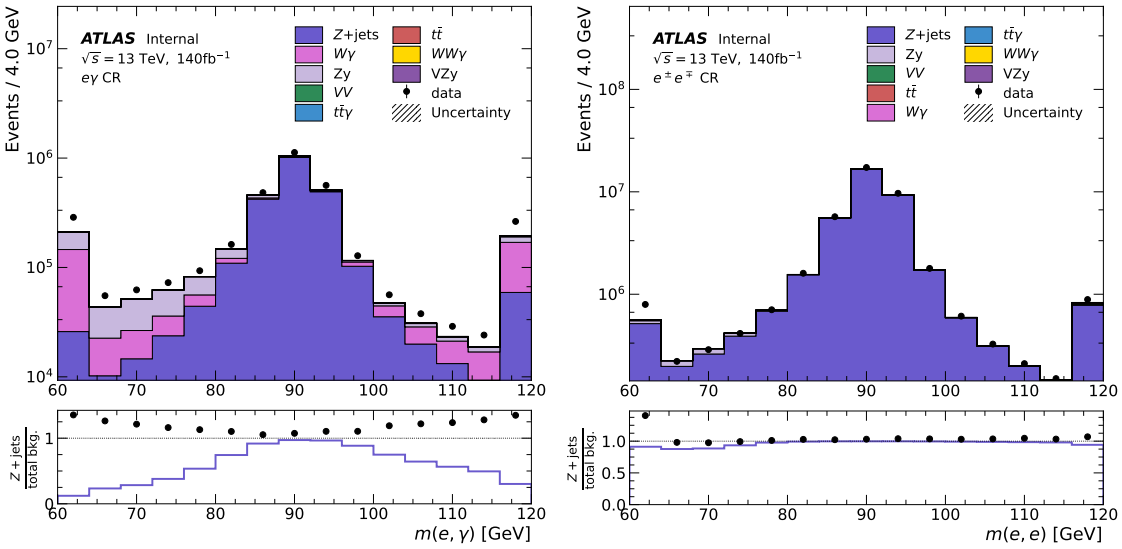

Figure 4.15: $m(e,\gamma)$ distributions in the $e\gamma$ and $e^{\pm}e^{\mp}$ CRs. Uncertainty is statistical only. First and last bins include underflow and overflow.

4.3 Samples

This section describes the data sample recorded by the ATLAS detector as well as Monte Carlo (MC) simulation samples for each physics process expected to contribute to the $e^{\pm}\mu^{\mp}\gamma$ SR and control regions. The MC samples were produced with various event generator software packages that implement the SM (and EFT model) and accordingly represent the theoretical predictions of the analysis. Each event is processed through a simulation of the ATLAS detector. Some physics processes are simulated with a full simulation of the ATLAS detector provided by the GEANT4 software package[82], and others are processed with a fast simulation that implements a simplified model of ECal and HCal[83]. Unless otherwise mentioned, all MC samples in this analysis use the full GEANT4 detector simulation.

Often the predictions of MC simulations are not perfect and must be corrected to match real data. In particular, MC simulations are known to poorly model processes marred by detector effects, shortcomings of event reconstruction algorithms, misidentified particles, low resolution measurements, etc. These shortcomings are addressed with data-driven methods for processes especially sensitive to these effects, in particular Sections 5.1.1 and 5.1.2 address events in which a jet or an electron was misidentified as a photon.

The effects of pileup (see Figure 3.3) must be accounted for in MC samples in order to properly compare to real data. This is accomplished by injecting additional minimum-bias interactions (i.e. the most common events which the trigger was designed to reject) simulated with Pythia 8.186[84] using the A3 tune[85] parameter set. Pileup conditions changed over the course of the three data-taking years, so MC events are reweighted to match the pileup distribution observed in data.

MC event generators are subject to theoretical uncertainties, namely uncertainty in the choice of renormalization and factorization scales μ_R and μ_F, as well as the choice of parton distribution function (PDF). Typically MC samples are generated with arbitrary choices and are reweighted with alternate values to determine the envelope of theoretically acceptable results, which factors into the overall systematic uncertainty of the analysis.

Data

The data used in this thesis was recorded by the ATLAS detector during LHC run-2 encompassing the years 2015-2018. This dataset comprises 140 $\text{fb}^{-1} \pm 0.83\%$ of integrated luminosity[86] from proton-proton collisions with center-of-mass energy $\sqrt{s} = 13$ TeV.

Data events are required to pass trigger requirements[87, 88, 89] in order to be recorded for offline analysis. The triggers used in the $W^{\pm}W^{\mp}\gamma$ analysis are summarized in Table 4.7; each event is required to pass at least one single-electron or single-muon trigger. Furthermore, trigger-matching requirements are imposed on reconstructed electrons and muons in the event, requiring them to match the corresponding trigger-level objects. The single-electron triggers require a track in the event matched to a calorimeter cluster while the single-muon triggers require a track reconstructed in both the ID and MS. Quality criteria are then applied to these primitive trigger objects. LHC luminosity increased significantly between 2015 and 2016 leading to stricter trigger requirements. Data from 2015 triggered on medium electrons with $E_{\text{T}} > 24$ GeV and loose muons with $p_{\text{T}} > 20$ GeV, while data from 2016-2018 triggered on tight electrons with $E_{\text{T}} > 26$ GeV and medium muons with $p_{\text{T}} > 26$ GeV. To improve efficiency at high E_{T} (or p_{T}), additional triggers with looser working points are available.

Some preselection criteria are applied to data events[90]. Data is recorded by ATLAS in

Year	Electron triggers	Muon triggers
2015	HLT_e24_lhmedium_L1EM20VH HLT_e60_lhmedium HLT_e120_lhloose	HLT_mu20_iloose_L1MU15 HLT_mu50
2016–2018	HLT_e26_lhtight_nod0_ivarloose HLT_e60_lhmedium_nod0 HLT_e140_lhloose_nod0	HLT_mu26_ivarmedium HLT_mu50

Table 4.7: Triggers used in the $W^{\pm}W^{\mp}\gamma$ analysis.

lumi-blocks corresponding to about 1 minute of data acquisition; events used in the $W^{\pm}W^{\mp}\gamma$ analysis are required to belong to lumi-blocks on the Good Runs List (GRL) which logs lumi-blocks recorded during stable LHC beams while the ATLAS detector is functioning properly. Additionally, every event is required to have a primary vertex. Furthermore, event cleaning requirements[91] are imposed to reject certain non-collision backgrounds: namely beam-induced background, cosmic ray showers, and calorimeter noise from pathological cells.

$\mathbf{W^{\pm}W^{\mp}\gamma}$

The signal MC sample was generated with the Sherpa 2.2.11[92] event generator package using the NNPDF3.0 NNLO PDF set[93]. This sample includes all processes resulting in the $\ell\nu\ell\nu\gamma$ final state including $W^{\pm}W^{\mp}\gamma$, same-charge $W^{\pm}W^{\pm}\gamma$, and $VZ\gamma$ with $Z \to \tau^{\pm}\tau^{\mp}$ in the leptonic τ decay channel. $t\bar{t}\gamma \to W^{\pm}bW^{\mp}b\gamma$ events are removed with a generator-level veto on b quarks. The matrix element was computed at NLO for the case of zero additional jets, and at LO the using the Comix [94] and OpenLoops[95, 96, 97] libraries when up to two additional final-state jets may be present. The matrix elements were matched with the Sherpa parton shower [98] using the ME+PS@NLO prescription[99, 100, 101, 102] using the set of tuned parameters developed by the Sherpa authors.

$W^{\pm}W^{\mp}\gamma$ aQGC

Samples describing the contributions of a dimension-8 EFT model[45] to the $W^{\pm}W^{\mp}\gamma$ process were generated with MadGraph 2.9.9[103] at LO interfaced with Pythia 8.3[84] using the NNPDF3.0 NNLO PDF set[93]. The implementation of the EFT model is provided by Eboli[104]. The contributions of each EFT operator were generated separately from the others, i.e. in each EFT sample only one operator has non-zero Wilson coefficient. The samples were generated with Wilson coefficient value 1 TeV^4/Λ^4. The EFT samples are decomposed into QUAD and SMINT parts as described in Section 6.1, allowing for rescaling to different values of Wilson coefficient.

Additionally, a SM $W^{\pm}W^{\mp}\gamma$ sample was generated with MadGraph under the same settings as the EFT samples in order to correct the EFT samples for differences with the nominal $W^{\pm}W^{\mp}\gamma$ Sherpa sample. The notable differences are:

- The Sherpa sample generates the $W^{\pm}W^{\mp}\gamma$ process at NLO while the MadGraph implementation of the EFT model only permits events generation at LO.
- The Sherpa sample generates the $\ell\nu\ell\nu\gamma$ process including off-shell W bosons as well as others while the MadGraph sample only includes on-shell $W^{\pm}W^{\mp}\gamma$ production.
- The Sherpa sample includes 0-2 additional LO jets in the final state while the MadGraph samples contain no additional jets.
- The MadGraph samples were generated with `aEWM1` set to ~ 128 resulting in a Z mass of 79.82 GeV, while the Sherpa samples were generated with the correct value of Z mass.

The ATLAS detector simulation software is very CPU intensive, so to save time a generator filter requiring exactly one electron and one muon with $p_{\mathrm{T}} > 15$ GeV was applied to these MadGraph samples before detector simulation. The generator filter efficiency is in the range 1-5% depending on the specific sample.

$\mathbf{t\bar{t}\gamma}$

The $t\bar{t}\gamma$ process was produced with the MadGraph5_aMC@NLO 2.7.3[103] event generator with the NNPDF3.0 NNLO PDF set[93] interfaced with Pythia 8.240[84] using the A14 tune[105] parameter set. Additionally, $tW\gamma$ production is included under the umbrella of $t\bar{t}\gamma$ in this analysis as it only differs from $t\bar{t}\gamma$ by an additional b jet. The $t\bar{t}\gamma$ and $tW\gamma$ processes are each composed of two subprocesses generated separately and combined afterward: direct $t\bar{t}\gamma$ ($tW\gamma$) production and $t\bar{t}$ (tW) with a final-state photon radiated from a top quark or its decay products. The decays of the top quarks of the $t\bar{t}\gamma$ samples were processed with MadSpin[106]. The decays of b and c quarks were processed with EvtGen[107]. The GEANT4 full detector simulation was used to produce the $t\bar{t}\gamma$ samples and the fast simulation was used to produce the $tW\gamma$ samples.

$\mathbf{Z\gamma}$

The $Z\gamma$ process was produced with Sherpa 2.2.8[92] at NLO using the NNPDF3.0 NNLO PDF set[93]. The matrix elements were computed at NLO for the case of 0-1 additional jets, and at LO using the Comix [94] and OpenLoops[95, 96, 97] libraries when 2 or 3 additional final-state jets may be present. The matrix elements were matched with the Sherpa parton shower [98] using the ME+PS@NLO prescription[99, 100, 101, 102] using the set of tuned

parameters developed by the SHERPA authors. Events with off-shell Z bosons are included. The $Z\gamma$ sample was generated in four parts according to final state which are combined afterward: $ee\gamma$, $\mu\mu\gamma$, $\tau\tau\gamma$, and $\nu\nu\gamma$.

VZγ

The $VZ\gamma$ process was generated in two parts and combined afterward: $WZ\gamma$ with SHERPA 2.2.11[92] at NLO and $ZZ\gamma$ with SHERPA 2.2.5 at NLO. Both processes were generated with the NNPDF3.0 NNLO PDF set[93]. The matrix elements were computed at NLO for the case of 0 additional jets, and LO using the Comix [94] and OPENLOOPS[95, 96, 97] libraries when up to two (for $WZ\gamma$) or up to three (for $ZZ\gamma$) additional final-state jets may be present. The matrix elements were matched with the SHERPA parton shower [98] using the ME+PS@NLO prescription[99, 100, 101, 102] using the set of tuned parameters developed by the SHERPA authors. Events with off-shell W and Z bosons were included. The allowed final states are $\ell\ell\ell\nu\gamma$ for $WZ\gamma$ and $\ell\ell\ell\ell\gamma$ for $ZZ\gamma$.

VV

Diboson processes, namely WW, WZ, and ZZ production, were generated with SHERPA 2.2.1 [92] (semileptonic final states) and SHERPA 2.2.2 (fully leptonic final states). Loop-induced $gg \to VV$ processes use the CT10 PDF set[108] while the others use the NNPDF3.0 NNLO PDF set[93]. Samples were generated separately per final state and combined afterward, but zero, one, and four lepton final states were neglected in this analysis due to their negligible contribution. The samples include off-shell W, Z as well and Higgs processes. The matrix elements were computed at NLO for the case of 0-1 additional jets, and at LO using the

Comix [94] and OpenLoops[95, 96, 97] libraries when up to three additional final-state jets may be present. The matrix elements were matched with the Sherpa parton shower [98] using the ME+PS@NLO prescription[99, 100, 101, 102] using the set of tuned parameters developed by the Sherpa authors.

$t\bar{t}$

The $t\bar{t}$ process was generated with the PowhegBox v2[109, 110, 111, 112] event generation software package with the NNPDF3.0 NNLO PDF set[93] and the h_{damp} parameter set to 1.5× the top quark mass. The parton shower was modelled by Pythia 8.230[84] using the A14 tune[105] parameter set and the NNPDF2.3 LO PDF set[113]. The decays of b and c quarks were processed with EvtGen[107]. The tW process is included under the umbrella of $t\bar{t}$ in this analysis as it only differs from $t\bar{t}$ by an additional b jet. tW production was also modelled by PowhegBox v2[114]. The diagram removal scheme[115] was used to remove interference and overlap with the $t\bar{t}$ process.

Z+jets

The production of Z+jets was simulated with the Sherpa 2.2.1[92] generator using NLO matrix elements for up to two partons, and LO matrix elements for up to four partons calculated with the Comix [94] and OpenLoops[95, 96, 97] libraries. They were matched with the Sherpa parton shower [98] using the ME+PS@NLO prescription[99, 100, 101, 102] using the set of tuned parameters developed by the Sherpa authors. The NNPDF3.0 NNLO set of PDFs[93] was used and the samples were normalised to a NNLO prediction[116].

Chapter 5

Measurement of $pp \to W^{\pm}W^{\mp}\gamma$ cross section

5.1 Data-driven backgrounds

To each physics process present in the $e^{\pm}\mu^{\mp}\gamma$ SR with a prompt photon ($W^{\pm}W^{\mp}\gamma$, $t\bar{t}\gamma$, $Z\gamma$, $VZ\gamma$), a corresponding process without a prompt photon (VV, $t\bar{t}$, $Z+\text{jets}$) can be present, as well if a photon is mis-reconstructed from another object. This can occur if the photon is from a misidentified jet or electron ("fake" photon) or if the photon is radiated from a final-state jet or electron ("non-prompt" photon). MC simulations are known to poorly model events with misidentified and/or non-prompt photons. The uncorrected contributions of these processes are listed in Table 5.1. This section describes the data-driven methods used to correct MC samples in the $e^{\pm}\mu^{\mp}\gamma$ SR containing these events in two cases: fake photons from jets and fake photons from electrons.

5.1.1 Jets misidentified as photons

The $Z+\text{jets}$ CR, defined in Section 4.2, is used to correct MC mismodelling of events in which a jet is misidentified as a photon or a non-prompt photon is radiated from a jet. We assume that the $j \to \gamma$ fake rate does not depend on the flavor of the associated leptons in

	$e^{\pm}\mu^{\mp}\gamma$ SR
$t\bar{t}$	20 ± 6
Diboson	13 ± 1.3
$Z+\text{jets}$	11 ± 7
Total	40 ± 6

Table 5.1: Contributions to the $e^{\pm}\mu^{\mp}\gamma$ SR from physics processes without a prompt photon.

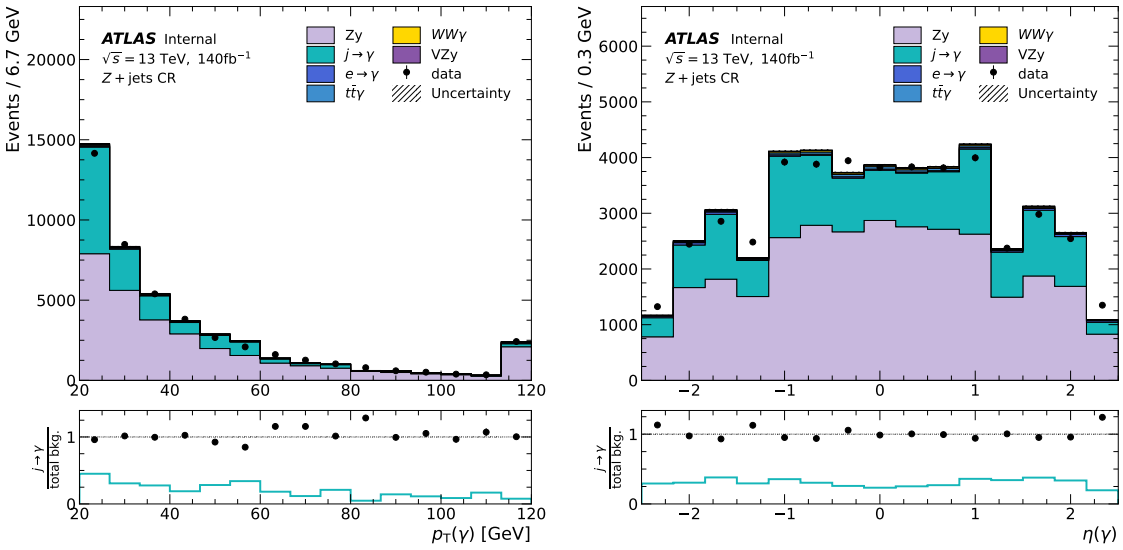

Figure 5.1: Kinematic distributions in the $Z+$jets CR with $j \to \gamma$ SF applied. Uncertainty is statistical only. Last bin includes overflow.

the event, allowing MC correction scale factors (SFs) derived in this region to be applied to $j \to \gamma$ MC events in the $e^{\pm}\mu^{\mp}\gamma$ SR.

In the $Z+$jets CR, The $Z+$jets process represents fake/non-prompt photons and can be used to estimate the contribution of these events to the data. Figure 4.14 shows plots of kinematic variables in the $Z+$jets CR, where it can be seen that $j \to \gamma$ events represent about 30% of the total. To obtain an estimate of the number of $j \to \gamma$ events in the data, the large contributions from $Z\gamma$ (plus other prompt processes) must be subtracted off. MC correction scale factors for $j \to \gamma$ events are computed as

$$\text{SF} = \frac{N(\text{data}) - N(\text{prompt MC})}{N(j \to \gamma \text{ MC})}. \tag{5.1}$$

The $Z+$jets CR after correcting $j \to \gamma$ MC is plotted in Figure 5.1.

Systematic uncertainties on the SFs were estimated from two contributions:

1. statistical uncertainty on the numbers of events used to calculate the SFs, and

2. a 30% overall uncertainty derived from the ABCD method.

The ABCD method for estimating background contributions to a SR works by partitioning phase space into four regions. In this case, we partition events of the $e^{\pm}\mu^{\mp}\gamma$ SR with loosened photon criteria based on photon ID and isolation requirements:

- region A: $e^{\pm}\mu^{\mp}\gamma$ SR events that fail tight photon ID and isolation requirements,
- region B: $e^{\pm}\mu^{\mp}\gamma$ SR events that pass tight photon ID requirements but fail isolation requirements,
- region C: $e^{\pm}\mu^{\mp}\gamma$ SR events that fail tight photon ID requirements but pass isolation requirements, and
- region D: $e^{\pm}\mu^{\mp}\gamma$ SR events that pass both tight photon ID requirements and isolation requirements.

If we assume that photon ID and isolation requirements are not correlated, then we can assume that the ratio of isolated to non-isolated photons is independent of whether the photons pass the ID requirement

$$\frac{N_D}{N_B} = \frac{N_C}{N_A}, \tag{5.2}$$

where the N's represent the number of data events with prompt photon MC subtracted off like Equation (5.1). As region D is essentially the nominal $e^{\pm}\mu^{\mp}\gamma$ SR, we could use this equality to directly estimate the contribution of fake, non-prompt photons in the SR. However, due to the limited statistics and low purity of the $e^{\pm}\mu^{\mp}\gamma$ SR this method gives a high uncertainty. Instead, region D associated with the $Z\gamma$ CR (without the $m(\ell,\ell,\gamma)$ cut)

is used to compute a scale factor that is applied to the $e^{\pm}\mu^{\mp}\gamma$ SR under the assumption that the $j \to \gamma$ fake rate does not depend on the associated leptons in the final state:

$$N_{\text{corr}}^{e^{\pm}\mu^{\mp}\gamma} = \frac{N_D^{Z\gamma}}{N_{j\to\gamma,\text{MC}}^{Z\gamma}} \times N_{\text{MC}}^{e^{\pm}\mu^{\mp}\gamma}, \tag{5.3}$$

This results in ∼30% uncertainty in $N_{\text{corr}}^{e^{\pm}\mu^{\mp}\gamma}$ arising mostly from the low purity of tight, non-isolated photon events in the $Z\gamma$ and $Z+$jets CRs. Applying this method to the $Z+$jets CR instead of the $e^{\pm}\mu^{\mp}\gamma$ SR gives an estimate consistent with Figure 5.1 within uncertainties. We proceed in the $W^{\pm}W^{\mp}\gamma$ analysis by using the scale factors of Equation (5.1) in the $e^{\pm}\mu^{\mp}\gamma$ SR but with a 30% overall systematic uncertainty on the $j \to \gamma$ contribution.

5.1.2 Electrons misidentified as photons

Events in the $e^{\pm}\mu^{\mp}\gamma$ SR with $m(e,\gamma)$ near m_Z are vetoed to remove contamination from events from $Z \to e^+e^-$ in which an electron was misidentified as a photon. Figure 5.2 shows the distribution of $m(e,\gamma)$ in the $e^{\pm}\mu^{\mp}\gamma$ SR and the VV CR, in which the $m(e,\gamma)$ cut is inverted. The $e \to \gamma$ events that remain in the $e^{\pm}\mu^{\mp}\gamma$ SR are poorly modelled by MC simulations, so a data-driven method is used to reweight MC events passing one of two criteria:

1. a reconstructed photon is matched to an electron in the MC truth record, or

2. a photon is reconstructed within $\Delta R < 0.1$ of an electron in the MC truth record.

These events are reweighted with a scale factor, binned in $p_{\mathrm{T}}(\gamma)$ and $|\eta(\gamma)|$, defined as the ratio of $e \to \gamma$ fake rates as computed in in data and MC:

$$\mathrm{SF}(p_{\mathrm{T}}, |\eta|) = \frac{\mathrm{FR}_{\mathrm{data}}(p_{\mathrm{T}}, |\eta|)}{\mathrm{FR}_{\mathrm{MC}}(p_{\mathrm{T}}, |\eta|)}. \tag{5.4}$$

The fake rates are computed in the $e\gamma$ and $e^{\pm}e^{\mp}$ CRs, defined in Section 4.2. We assume that the MC simulation's mismodelling of $e \to \gamma$ fake events in the $Z \to e^{\pm}e^{\mp}$ channel is similar to the $VZ \to Ve^{\pm}e^{\mp}$ events of the $e^{\pm}\mu^{\mp}\gamma$ SR, i.e., that the mechanism causing the photon reconstruction algorithm to fail on $Z \to e^{\pm}e^{\mp}$ events is independent of any other objects present in the event. As can be seen from Figure 4.15 there is some contribution from other backgrounds that must be subtracted off. To accomplish this, the $m(e, \gamma)$ and $m(e, e)$ distributions are fit to a parametric model with the $Z \to e^{\pm}e^{\mp}$ signal modelled by a Breit-Wigner distribution $\circledast$ Crystal Ball distribution ($\circledast$ denotes convolution) and the background modelled by a 5th order Bernstein polynominal. The Breit-Wigner models Z decay so its width is fixed to 2.49 GeV, i.e. the Z decay width[13], but its mean is free in the fit. The fits were performed in the range 70 GeV $< m(e\gamma), m(e, e) >$ 110 GeV. The fit was performed independently for $e\gamma$ and $e^{\pm}e^{\mp}$, MC and data, in each of 25 $(p_{\mathrm{T}}, |\eta|)$ bins for a total of 100 fits; some fits to this model are plotted in Figure 5.3. The numbers of $Z \to e^{\pm}e^{\mp}, e\gamma$ signal events $N(e^{\pm}e^{\mp}), N(e\gamma)$ are extracted from the fits as the integrals of the signal models, and the fake rates are computed as

$$\mathrm{FR} = \frac{N(e\gamma)}{N(e^{\pm}e^{\mp})}. \tag{5.5}$$

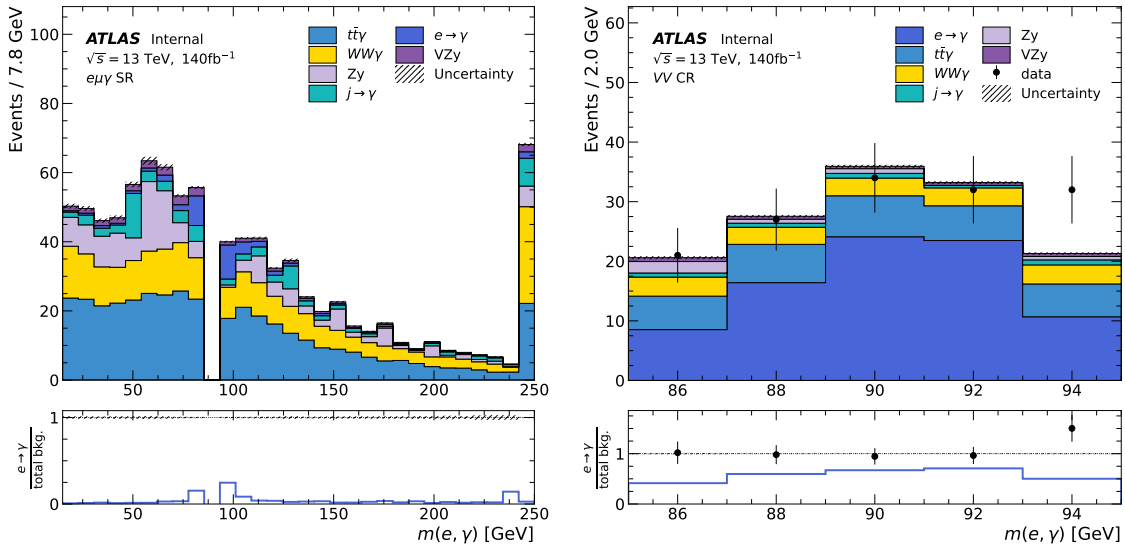

Figure 5.2: $m(e,\gamma)$ in the $e^{\pm}\mu^{\mp}\gamma$ SR and VV CR.

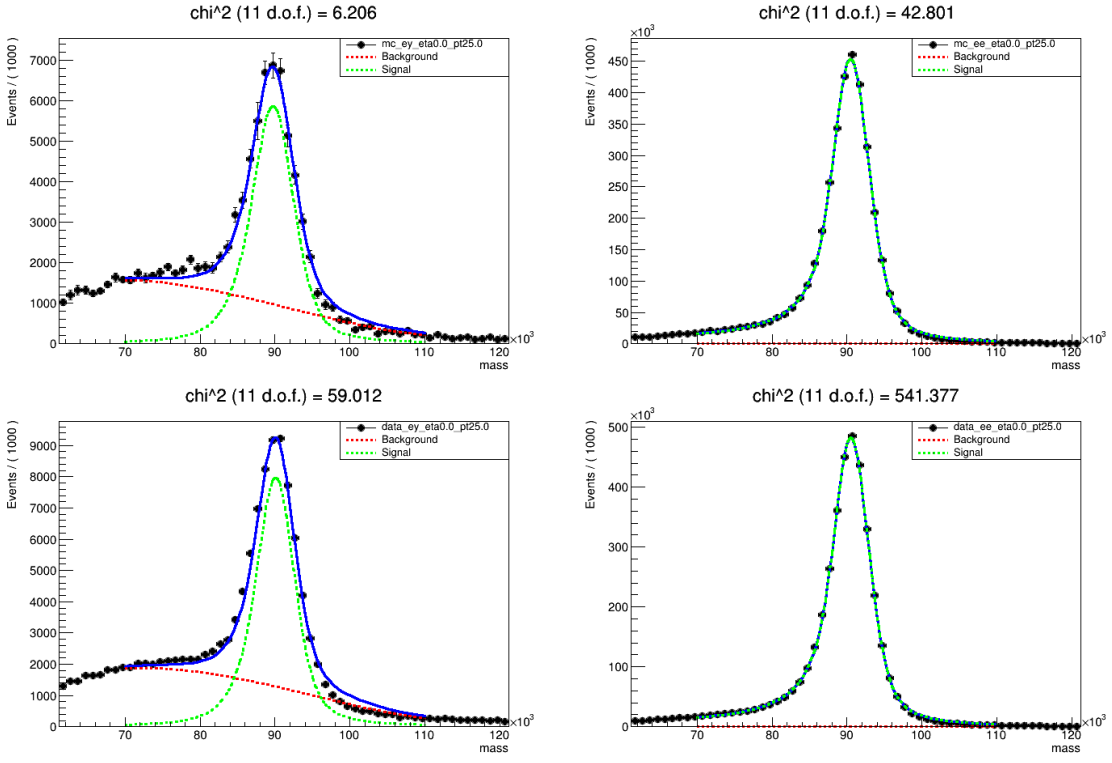

Figure 5.3: Fits of $Z \to e\gamma$ and $Z \to e^{\pm}e^{\mp}$ to Breit-Wigner $\circledast$ Crystal Ball + 5th order Bernstein polynomial in the bin with $p_{\mathrm{T}} < 25$ GeV and $|\eta| < 0.5$. (Top left) MC $e\gamma$, (Top right) MC $e^{\pm}e^{\mp}$, (Bottom left) data $e\gamma$, (Bottom right) data $e^{\pm}e^{\mp}$.

The $e \to \gamma$ SF values are plotted in Figure 5.4 and the $e\gamma$ CR is plotted in Figure 5.5 with the SFs applied.

Systematic uncertainties on the SFs were estimated by repeating the procedure with the following variations:

1. $N(e\gamma)$ and $N(e^{\pm}e^{\mp})$ were varied up and down according to the uncertainty of the $Z \to e^{\pm}e^{\mp}$ signal model from the fits.

2. The $m(e,\gamma)$ and $m(e,e)$ ranges considered in the fit were expanded by 5 GeV in both directions.

3. The $m(e,\gamma)$ and $m(e,e)$ ranges considered in the fit were shrunk by 5 GeV in both directions.

4. The background model was replaced with a 4th order Bernstein polynomial.

These systematic uncertainties are modelled with nuisance parameters in the binned maximum likelihood fit of Section 5.3, the associated pull distributions are found in Figure 5.16.

5.2 Machine learning

The $e^{\pm}\mu^{\mp}\gamma$ SR contains about 26% $W^{\pm}W^{\mp}\gamma$ events and about 74% background (see Table 4.5). To obtain a more pure sample of $W^{\pm}W^{\mp}\gamma$ signal MC events to fit to data, a boosted decision tree (BDT) was trained on MC events of the $e^{\pm}\mu^{\mp}\gamma$ SR and the resulting discriminant was used to define the binned likelihood of Section 5.3. A BDT combines the signal/background discriminating power of several kinematic variables into a real-valued discriminant, essentially

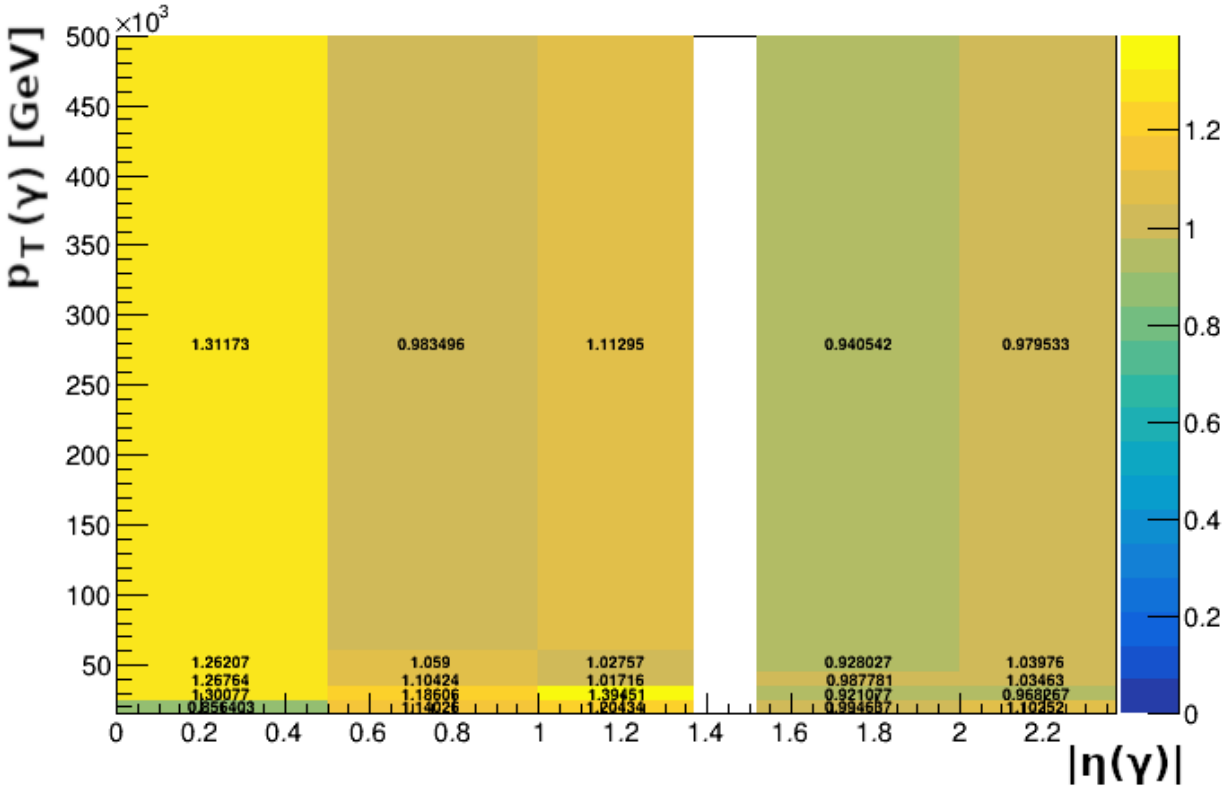

Figure 5.4: The values of the $e \to \gamma$ SFs in bins of $(p_{\mathrm{T}}(\gamma), |\eta(\gamma)|)$.

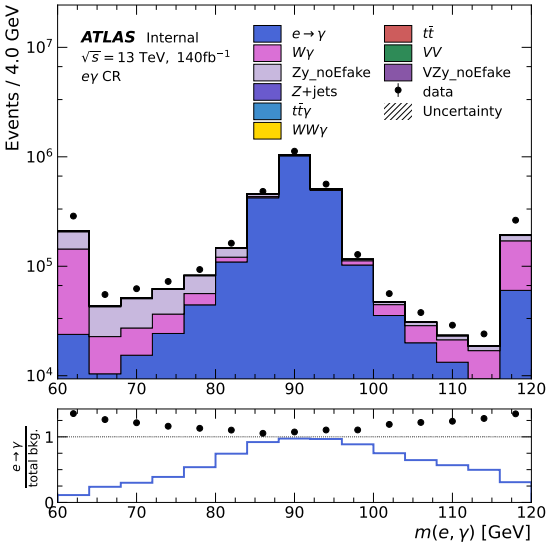

Figure 5.5: $m(e, \gamma)$ in the $e\gamma$ CR after $e \to \gamma$ SFs are applied.

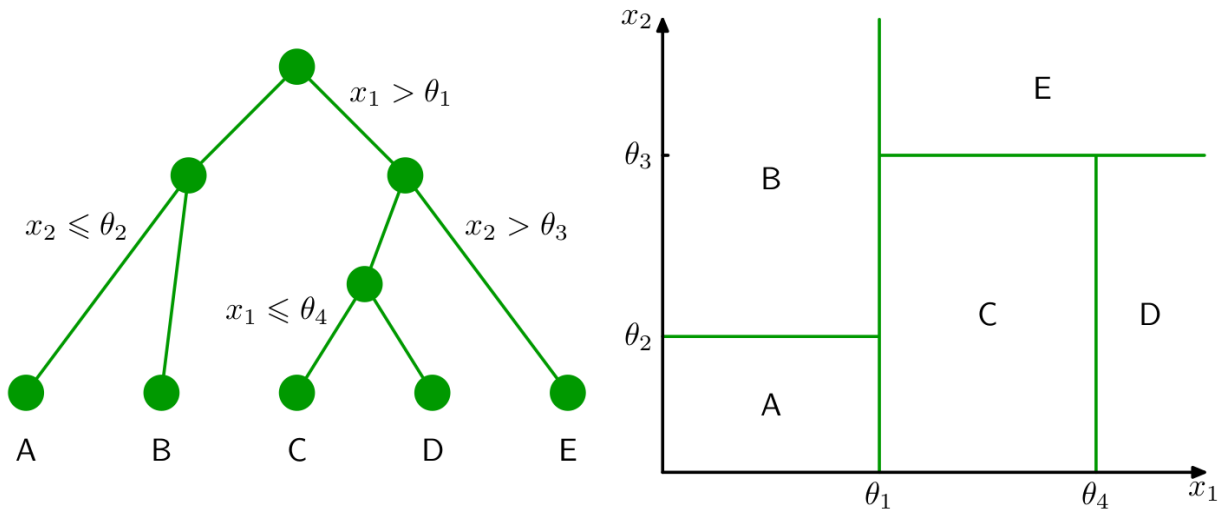

Figure 5.6: (Left) an example decision tree that classifies events into 5 categories A-E based on input variables x_1, x_2 and thresholds $\theta_1 - \theta_4$. (Right) The example decision tree partitions input variable space into regions. In the $W^{\pm}W^{\mp}\gamma$ analysis the BDT partitions a 10-dimensional input space into 2 categories. Source: Ref. [118].

a confidence score that the input event is a $W^{\pm}W^{\mp}\gamma$ signal event as opposed to a background event. The XGBoost[117] Python package was used to implement the BDT.

A BDT is an ensemble of K decision trees; a decision tree is illustrated in Figure 5.6. XGBoost uses classification and regression trees (CART), which assign each leaf node of the trees a weight w_k. The BDT discriminant $\hat{y}(x)$ is evaluated on an event x by summing the weights of each CART in the ensemble according to the leaf node arrived at by evaluating the tree's cuts on the event's kinematic variables:

$$\hat{y}(x) = \sum_{k=1}^{K} \hat{y}^{(k)}(x) = \sum_{k=1}^{K} w_k(x). \tag{5.6}$$

XGBoost extends the predictive power of a single CART by training with the gradient boosting algorithm, in which additional trees are trained that perform better on events misclassified by preceding trees. Given a training set of n input vectors $\{x_i\}$ and targets $\{y_i\}$,

The BDT discriminant $\hat{y}_i(x_i)$ is trained iteratively, adding one tree $f_t(x_i)$ at a time:

$$\hat{y}_i^{(0)} = 0, and \tag{5.7}$$

$$\hat{y}_i^{(t)} = \hat{y}^{(t-1)} + f_t(x_i), \tag{5.8}$$

such that the objective function $\mathcal{L}^t = \sum_{i=1}^{n} l(y_i, \hat{y}_i^{(t-1)} + f_t(x_i)) + \Omega(f_t)$ is minimized, where $l(y_i, \hat{y}_i)$ is an arbitrary differentiable loss function and $\Omega(f_t)$ is a regularization term to control model complexity. The loss function quantifies the difference (the "residual") between the prediction $\hat{y}_i$ and the training target y_i.

XGBoost uses a greedy algorithm during training to determine the structure of individual trees based on the minimization of this objective function. The greedy algorithm iteratively adds nodes to a tree by evaluating several proposed splits of the input space and choosing the one that best minimizes the objective function for each iteration step.

The BDT for the $W^{\pm}W^{\mp}\gamma$ analysis was trained using 5-fold cross-validation, in which 5 BDTs are each trained on (5-1)/5 = 80% of MC events in the $e^{\pm}\mu^{\mp}\gamma$ SR and the remaining 20% are set aside as a test set to evaluate the performance of the BDT. This procedure is repeated 5 times such that each event appears in one test set. The BDT's performance is determined using the receiver operating characteristic (ROC) curve. The ROC curve is obtained from the BDT output by evaluating the true positive rate (type-I error rate) and false positive rate (type-II error rate) for each event in the training and test sets. The ROC curve of the BDT trained in the $e^{\pm}\mu^{\mp}\gamma$ SR is plotted in Figure 5.7. The area under the ROC curve (AUC) quantifies the performance of the BDT as we want a BDT with low false positive rate and high true positive rate.

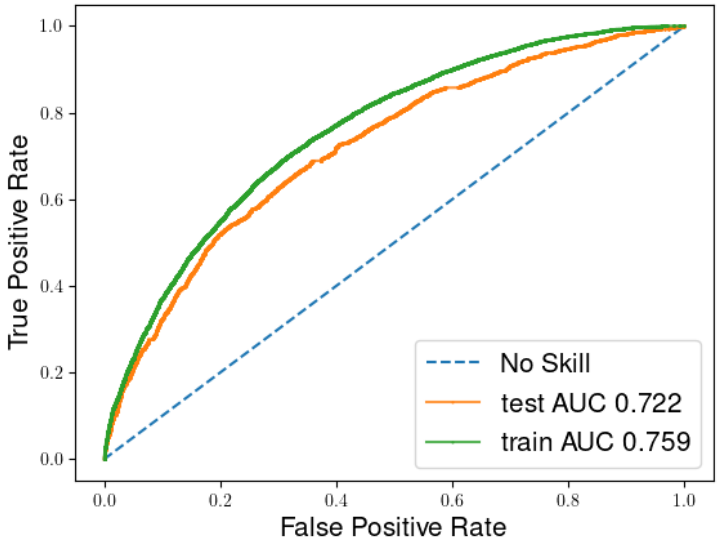

Figure 5.7: ROC curves for the training and test set of one fold of the BDT in the $e^{\pm}\mu^{\mp}\gamma$ SR.

The input variables selected for the $W^{\pm}W^{\mp}\gamma$ analysis are the 10 kinematic variables out of a pool of ∼100 with highest feature importance as evaluated by XGBoost. They are listed in Table 5.3 and plotted in the SR and CRs in Section 4.2. The BDT hyperparameters for the $W^{\pm}W^{\mp}\gamma$ analysis were optimized by training many BDTs and selecting the one that maximizes the AUC score on the test set. The optimized hyperparameters are listed in Table 5.2. The meanings of the hyperparameters are:

- **Number of trees**— The number of trees to train in the BDT.
- **Max tree depth**— The maximum number of sequential cuts allowed for each tree.
- **Event subsample**— The fraction of events used in the training.
- **Variable subsample**— The fraction of input variables used in the training.
- **Min. child weight**— The minimum number of training samples required for each leaf node in a CART.

- **Learning rate**— A constant factor multiplied to every CART's leaf node weights. A smaller learning rate increases CPU time required for training but can improve the granularity of gradient calculations during minimization the objective function.

- **L2 regularization**— Adds a ridge regression term to the objective function, i.e. a regularization term of the form

$$\frac{\lambda}{2}\sum_{j=1}^{J}|w_j|^2. \tag{5.9}$$

  This term penalizes large leaf node weights w_j in the training.

This method of hyperparameter optimization may introduce some bias into the BDT, i.e. it may not perform as well in general on experimental data as it does on the test set, because the test set itself is used to choose the hyperparameters. Ideally, an independent set of MC events (a "validation set") should be used to perform the hyperparameter. However, MC event generation and detector simulation accounted for over 65% of the ATLAS experiment's computing resources during LHC run-2[119], so generating additional MC events is very costly. We instead accept a potential small reduction in BDT performance due to bias in order to make use of all available MC events in the binned likelihood of Section 5.3 in order to minimize MC statistical uncertainty in the $W^{\pm}W^{\mp}\gamma$ cross section measurement itself. Other published ATLAS analyses, such as Ref. [120], do not typically define a separate validation set to evaluate multivariate algorithms.

The BDT is trained in the $e^{\pm}\mu^{\mp}\gamma$ SR and is applied to events in the SR, as well as the CRs. The BDT distributions of events in the $e^{\pm}\mu^{\mp}\gamma$ SR and CRs are plotted in Figure 5.8, where it can be seen that the BDT tends to assign $W^{\pm}W^{\mp}\gamma$ signal events high discriminant values and background events to low discriminant values. The rightmost histogram bin of

Hyperparameter	Value
Number of trees	120
Max tree depth	4
Event subsample	0.5
Variable subsample	0.5
Min. child weight	1
Learning rate	0.1
L2 regularization	1

Table 5.2: XGBoost BDT hyperparameters used in the $W^{\pm}W^{\mp}\gamma$ analysis.

Variable	Feature importance
$p_{\mathrm{T}}(j_1)$	0.19
$\Delta R(j_1, j_2)$	0.13
$m_T(e, \mu)$	0.11
Number of jets	0.11
$p_{\mathrm{T}}(\ell_1)$	0.10
$m(e, \mu)$	0.09
$m_{\mathrm{T}}(\ell_1)$	0.08
$m(e, \mu, \gamma) + m(e, \gamma)$	0.07
$\lvert m(e, \gamma) - m_Z \rvert$	0.06
$m(e, \mu, \gamma)$	0.06

Table 5.3: BDT input variables used in the $W^{\pm}W^{\mp}\gamma$ analysis, along with the feature importance evaluated by XGBoost.

the $e^{\pm}\mu^{\mp}\gamma$ SR is over 90% pure in $W^{\pm}W^{\mp}\gamma$ signal, which will help constrain the $W^{\pm}W^{\mp}\gamma$ signal normalization in the binned maximum-likelihood fit of Section 5.3.

5.3 Cross section measurement

The data of the $e^{\pm}\mu^{\mp}\gamma$ SR is used to measure the cross section of $W^{\pm}W^{\mp}\gamma$ production as outlined in this section. The main idea is to perform a maximum likelihood fit of the binned BDT distributions of Figure 5.8 to determine the best-fit value of the $W^{\pm}W^{\mp}\gamma$ distribution's normalization factor. The $t\bar{t}\gamma$, $Z\gamma$, and $e \to \gamma$ fake backgrounds' normalization factors are constrained by fits to data in the control regions, along with other nuisance parameters quantifying systematic uncertainties. Once the best-fit $W^{\pm}W^{\mp}\gamma$ normalization factor is known, it can be used to correct the Sherpa MC event generator software's estimate of the $W^{\pm}W^{\mp}\gamma$ cross section (441 fb).

In order to remove potential bias on the part of the experimenters, the ATLAS dataset is blinded until the complete analysis plan is fully documented and validated according to the ATLAS unblinding approval process. At the time of writing, the data is still blinded in the $e^{\pm}\mu^{\mp}\gamma$ SR. Data in the CRs are already unblinded so we can perform measurements of the background contributions but we cannot measure the contribution from $W^{\pm}W^{\mp}\gamma$ itself in the SR. Instead, we define the "Asimov dataset" as a synthetic dataset representing the expected dataset under the assumptions of the theoretical model, in this case the SM. We can perform a fit to the Asimov dataset to determine the expected cross section based on the MC simulations, and later after unblinding approval we will repeat the fit with the same procedure and settings but with the real dataset.

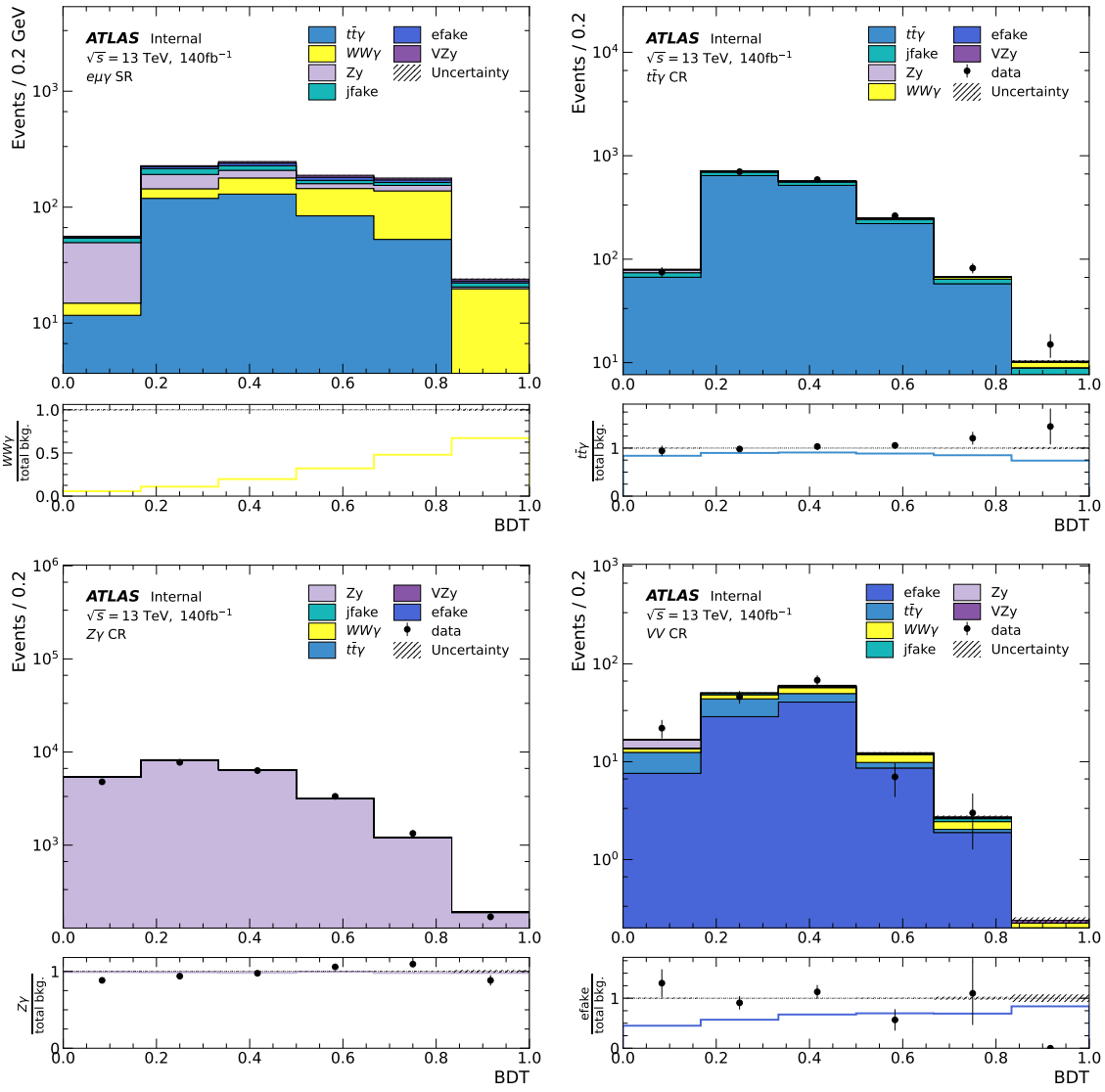

Figure 5.8: BDT distribution in the $e^{\pm}\mu^{\mp}\gamma$ SR (top left), $t\bar{t}\gamma$ CR (top right), $Z\gamma$ CR (bottom left), and VV CR (bottom right).

We use the TRExFitter software package, internal to the ATLAS collaboration, to perform the fit. TRExFitter is based on the HistFactory[121] software packge for building statistical models, which itself is based on the RooStats[122] and RooFit[123] packages integrated into the ROOT software package[124]. The statistical methodology of the binned maximum likelihood fit is based on Ref. [125].

5.3.1 Likelihood function

Consider the histogrammed BDT distribution of the $e^{\pm}\mu^{\mp}\gamma$ SR in Figure 5.8. In each bin, MC simulations of the $W^{\pm}W^{\mp}\gamma$ signal and various backgrounds, along with data-driven estimates of $j \to \gamma$ and $e \to \gamma$ fake photon processes, are summed to give the total expected number of events in that bin. Each bin is essentially a random counting experiment, which is modelled by a Poisson distribution,

$$\text{Pois}(n|\nu) = \frac{\nu^n}{n!}e^{-\nu}, \tag{5.10}$$

where n is the measured event count and ν is the expected event count. In the case of the Asimov dataset, $n = \nu$ by definition. The total expectation can be decomposed into expected signal and expected background terms:

$$\nu_{\text{SR}}(\mu, \boldsymbol{\theta}) = \mu\nu^s(\boldsymbol{\theta}) + \sum_b \nu^b(\boldsymbol{\theta}), \tag{5.11}$$

where μ is the "signal strength" and $\boldsymbol{\theta}$ is a vector of "nuisance parameters" (NPs) to be optimized by the fit. μ is the parameter of interest (POI) of the fit. $\mu = 0$ corresponds to the background-only hypothesis, $\mu = 1$ corresponds perfectly to the prediction of the signal

MC simulation, and other values indicate a mismatch between MC and data. The likelihood function for the whole $e^{\pm}\mu^{\mp}\gamma$ SR can be constructed as a product of Poisson terms, one for each bin i:

$$\mathcal{L}(\mu, \boldsymbol{\theta}) = \prod_i \text{Pois}(n_i|\mu\nu_i^s(\boldsymbol{\theta}) + \sum_b \mu_b\nu_i^b(\boldsymbol{\theta})). \tag{5.12}$$

The $t\bar{t}\gamma$, $Z\gamma$, and $e \to \gamma$ fake background normalizations μ_b are included in the list of NPs; they are constrained by measurements in corresponding CRs in a similar way to μ in the SR. Poisson terms corresponding to the bins of the SR and CRs are included in the likelihood in order to fit the signal and background normalizations simultaneously. The backgrounds without corresponding CRs have μ_b fixed to 1.

Systematic uncertainties in the analysis are modelled by NPs that are optimized in the fit simultaneously with the parameter of interest. Typically the effects of a systematic uncertainty are modelled by variations of the MC simulation with varied values of the NP. The uncertainties on the signal and background expectations σ^s, σ^b are extracted from the envelope of these MC simulations. For example, $\sigma^{j\to\gamma} = 0.3$ as discussed in Section 5.1.1. The signal and background expectations' dependence on the NPs $\boldsymbol{\theta}$ is modelled in the likelihood (Equation (5.12)) as:

$$\nu^s(\boldsymbol{\theta}) = s\prod_k(1 + \theta_k\sigma_k^s), \text{ and} \tag{5.13}$$

$$\nu^b(\boldsymbol{\theta}) = b\prod_k(1 + \theta_k\sigma_k^b), \tag{5.14}$$

$$\tag{5.15}$$

where s and b are the constant numbers of signal and background events. Bayesian-esque

constraint terms similar to Gaussian priors for each systematic uncertainty are also introduced into the likelihood:

$$\mathcal{L}(\mu, \boldsymbol{\theta}) = \prod_i \text{Pois}(n_i|\mu\nu_i^s(\boldsymbol{\theta}) + \sum_b \mu_b\nu_i^b(\boldsymbol{\theta})) \times \prod_k \text{Gauss}(\theta_k), \tag{5.16}$$

where $\prod_i$ indicates a term for each bin in the SR and CRs, and $\prod_k$ indicates a term for each NP.

5.3.2 Fit results

The binned maximum likelihood was performed in two steps. First a CR only fit to data was performed with $\mu(W^{\pm}W^{\mp}\gamma)$ fixed to 1 in order to constrain the background normalizations and other NPs. Then a second fit, including the SR and CRs simultaneously, was performed with the Asimov dataset in the SR defined using the background MC samples with NPs set to the values from the first fit. The fit results of the SR Asimov fit are presented in Figures 5.9 to 5.19. The meanings of each plot are:

- Figure 5.9— These are the best-fit values of the normalization factors μ, μ_b along with $\pm 1\sigma$ uncertainties.
- Figure 5.10— This is a plot of the negative log likelihood (adjusted such that the minimum is at $y = 0$) in the cases when systematic uncertainties are and are not included.
- Figure 5.11— This is the correlation matrix of the fit parameters, symmetric about the diagonal. Significant correlations between fit parameters can result in non-symmetric

uncertainties.

- Figures 5.12 to 5.18— These are plots of the NP "pulls" $(\hat{\theta} - \theta_0)/\Delta\theta$, where $\hat{\theta}$ is the best-fit value of the NP, θ_0 is the mean of its associated Gaussian constraint term in the likelihood, and $\Delta\theta$ is the uncertainty on $\hat{\theta}$. Pull distributions of NPs with Gaussian constraint terms are expected to be unit Gaussians.

- Figure 5.19— This plot shows the "impact" $\Delta\mu$ of the top 15 NPs on the best-fit value of the POI μ, along with their pulls. The impact a NP has on the POI is evaluated by re-fitting twice with the NP fixed to its central value ± its uncertainty, and then taking the difference between μ in these fits and μ in the nominal fit. The impacts are evaluated for the pre and post-fit values of the NPs and their uncertainties.

These plots provide insight into how the nuisance parameters affect the result. There are no unexpected correlations among the NPs, or with the POI. Furthermore, the pull distributions of the nuisance parameters are all nearly unit Gaussian as expected. We also see that the impacts of the NPs on the POI are symmetric as expected. The overall uncertainty on the POI is ± 0.15, so impacts of $\sim \pm 0.02$ are relatively small.

5.3.3 Fiducial cross section

The best-fit value of $\mu(W^{\pm}W^{\mp}\gamma)$, from Figure 5.9, is unsurprisingly 1.0 because the Asimov dataset is defined as the expectation from MC simulations. This implies the expected total cross section is 441 fb ± 15%, i.e. the value provided by SHERPA. However, the measured signal strength as determined by the fit is only valid in the well-understood phase space region of the $e^{\pm}\mu^{\mp}\gamma$ SR. The SR is defined in terms of criteria on reconstructed objects that

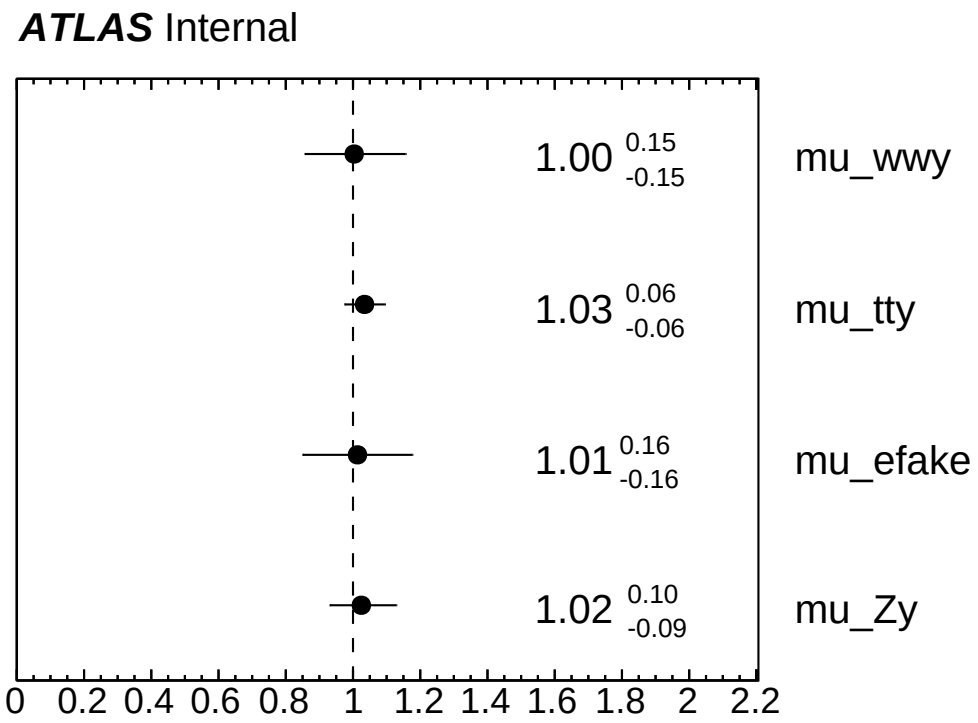

Figure 5.9: Best-fit normalization factors for $W^{\pm}W^{\mp}\gamma$, $t\bar{t}\gamma$, $Z\gamma$, $e \to \gamma$ fakes with $\pm 1\sigma$ uncertainties.

include inefficiencies and detector effects, so to report a reliable cross section measurement we correspondingly define a fiducial region. The selection criteria defining this region are similar to the $e^{\pm}\mu^{\mp}\gamma$ SR but at the level of event generation rather than reconstructed objects.

The fiducial region is defined as having an electron and a muon with opposite charge along with a photon. The photon and leptons are required to have $p_{\mathrm{T}} > 20$ GeV, the photon is required to have $|\eta| < 2.37$, and the leptons are required to have $|\eta| < 2.5$. One of the leptons is required to have $p_{\mathrm{T}} > 25$ GeV. Photons are vetoed if they are found within $\Delta R < 0.2$ of an electron or within 0.2 of a muon. Leptons are vetoed if they are found within $\Delta R < 0.1$ of a jet with $p_{\mathrm{T}} > 20$ GeV and $|\eta| < 4.5$. These criteria were applied to generator-level events with the Rivet[126] software package, and the fiducial cross section was found to be 10.5 fb. The PDF set, factorization, and renormalization scales were varied to determine the

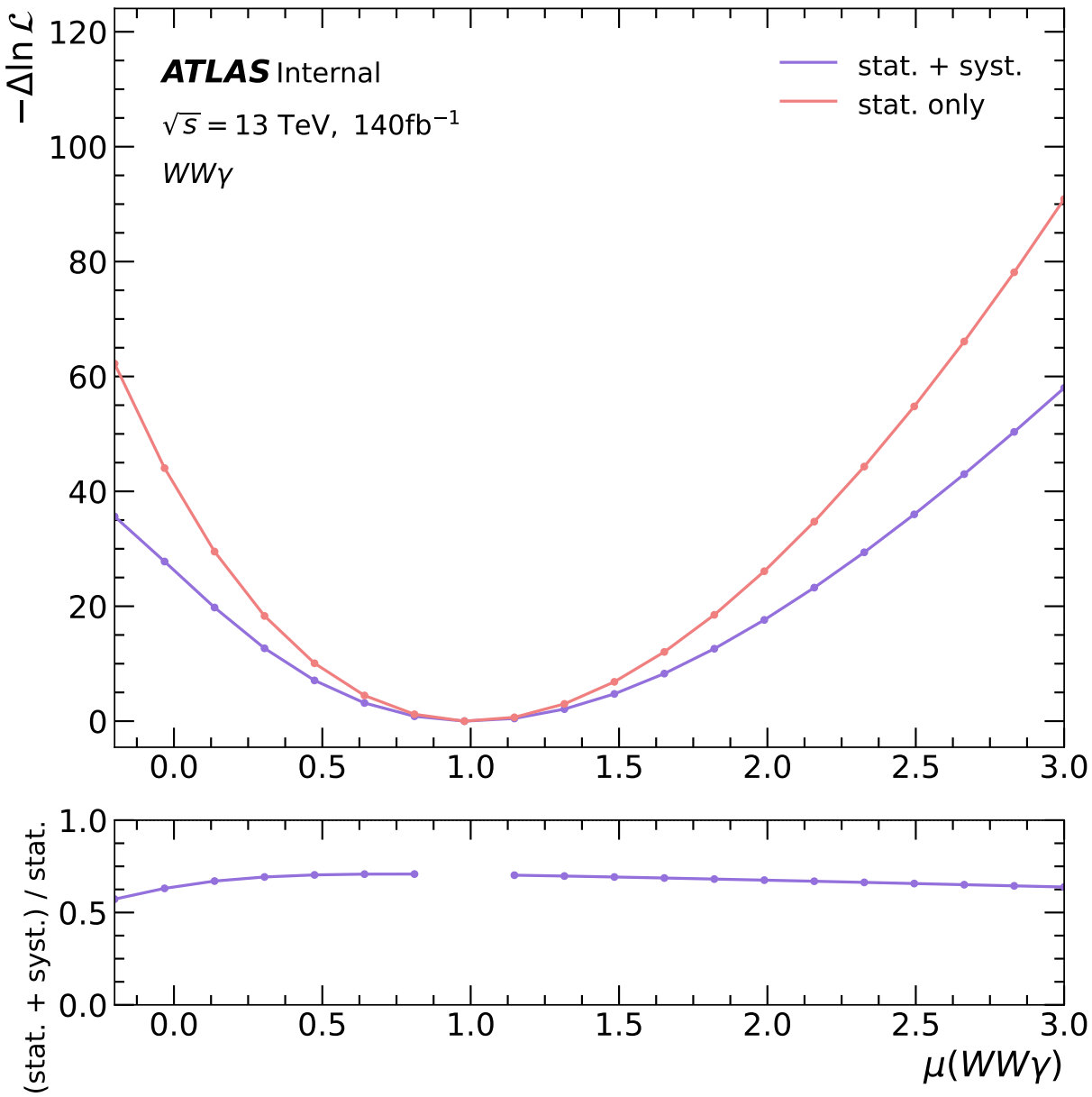

Figure 5.10: Negative log likelihood vs. $\mu(W^{\pm}W^{\mp}\gamma)$ with and without systematic uncertainties included in the fit.

envelope of systematic uncertainty on the fiducial cross section.

With this, the expected fiducial cross section is $10.5^{+17\%}_{-11\%}$ (theory) $\pm$ 15% (experiment) fb. The experimental uncertainty is dominated by statistical uncertainty.

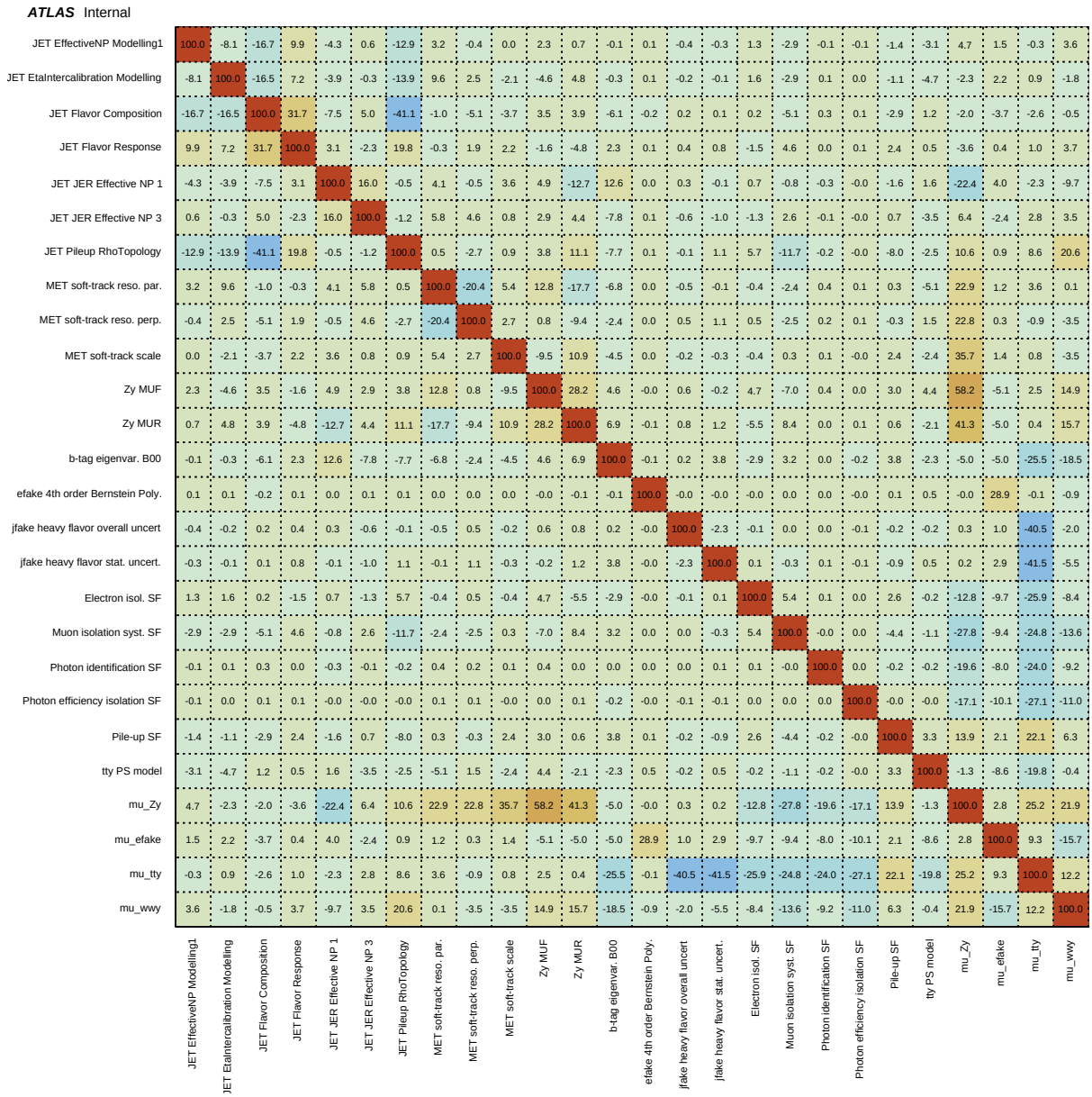

Figure 5.11: Correlations of fit parameters.

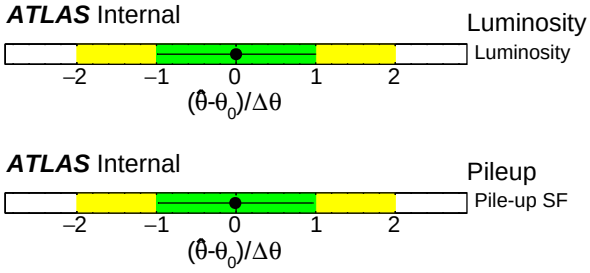

Figure 5.12: Luminosity and pile-up nuisance parameter pulls and constraints.

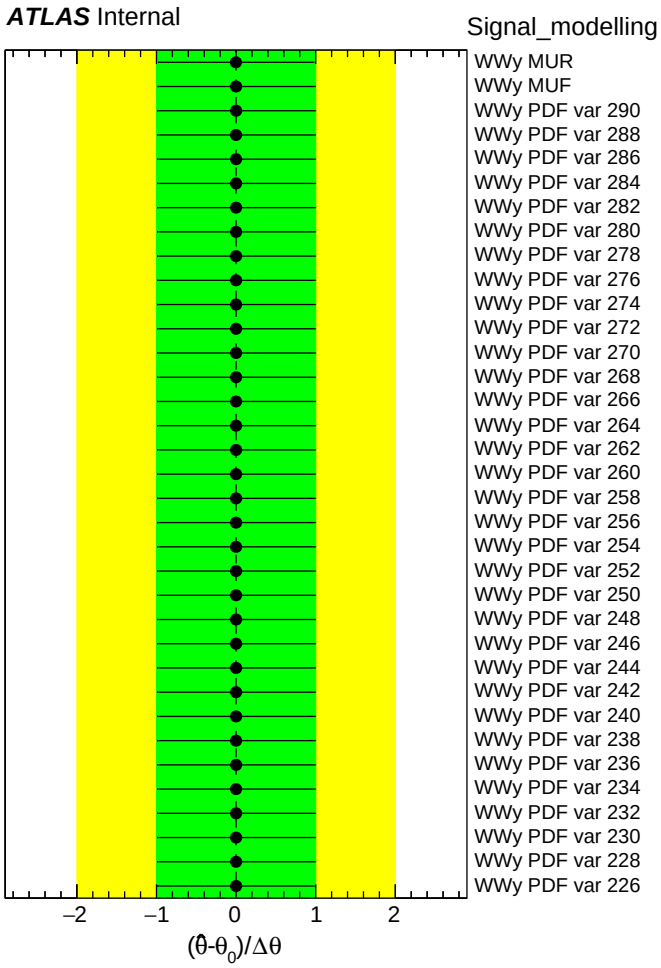

Figure 5.13: Signal modeling nuisance parameter pulls and constraints.

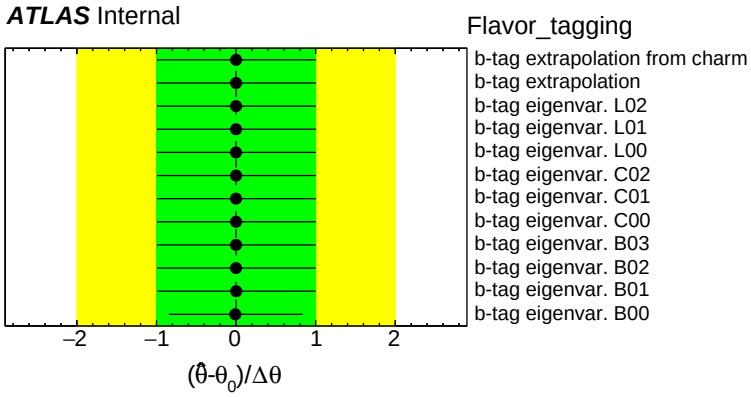

Figure 5.14: Flavor tagging nuisance parameter pulls and constraints.

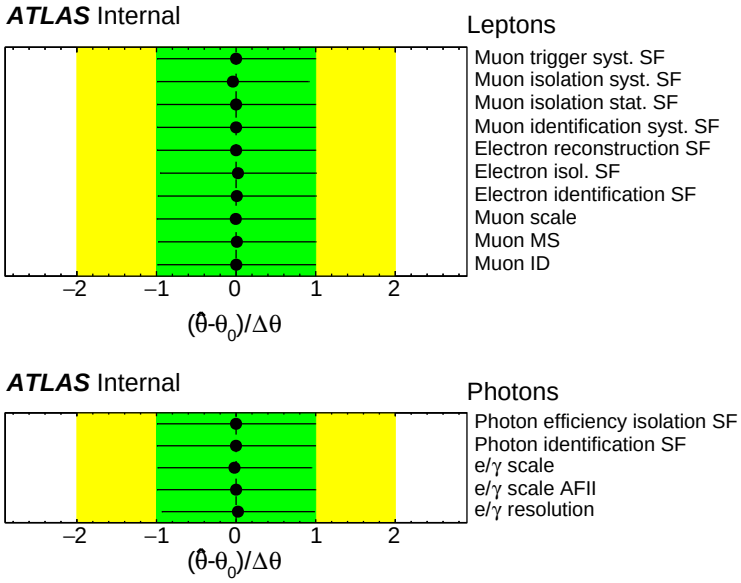

Figure 5.15: Lepton and photon nuisance parameter pulls and constraints.

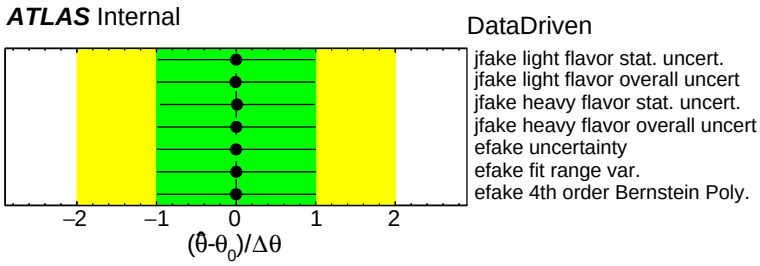

Figure 5.16: Data driven nuisance parameter pulls and constraints.

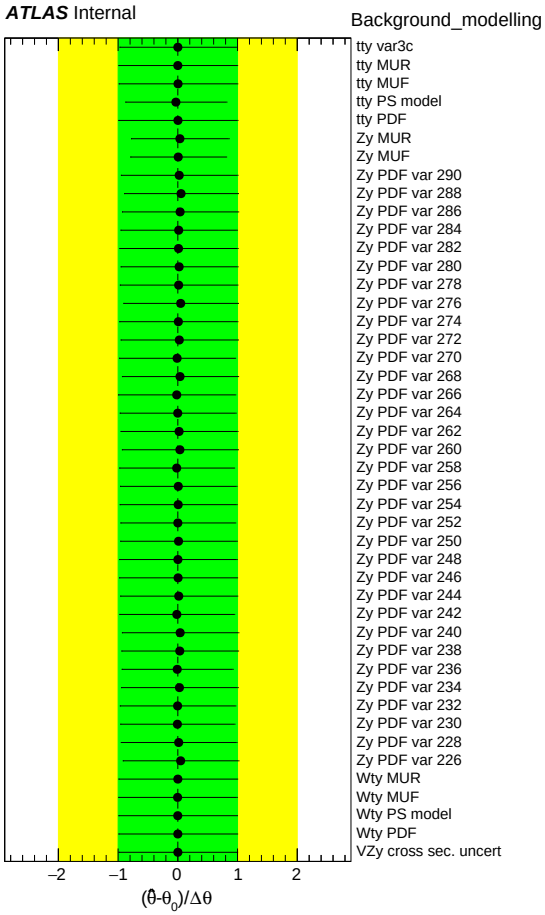

Figure 5.17: Background modeling nuisance parameter pulls and constraints.

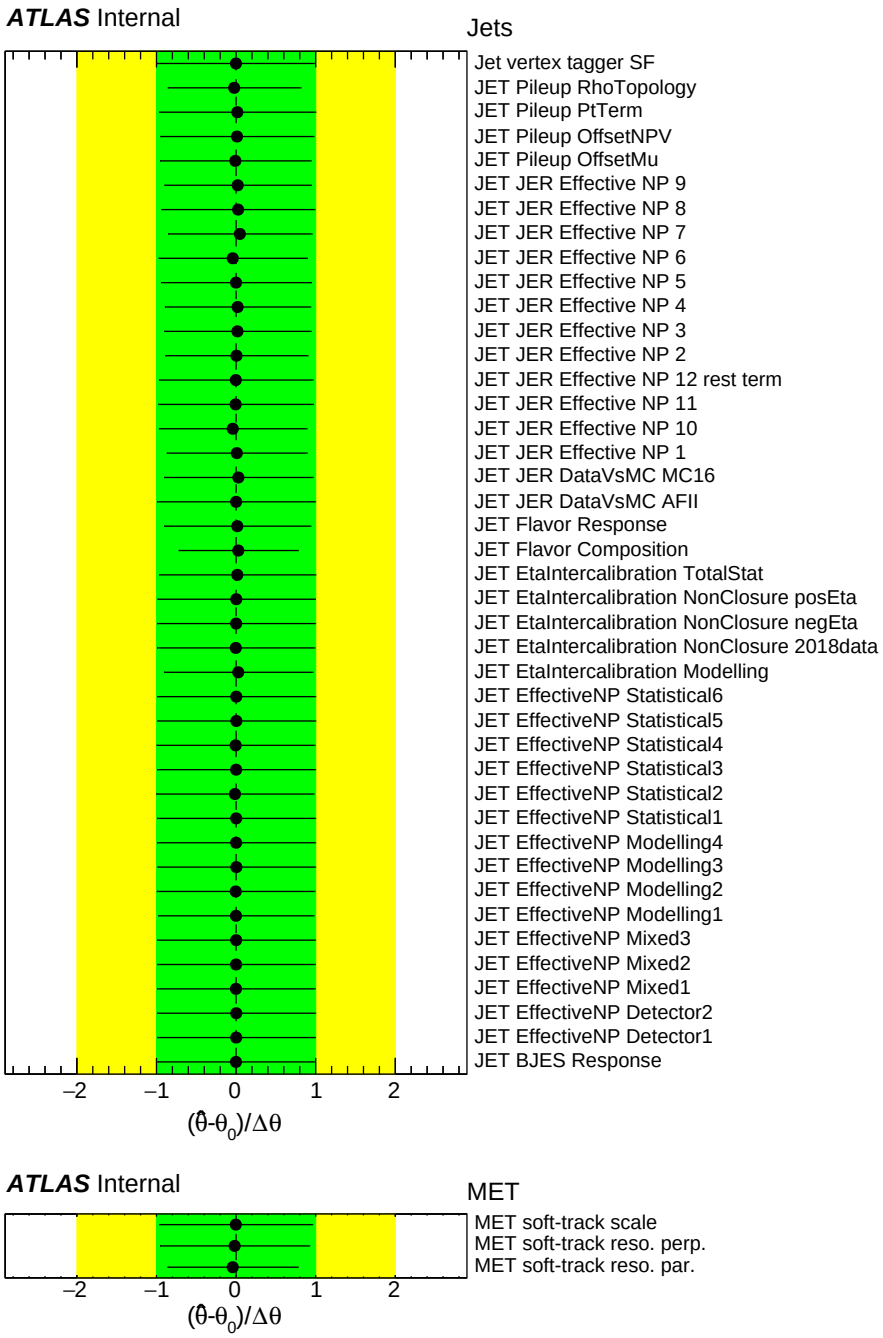

Figure 5.18: Jets and MET nuisance parameter pulls and constraints.

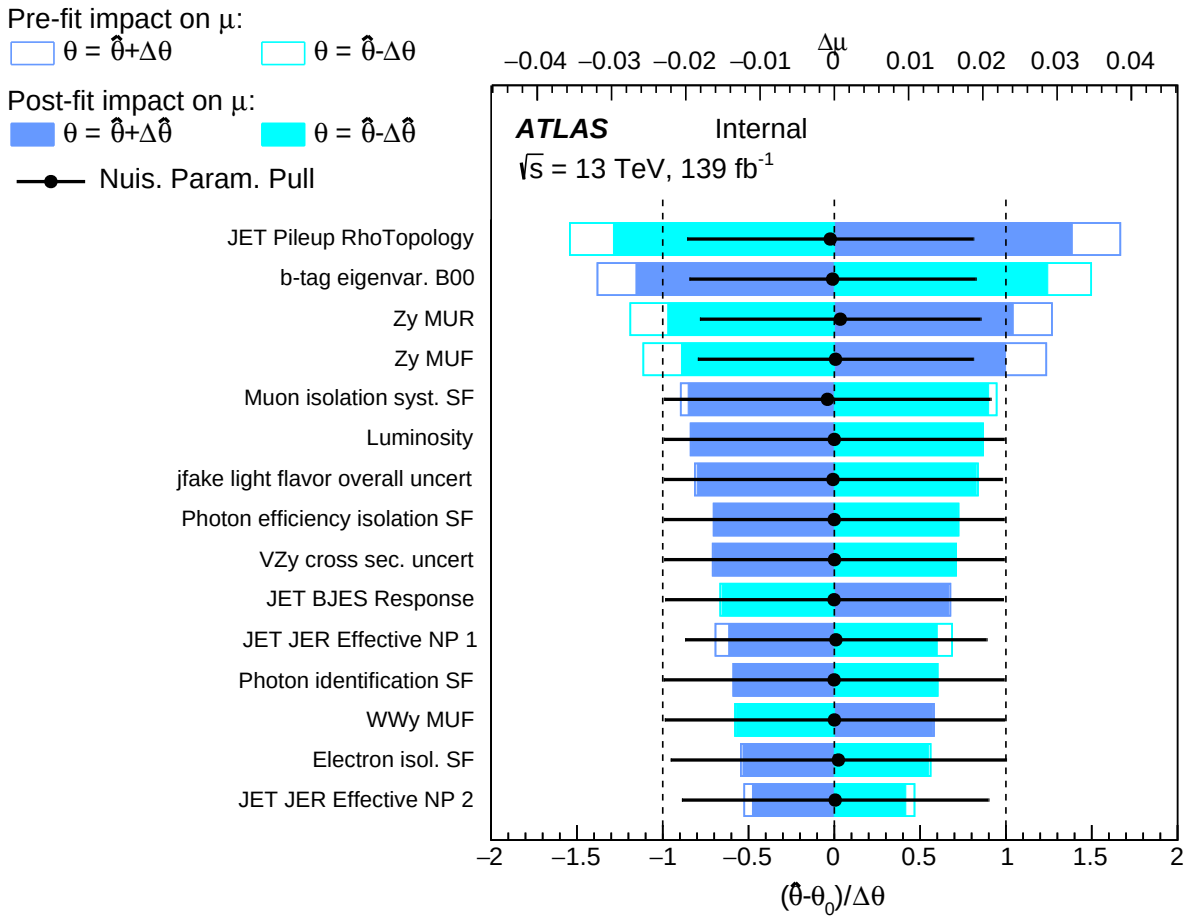

Figure 5.19: Pre-fit and post-fit impacts of nuisance parameters on the POI.

Chapter 6

$W^{\pm}W^{\mp}\gamma$ aQGC analysis

In this chapter the $W^{\pm}W^{\mp}\gamma$ cross section measurement is interpreted in the context of an EFT with dimension-8 operators, discussed in Section 2.2. The EFT model provides a useful framework for parameterizing potential deviations from the SM in LHC data.

6.1 EFT MC sample decomposition

The scattering matrix element $\mathcal{M} = \langle W^{\pm}W^{\mp}\gamma|S|pp\rangle$ for the S-matrix derived from the EFT Lagrangian (Equation (2.15)) can be decomposed into four terms

$$|\mathcal{M}|^2 = \underbrace{|\mathcal{M}_{\text{SM}}|^2}_{\text{SM}} + \underbrace{\sum_i 2c_i \text{Re}(\mathcal{M}^*_{\text{SM}}\mathcal{M}_i)}_{\text{SM-EFT interference}} + \underbrace{\sum_i c_i^2|\mathcal{M}_i|^2}_{\text{Pure EFT}} + \underbrace{\sum_i \sum_{j\neq i} 2c_i c_j \text{Re}(\mathcal{M}_i^*\mathcal{M}_j^*)}_{\text{EFT-EFT interference}}. \quad (6.1)$$

The first term represents the SM contribution, the second term (linear in c_i) represents interference between the SM and EFT, the third term (quadratic in c_i) represents contributions from pure EFT, and the fourth term represents interference between pairs of EFT operators. We neglect the EFT-EFT interference term in this analysis as it is expected to be very small compared to the other three.

Generating MC samples under the assumption of the EFT requires a specific value of the Wilson coefficient c_i for the generator to compute the matrix element. In light of Equation (6.1), however, the MC samples generated at a specific Wilson coefficient value $c_i = f$ can be re-scaled to arbitrary Wilson coefficient value f' by scaling the pure EFT part by the factor $(f'/f)^2$ and the SM-EFT interference part by the factor f'/f. Therefore, for

each EFT operator under study we generated two MC samples, representing pure EFT (called QUAD) and SM-EFT interference (called SMINT), and applied these factors to the weights of the MC events to obtain distributions at arbitrary Wilson coefficient values. Figure 6.1 shows the effect of scaling the Wilson coefficient of the M0 operator on the $p_{\mathrm{T}}(\gamma)$ distribution in the $e^{\pm}\mu^{\mp}\gamma$ region.

To correct for differences between the nominal $W^{\pm}W^{\mp}\gamma$ sample produced with Sherpa and the EFT samples produced with MadGraph, an alternate $W^{\pm}W^{\mp}\gamma$ SM sample was produced with MadGraph. The differences between the two $W^{\pm}W^{\mp}\gamma$ SM samples are plotted in Figure 6.2. The ratio of Sherpa/MadGraph, binned in $p_{\mathrm{T}}(\gamma)$, is taken as a scale factor to reweight EFT events under the assumption that differences listed in Section 4.3 would affect the EFT samples similarly to how they affect the SM samples.

6.2 EFT SR definition

The distributions of $p_{\mathrm{T}}(\gamma)$ for the 13 operators under study, decomposed into QUAD and SMINT components, are plotted in Figures 6.3 to 6.5. $p_{\mathrm{T}}(\gamma)$ is a good discriminant between EFT signal and background, so an alternate SR for the EFT analysis was defined with the same criteria as the nominal $e^{\pm}\mu^{\mp}\gamma$ SR but requiring $p_{\mathrm{T}}(\gamma) > 500$ GeV. Event yields attributed to the EFT signal and SM backgrounds in the SR are listed in Table 6.1. The remaining events with $p_{\mathrm{T}}(\gamma) < 500$ GeV define the $e^{\pm}\mu^{\mp}\gamma$ CR used to constrain the normalization of SM $W^{\pm}W^{\mp}\gamma$ in the EFT fit. BDT distributions for each EFT operator are plotted in Figures 6.6 to 6.8 in the $e^{\pm}\mu^{\mp}\gamma$ CR, Figures 6.9 to 6.11 in the $t\bar{t}\gamma$ CR, and Figures 6.12 to 6.14 in the VV CR. The contribution of EFT signal in the $Z\gamma$ CR is neglected because of the generator

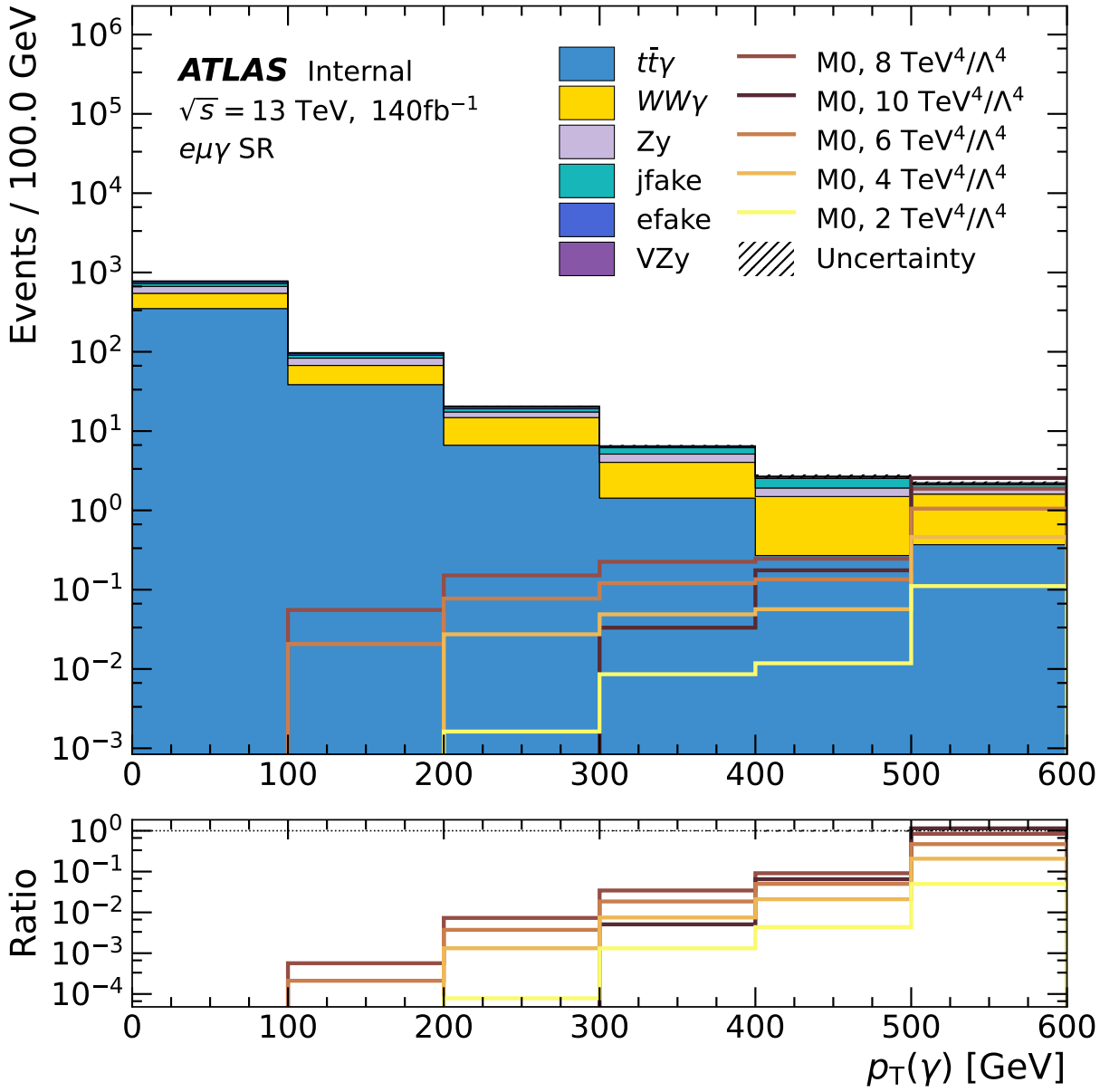

Figure 6.1: Distribution of $p_T(\gamma)$ in the $e^{\pm}\mu^{\mp}\gamma$ region with M0 Wilson coefficient set to various values. Uncertanties are statistical only. Last bin includes overflow.

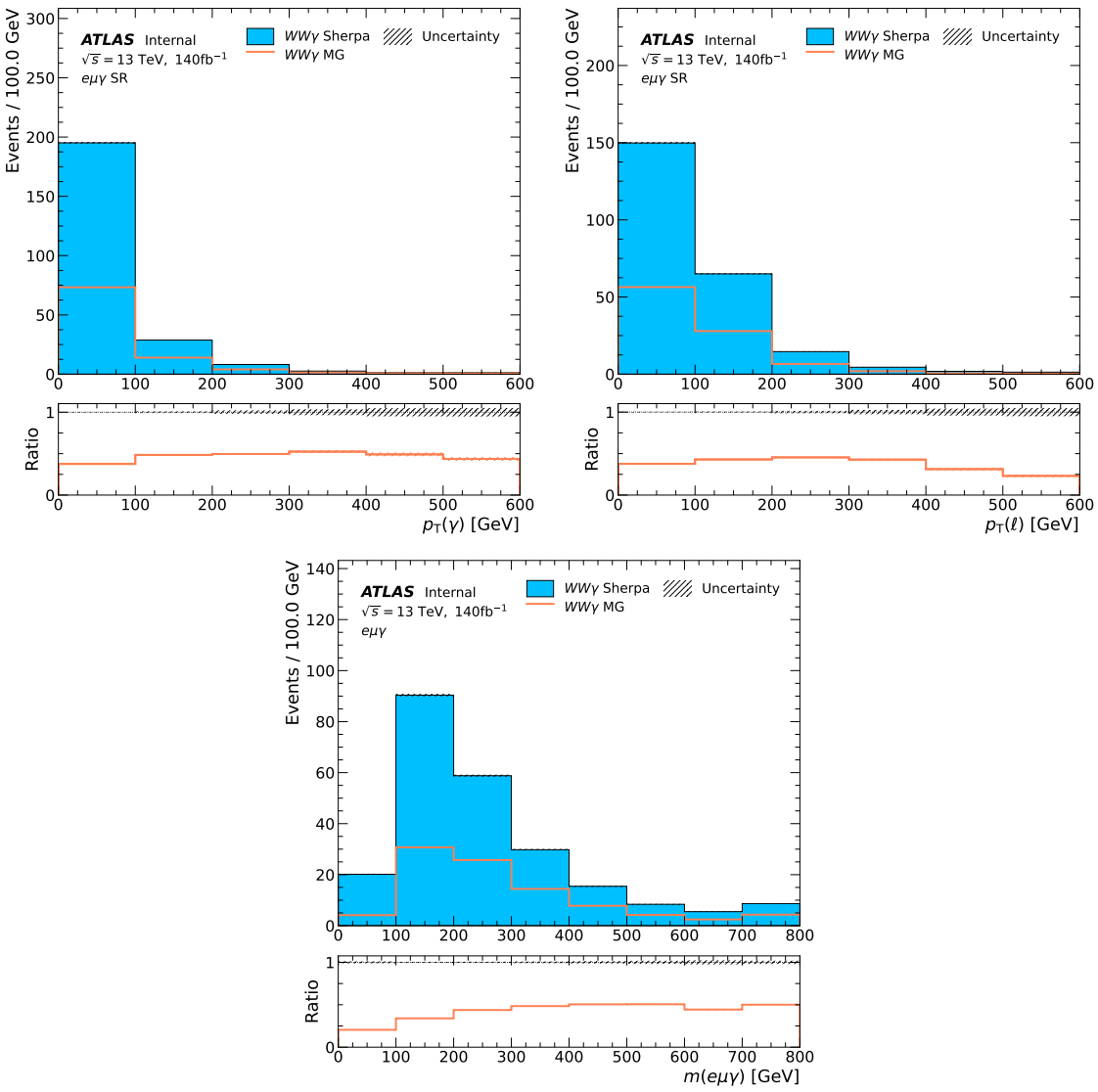

Figure 6.2: Distributions of $p_{\mathrm{T}}(\gamma)$ (upper left), $p_{\mathrm{T}}(\ell_1)$ (upper right), and $m(e,\mu,\gamma)$ (bottom) in the inclusive $e^{\pm}\mu^{\mp}\gamma$ region comparing the $W^{\pm}W^{\mp}\gamma$ SM Sherpa and MadGraph samples. Uncertanties are statistical only. Last bin includes overflow.

	EFT SR
M0	1.90
M1	1.86
M2	1.91
M3	1.89
M4	1.91
M5	1.91
M7	1.91
T0	1.89
T1	1.88
T2	1.86
T5	1.90
T6	1.90
T7	1.91
$W^{\pm}W^{\mp}\gamma$ SM	1.23
$t\bar{t}\gamma$	0.37
$j \to \gamma$	0.29
$Z\gamma$	0.24
$VZ\gamma$	0.09
$e \to \gamma$	0.01
Total bkg.	2.23

Table 6.1: EFT signal and SM background contributions to the EFT SR, when the EFT signal samples' Wilson Coefficients are set to the expected upper limit as determined in Section 6.3.

filter (see Section 4.3) requiring at least one electron at least one muon in the EFT samples at generator level, however the contribution to this CR is expected to be very small because $W^{\pm}W^{\mp}\gamma$ SM contribution is already very small.

6.3 Limits on Wilson coefficients

Upper and lower limits on the Wilson coefficients are determined by a maximum likelihood fit to the one-bin EFT SR and binned BDT distributions of the CRs. An independent fit was performed for each of the 13 Wilson coefficients. TRExFitter was used to perform the fit with the same likelihood and fit settings as described in Section 5.3 but with some key

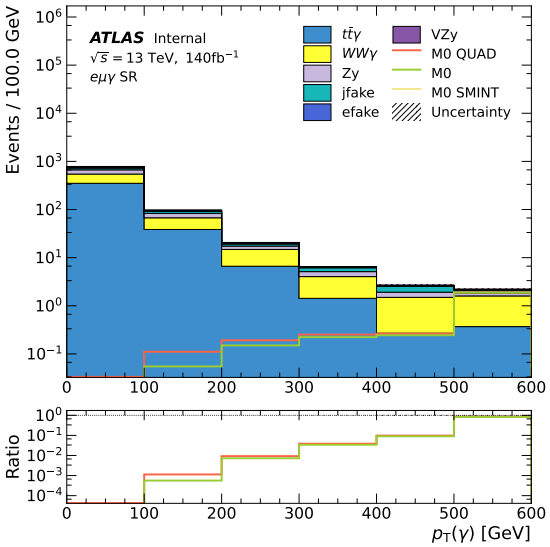

Figure 6.3: $p_{\mathrm{T}}(\gamma)$ distributions of EFT samples in the inclusive $e^{\pm}\mu^{\mp}\gamma$ region when Wilson coefficient is set to its expected upper limit as determined in Section 6.3. Each sample's QUAD and SMINT components is also shown. Uncertanties are statistical only. Last bin includes overflow.

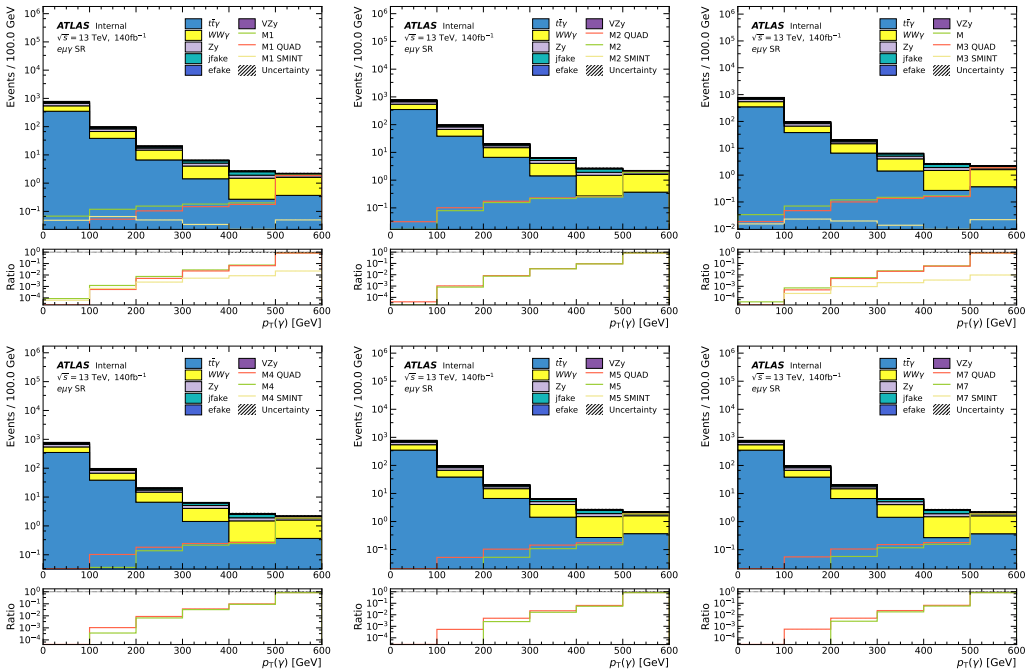

Figure 6.4: $p_{\mathrm{T}}(\gamma)$ distributions of EFT samples in the inclusive $e^{\pm}\mu^{\mp}\gamma$ region when Wilson coefficient is set to its expected upper limit as determined in Section 6.3. Each sample's QUAD and SMINT components is also shown. Uncertanties are statistical only. Last bin includes overflow.

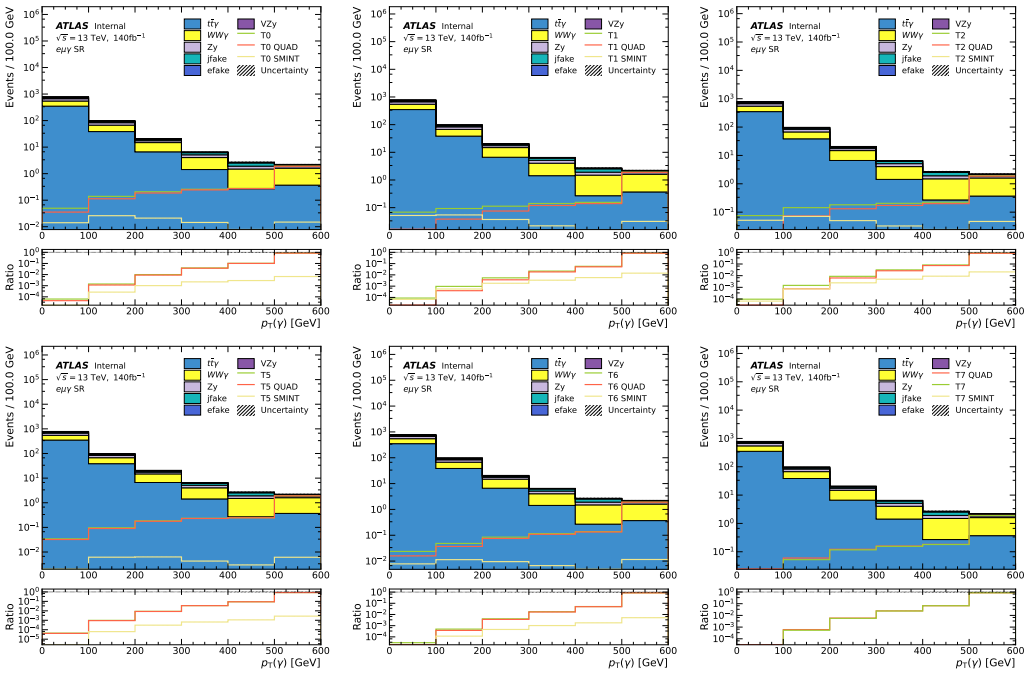

Figure 6.5: $p_{\mathrm{T}}(\gamma)$ distributions of EFT samples in the inclusive $e^{\pm}\mu^{\mp}\gamma$ region when Wilson coefficient is set to its expected upper limit as determined in Section 6.3. Each sample's QUAD and SMINT components is also shown. Uncertanties are statistical only. Last bin includes overflow.

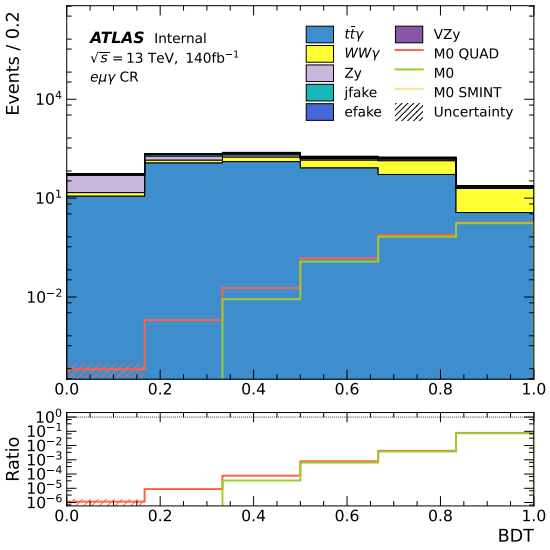

Figure 6.6: BDT distributions of EFT samples in the $e^{\pm}\mu^{\mp}\gamma$ CR when Wilson coefficient is set to its expected upper limit as determined in Section 6.3. Each sample's QUAD and SMINT components is also shown. Uncertanties are statistical only. Last bin includes overflow.

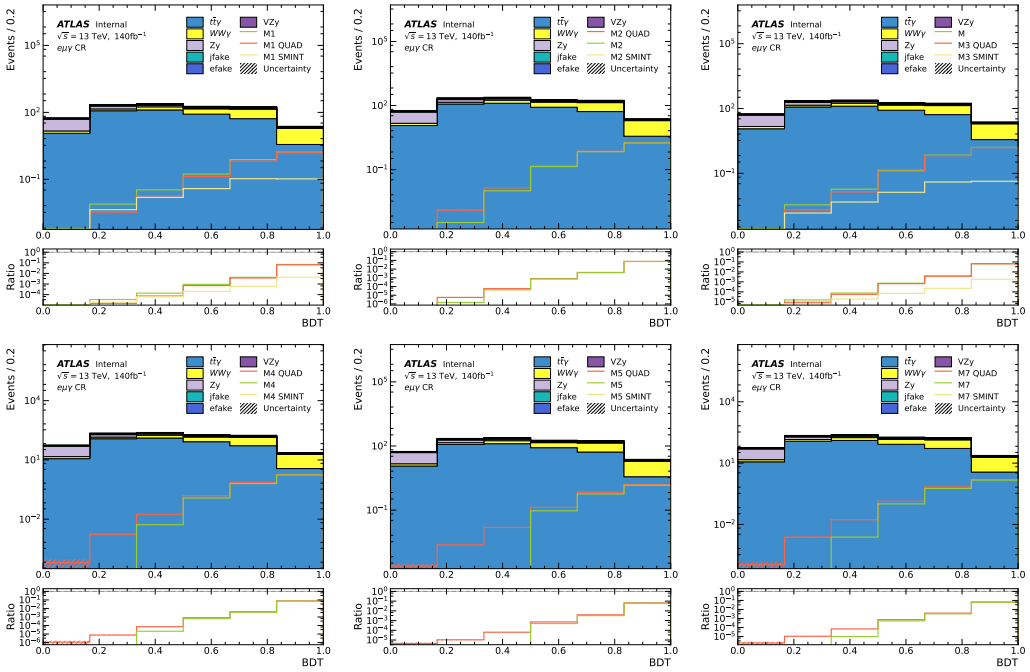

Figure 6.7: BDT distributions of EFT samples in the $e^{\pm}\mu^{\mp}\gamma$ CR when Wilson coefficient is set to its expected upper limit as determined in Section 6.3. Each sample's QUAD and SMINT components is also shown. Uncertanties are statistical only. Last bin includes overflow.

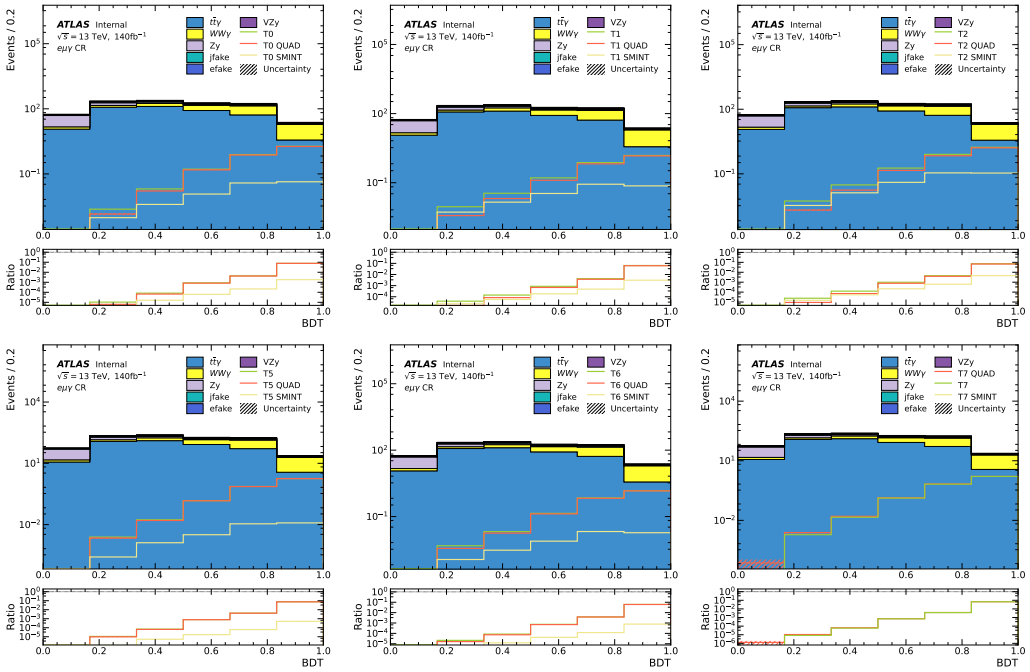

Figure 6.8: BDT distributions of EFT samples in the $e^{\pm}\mu^{\mp}\gamma$ CR when Wilson coefficient is set to its expected upper limit as determined in Section 6.3. Each sample's QUAD and SMINT components is also shown. Uncertanties are statistical only. Last bin includes overflow.

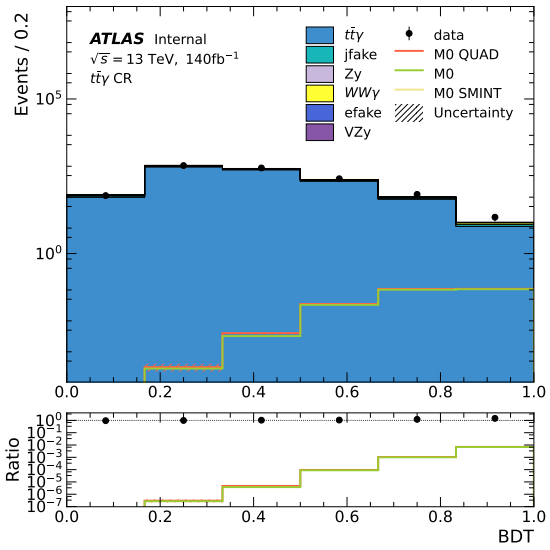

Figure 6.9: BDT distributions of EFT samples in the $t\bar{t}\gamma$ CR when Wilson coefficient is set to its expected upper limit as determined in Section 6.3. Each sample's QUAD and SMINT components is also shown. Uncertanties are statistical only. Last bin includes overflow.

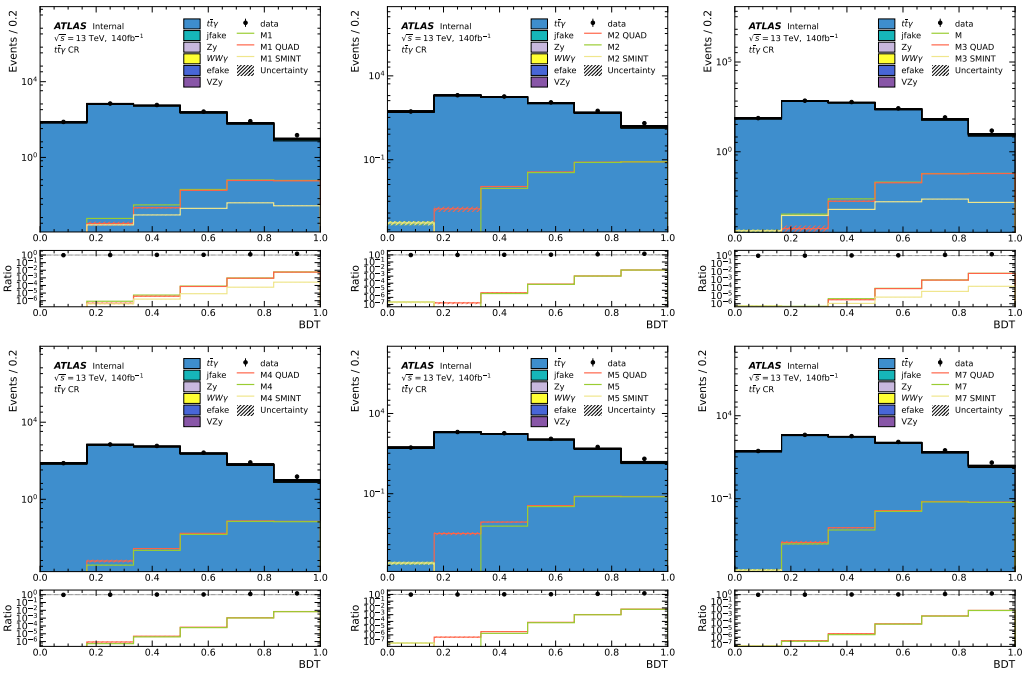

Figure 6.10: BDT distributions of EFT samples in the $t\bar{t}\gamma$ CR when Wilson coefficient is set to its expected upper limit as determined in Section 6.3. Each sample's QUAD and SMINT components is also shown. Uncertanties are statistical only. Last bin includes overflow.

differences:

1. The EFT processes are considered the signal in the EFT fits.

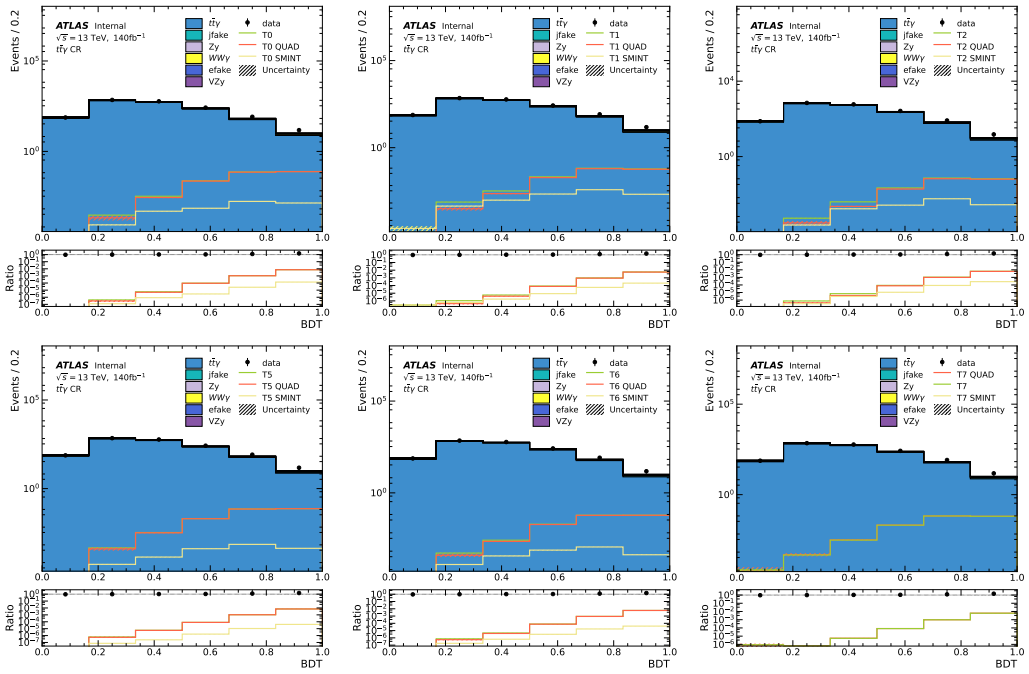

Figure 6.11: BDT distributions of EFT samples in the $t\bar{t}\gamma$ CR when Wilson coefficient is set to its expected upper limit as determined in Section 6.3. Each sample's QUAD and SMINT components is also shown. Uncertanties are statistical only. Last bin includes overflow.

2. The SM $W^{\pm}W^{\mp}\gamma$ process, considered signal in the cross section measurement, is considered background in the EFT fit.

3. The SM $W^{\pm}W^{\mp}\gamma$ normalization factor is considered a nuisance parameter.

4. A new unconstrained parameter representing the Wilson coefficient is defined as the POI.

5. The Asimov dataset is defined as the SM background expectation with NP values set to the results of the CR only fit of Section 5.3.

The normalization factor of the SMINT component of the signal is defined to depend linearly on the POI, and the normalization factor of the QUAD component is defined to depend quadratically on the POI. The EFT MC samples were generated with Wilson coefficient = 1

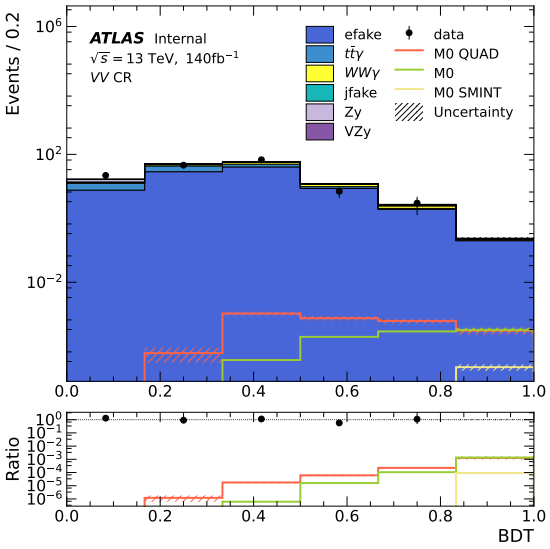

Figure 6.12: BDT distributions of EFT samples in the VV CR when Wilson coefficient is set to its expected upper limit as determined in Section 6.3. Each sample's QUAD and SMINT components is also shown. Uncertanties are statistical only. Last bin includes overflow.

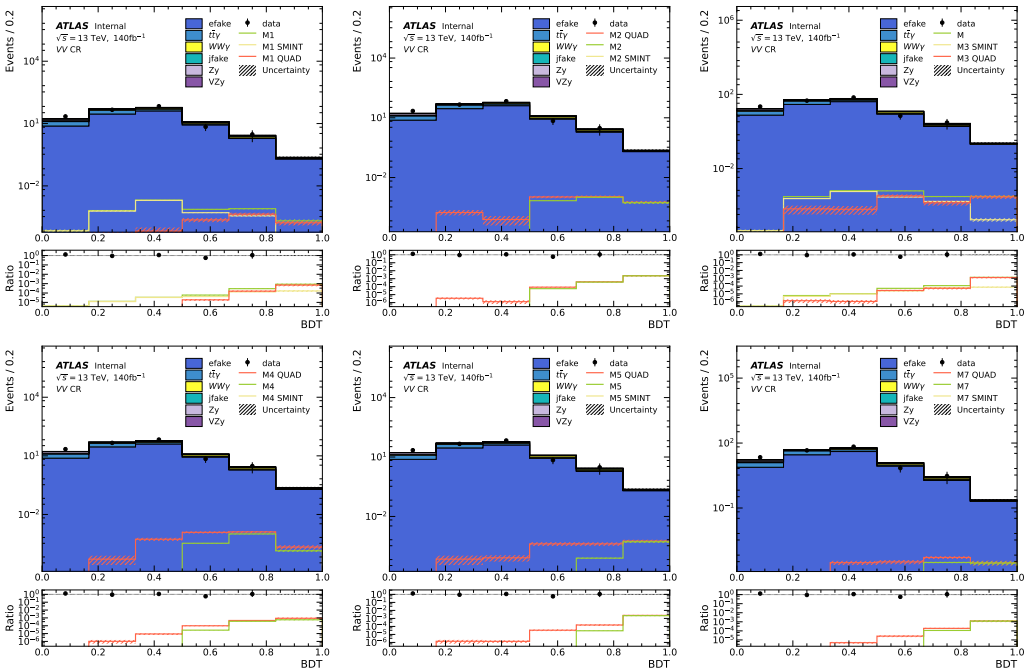

Figure 6.13: BDT distributions of EFT samples in the VV CR when Wilson coefficient is set to its expected upper limit as determined in Section 6.3. Each sample's QUAD and SMINT components is also shown. Uncertanties are statistical only. Last bin includes overflow.

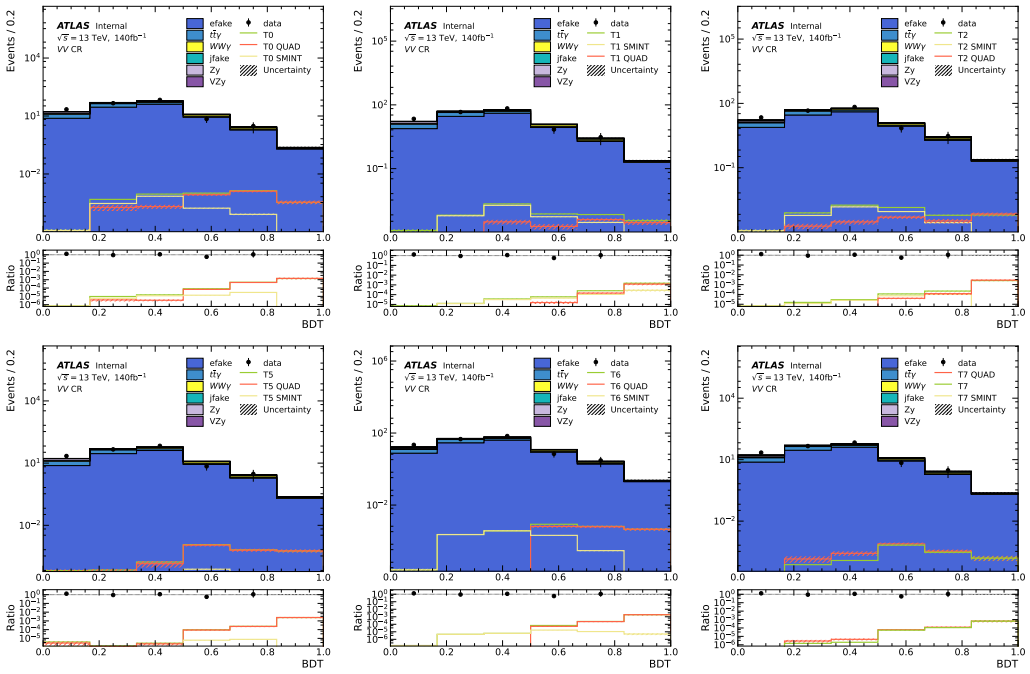

Figure 6.14: BDT distributions of EFT samples in the VV CR when Wilson coefficient is set to its expected upper limit as determined in Section 6.3. Each sample's QUAD and SMINT components is also shown. Uncertanties are statistical only. Last bin includes overflow.

TeV^4/Λ^4, so with this prescription the POI is essentially the Wilson coefficent itself in units of TeV^4/Λ^4. The fit results are presented for the M0 operator in Figures 6.15 to 6.23.

The best-fit value of the Wilson coefficient, from Figure 6.15, is of course 0 because the Asimov dataset is defined as the SM expectation. The uncertainties tell us that Wilson coefficient values in the range [-5.16, 5.16] are consistent with the SM at $\pm 1\sigma$ level. The expected upper and lower limits at the 95% confidence level (CL) are computed using Wilks' theorem[127], which states that $-2\Delta \ln \mathcal{L}$ asymptotically (in the limit of many events) converges to a χ^2 distribution. A p-value of 0.05 for a χ^2 distribution with one degree of freedom corresponds to $\chi^2 = 3.84$, hence the upper and lower expected limits are extracted from the likelihood curve where it intersects $-\Delta \ln \mathcal{L} = 3.84/2$. The likelihood curves for the 13 Wilson coefficients are plotted in Figures 6.25 and 6.27 and the expected limits are listed

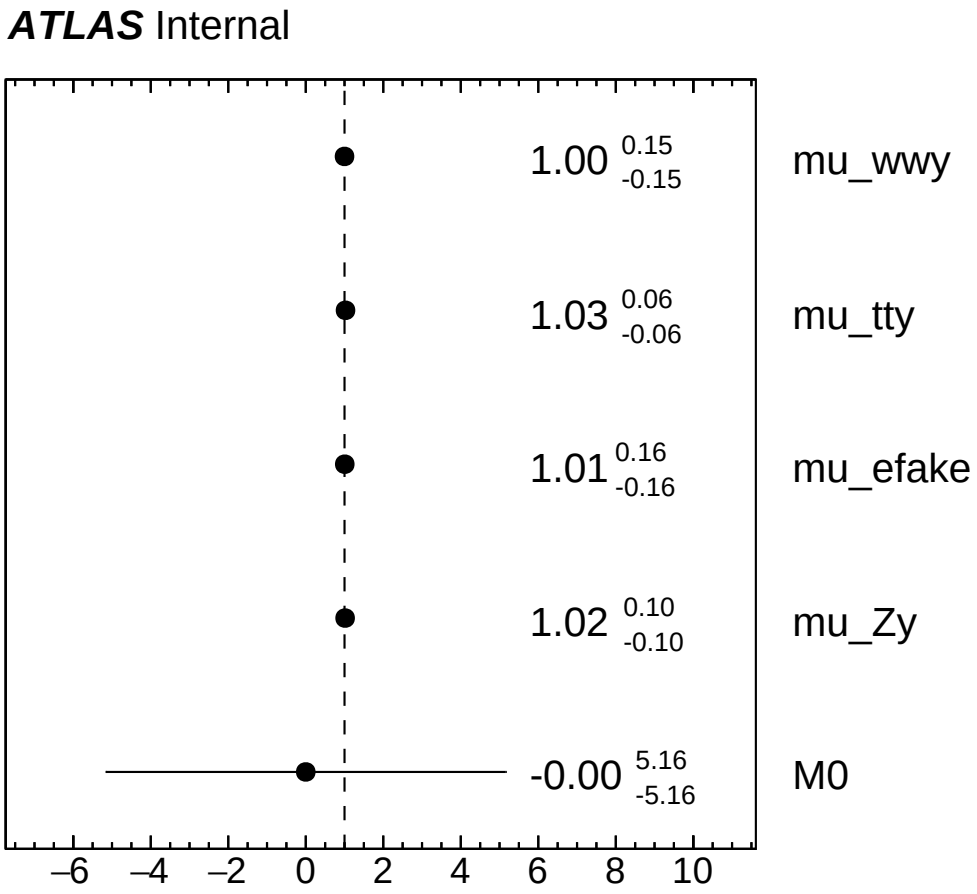

Figure 6.15: Best-fit normalization factors for the M0 Wilson coefficeint, $W^{\pm}W^{\mp}\gamma$, $t\bar{t}\gamma$, $Z\gamma$, $e \to \gamma$ fakes with $\pm 1\sigma$ uncertainties.

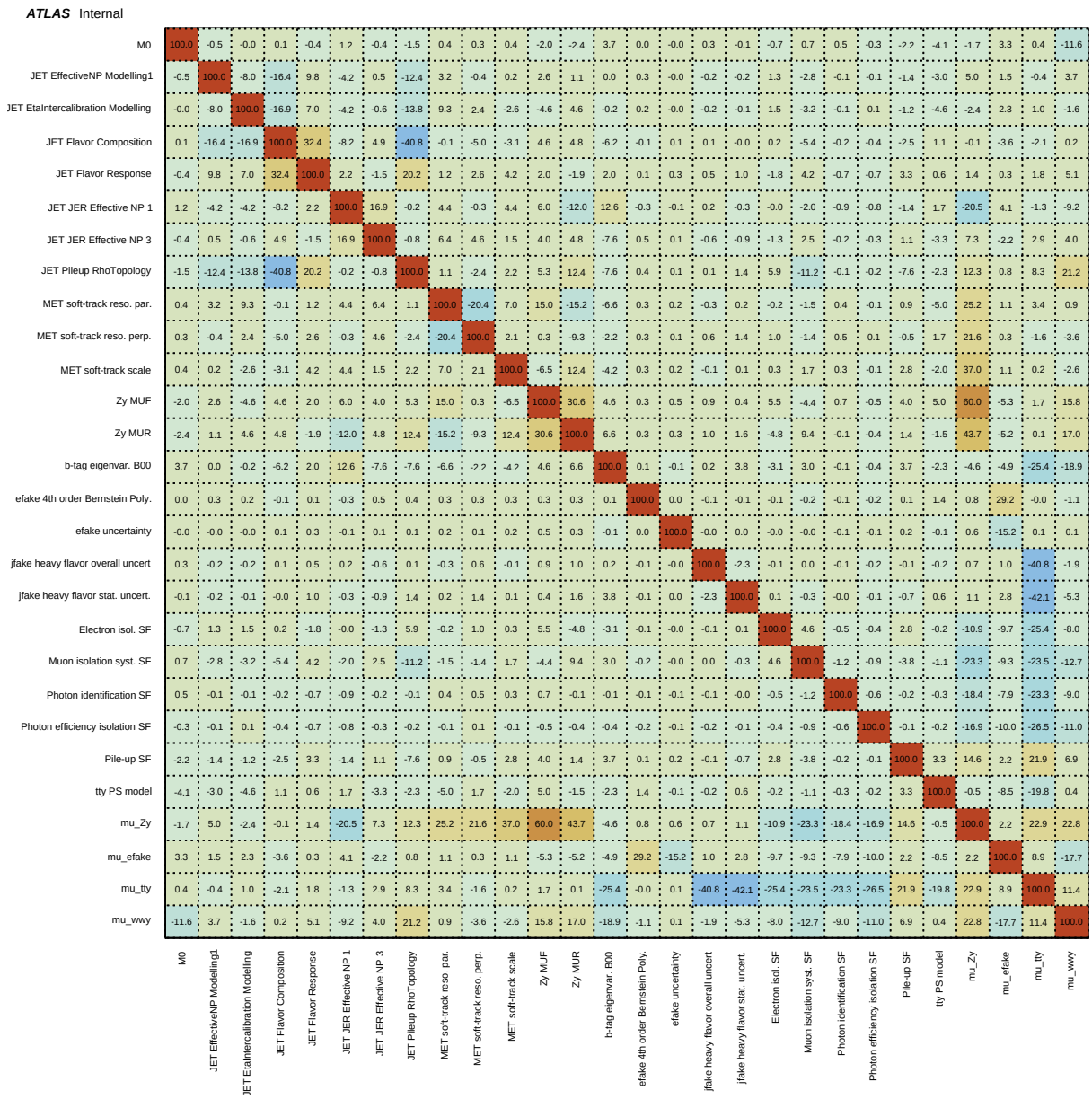

Figure 6.16: Correlations of fit parameters in the M0 EFT fit.

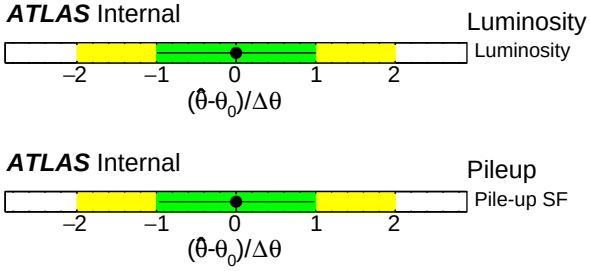

Figure 6.17: Luminosity and pile-up nuisance parameter pulls and constraints in the M0 EFT fit.

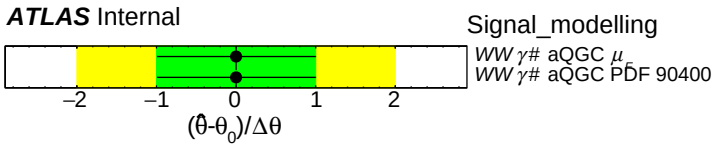

Figure 6.18: Signal modeling nuisance parameter pulls and constraints in the M0 EFT fit.

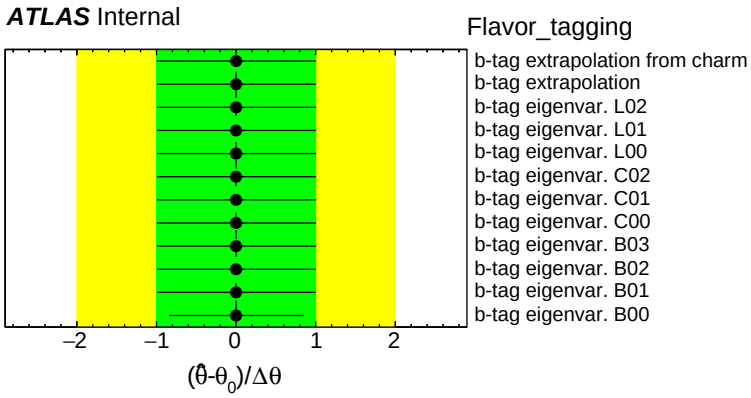

Figure 6.19: Flavor tagging nuisance parameter pulls and constraints in the M0 EFT fit.

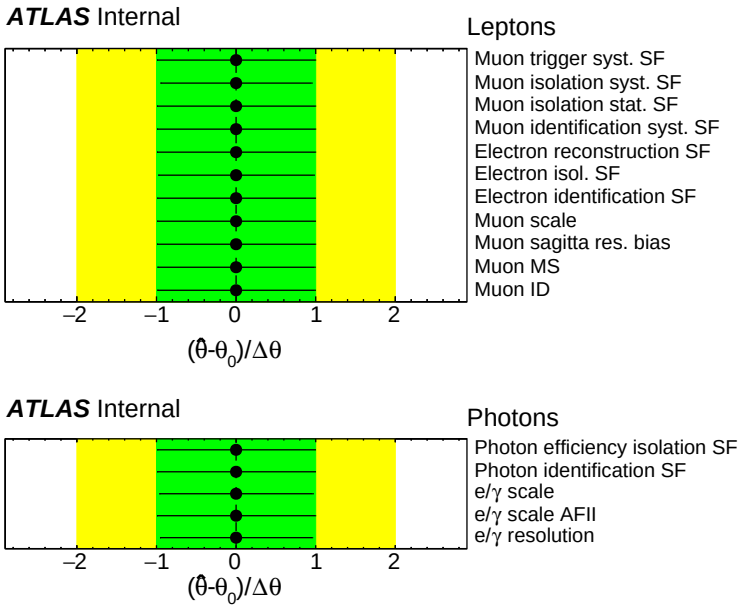

Figure 6.20: Lepton and photon nuisance parameter pulls and constraints in the M0 EFT fit.

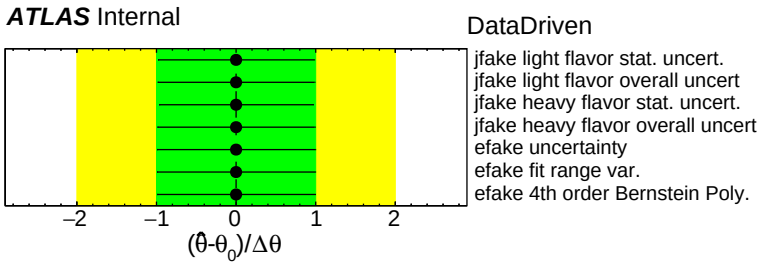

Figure 6.21: Data driven nuisance parameter pulls and constraints in the M0 EFT fit.

in Table 6.2.

	Limits @ 95% CL	Limits from ATLAS run-1[39]	Best limits to date
M0	[–7.85, 7.85]	[-300, 300]	[-0.69, 0.70] [28]
M1	[–12.83, 12.47]	[-500, 500]	[-2.0, 2.1] [28]
M2	[–3.07, 3.07]	[-1800, 1800]	[-1.9, 1.9] [32]
M3	[–4.97, 4.91]	[-3100, 3100]	[-2.7, 2.7] [32]
M4	[–7.72, 7.72]	[-1100, 1100]	[-3.7, 3.6] [32]
M5	[–6.22, 6.22]	[-1700, 1700]	[-3.9, 3.9] [32]
M7	[–25.37, 25.37]	[-1100, 1100]	[-3.4, 3.4] [28]
T0	[–1.40, 1.38]	[-100, 100]	[-0.12, 0.11] [28]
T1	[–1.68, 1.65]	[-200, 200]	[-0.12, 0.13] [28]
T2	[–3.82, 3.72]	[-400, 400]	[-0.85, 1.0] [32]
T5	[–1.09, 1.08]	[-1500, 1600]	[-0.31, 0.35] [32]
T6	[–1.31, 1.31]	[-1900, 1900]	[-0.25, 0.27] [32]
T7	[–2.92, 2.92]	[-4300, 4300]	[-0.67, 0.73] [32]

Table 6.2: Expected limits, in units of TeV^4/Λ^4, at the 95% CL of the 13 Wilson coefficients.

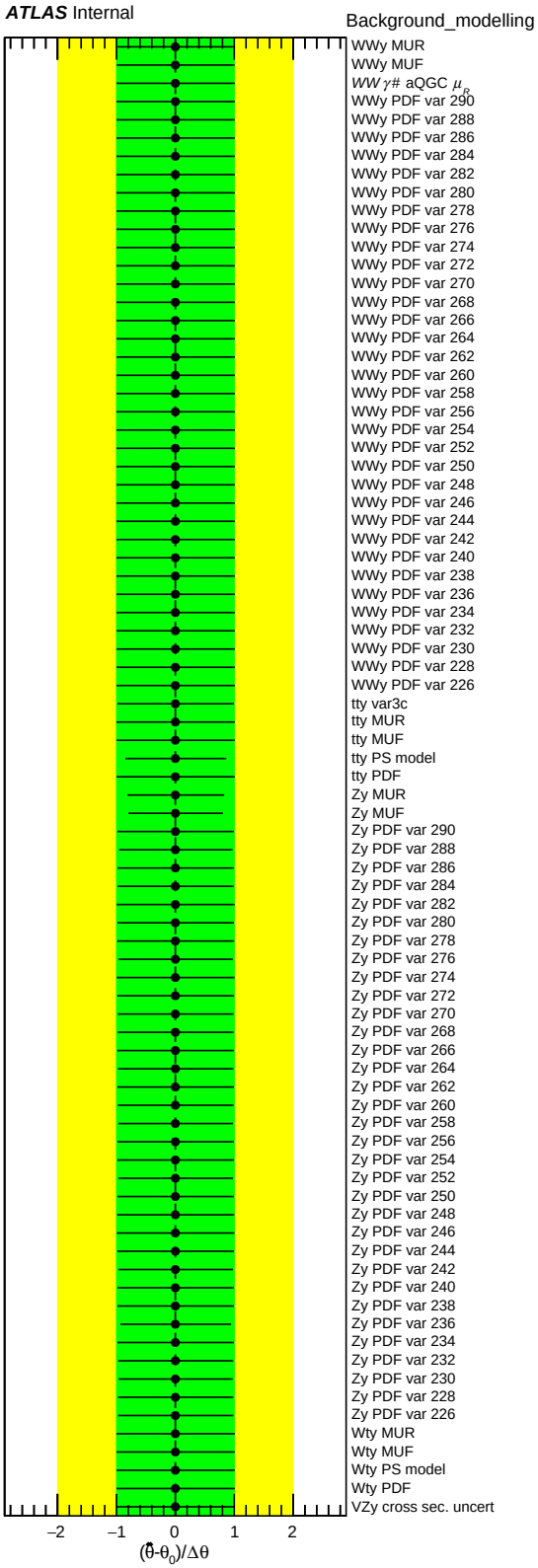

Figure 6.22: Background modeling nuisance parameter pulls and constraints in the M0 EFT fit.

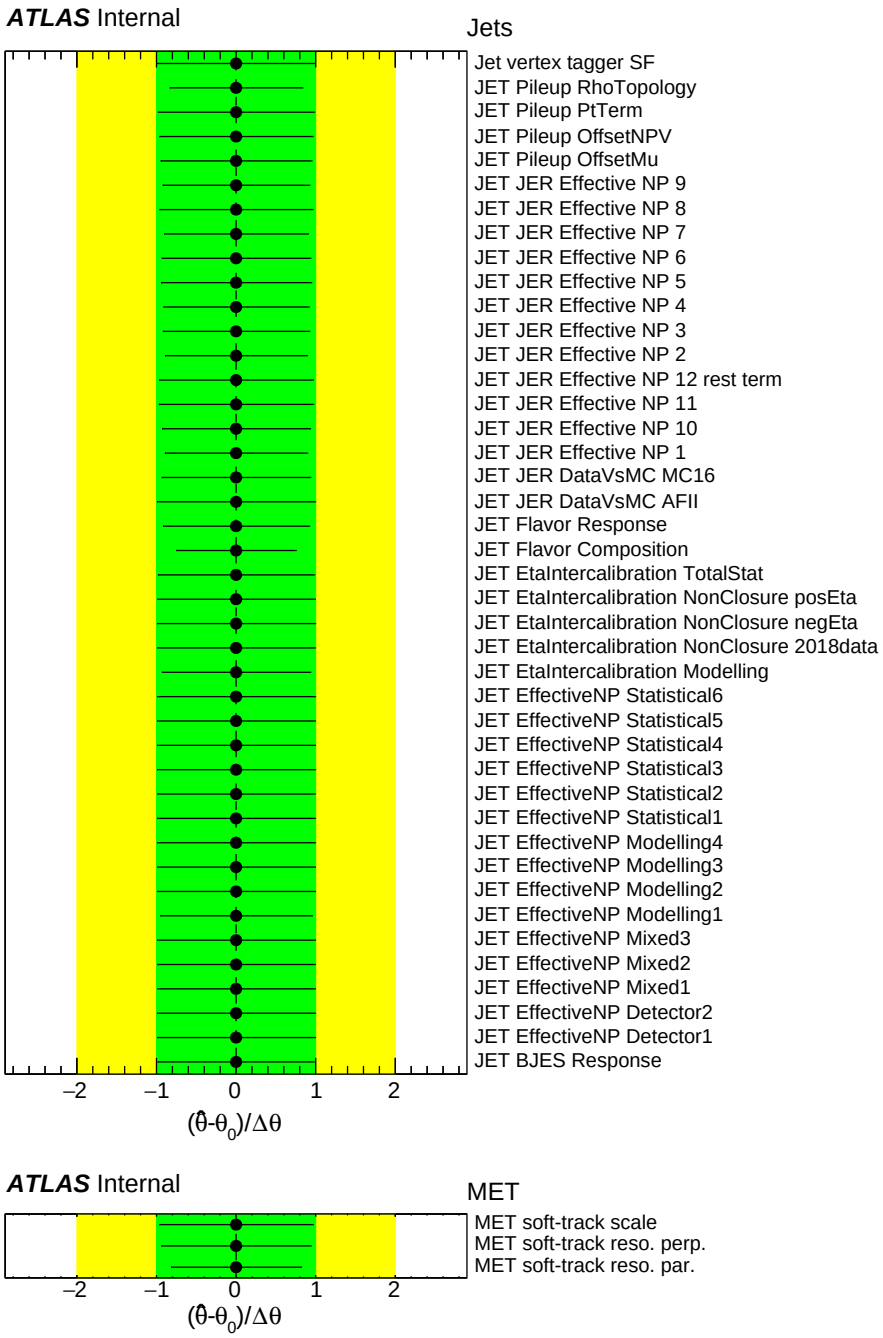

Figure 6.23: Jets and MET nuisance parameter pulls and constraints in the M0 EFT fit.

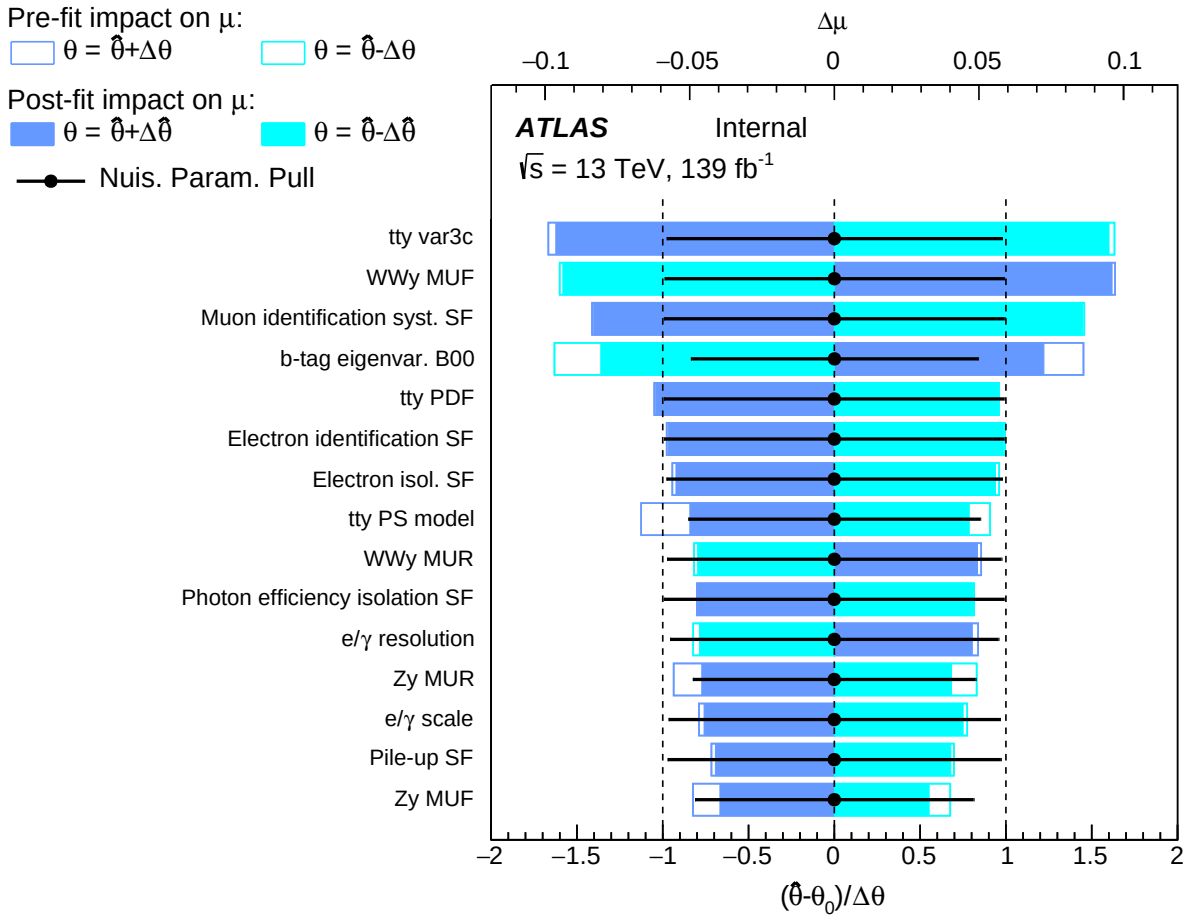

Figure 6.24: Pre-fit and post-fit impacts of nuisance parameters on the M0 Wilson coefficient (POI).

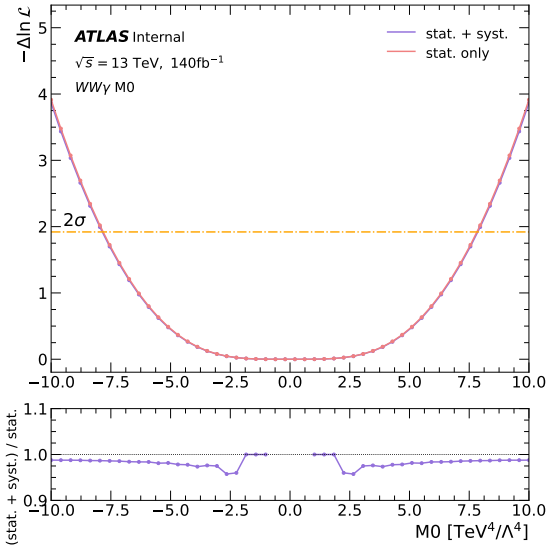

Figure 6.25: Negative log likelihood vs. Wilson coefficient (POI) with and without systematic uncertainties.

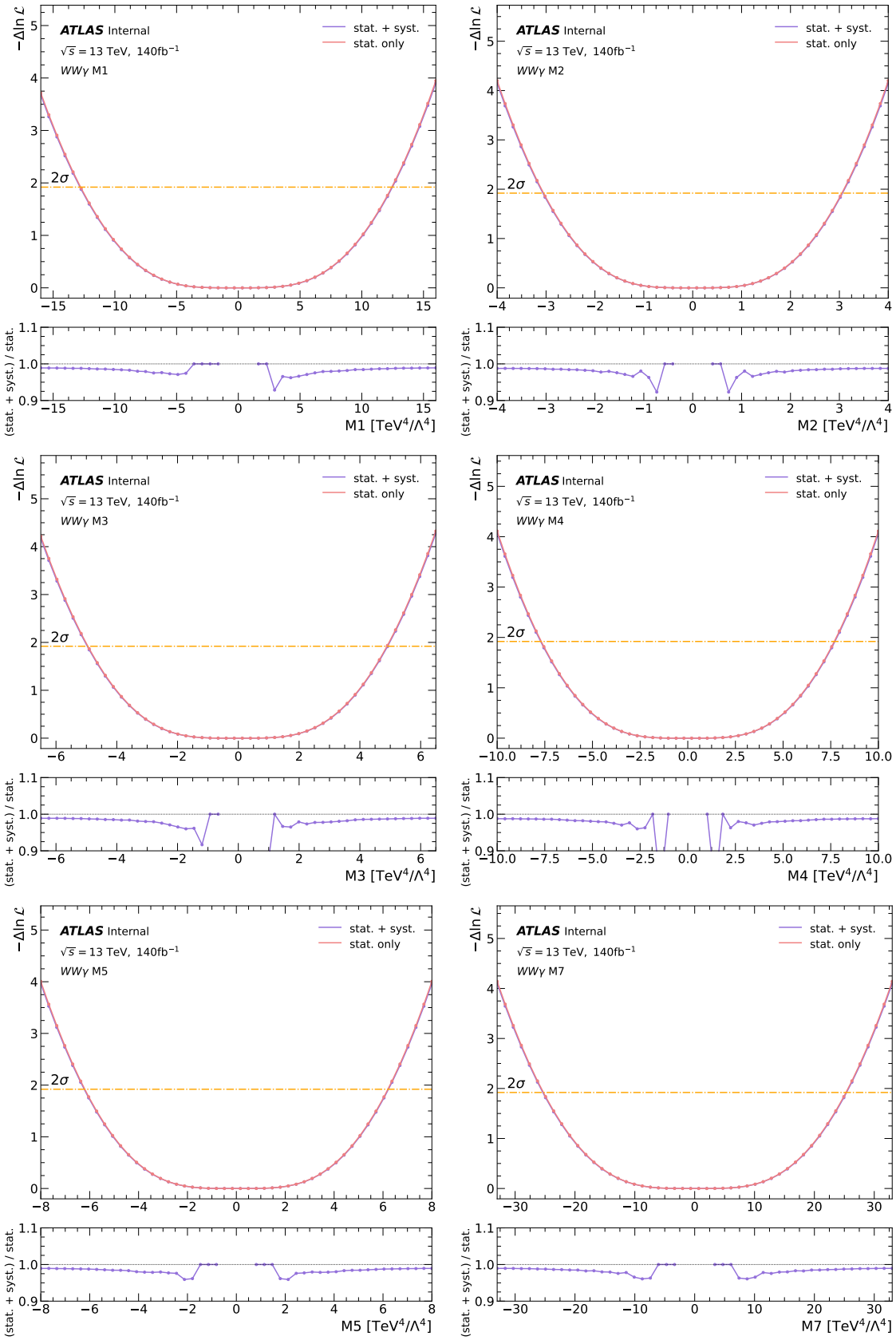

Figure 6.26: Negative log likelihood vs. Wilson coefficient (POI) with and without systematic uncertainties.

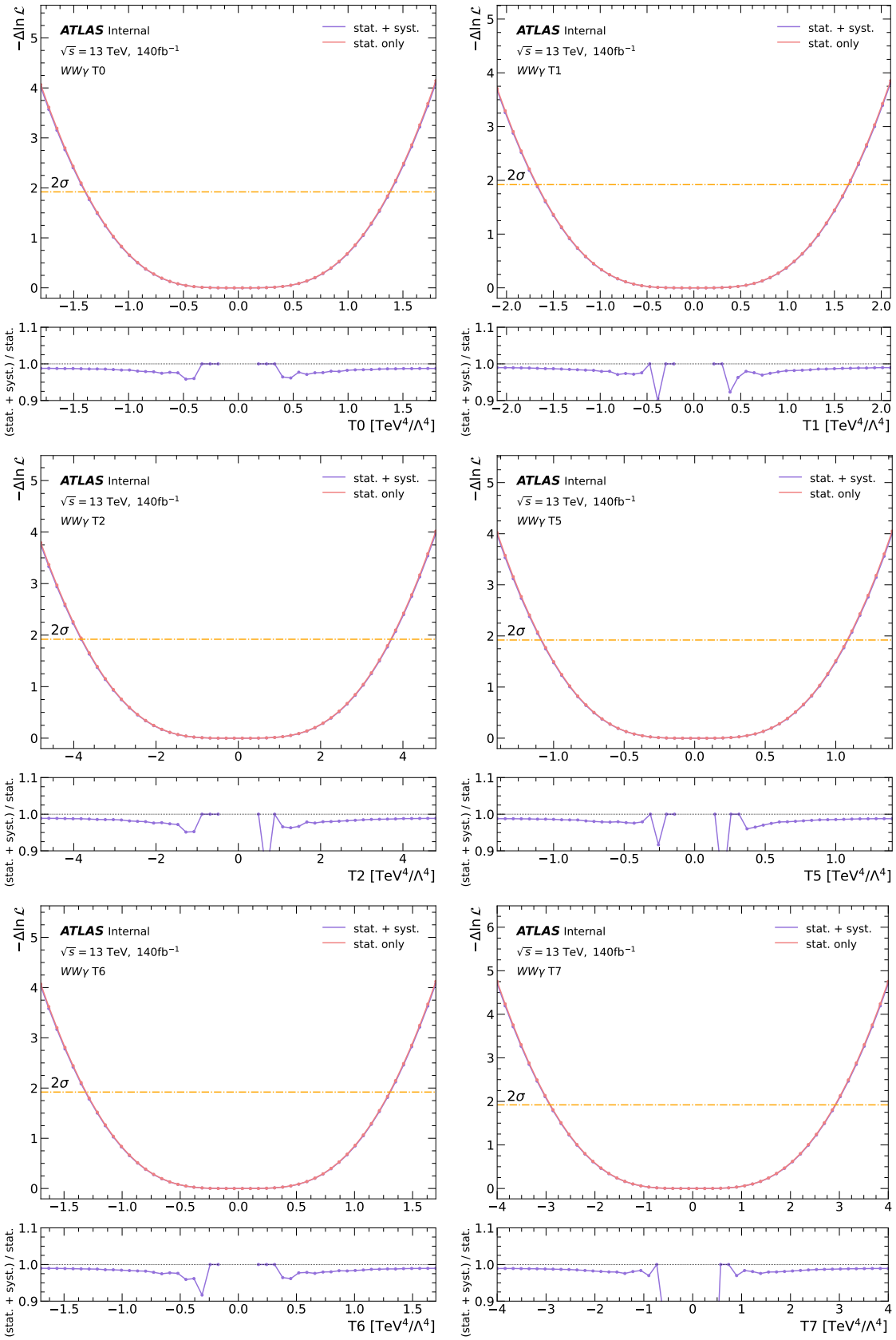

Figure 6.27: Negative log likelihood vs. Wilson coefficient (POI) with and without systematic uncertainties.

6.4 Unitarity restoration

As discussed in Section 2.2, the EFT operators are known to be non-unitary at high $\sqrt{s}$. The unitarity bounds of Table 2.1 at $\sqrt{s} = 3$ TeV where the distribution of $m(W^{\pm}W^{\mp}\gamma)$ at parton level (Figure 2.6) peaks are smaller than the expected limits of Table 6.2, indicating likely unitary violation. We implemented two model-dependent procedures to restore unitarity to the EFT model, and computed the dependence of the 95% CL limits on the model parameters.

Clipping method

The first method to restore unitarity to the MC samples is simply to veto events with parton-level $m(W^{\pm}W^{\mp}\gamma)$ greater than some energy threshold. The energy threshold is an arbitary model parameter, as we do not know *a priori* what values of $\sqrt{s}$ violate unitarity in nature. The upper and lower expected limits at the 95% CL vs. the energy threshold are presented in Figures 6.28 to 6.30.

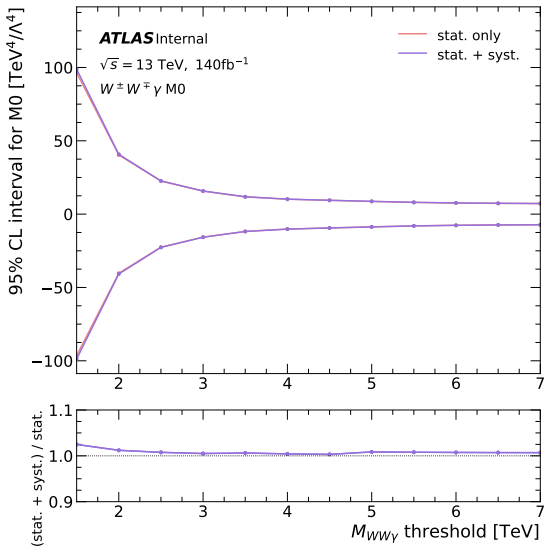

Figure 6.28: 95% CL upper and lower expected limits on Wilson coefficients vs. clipping energy.

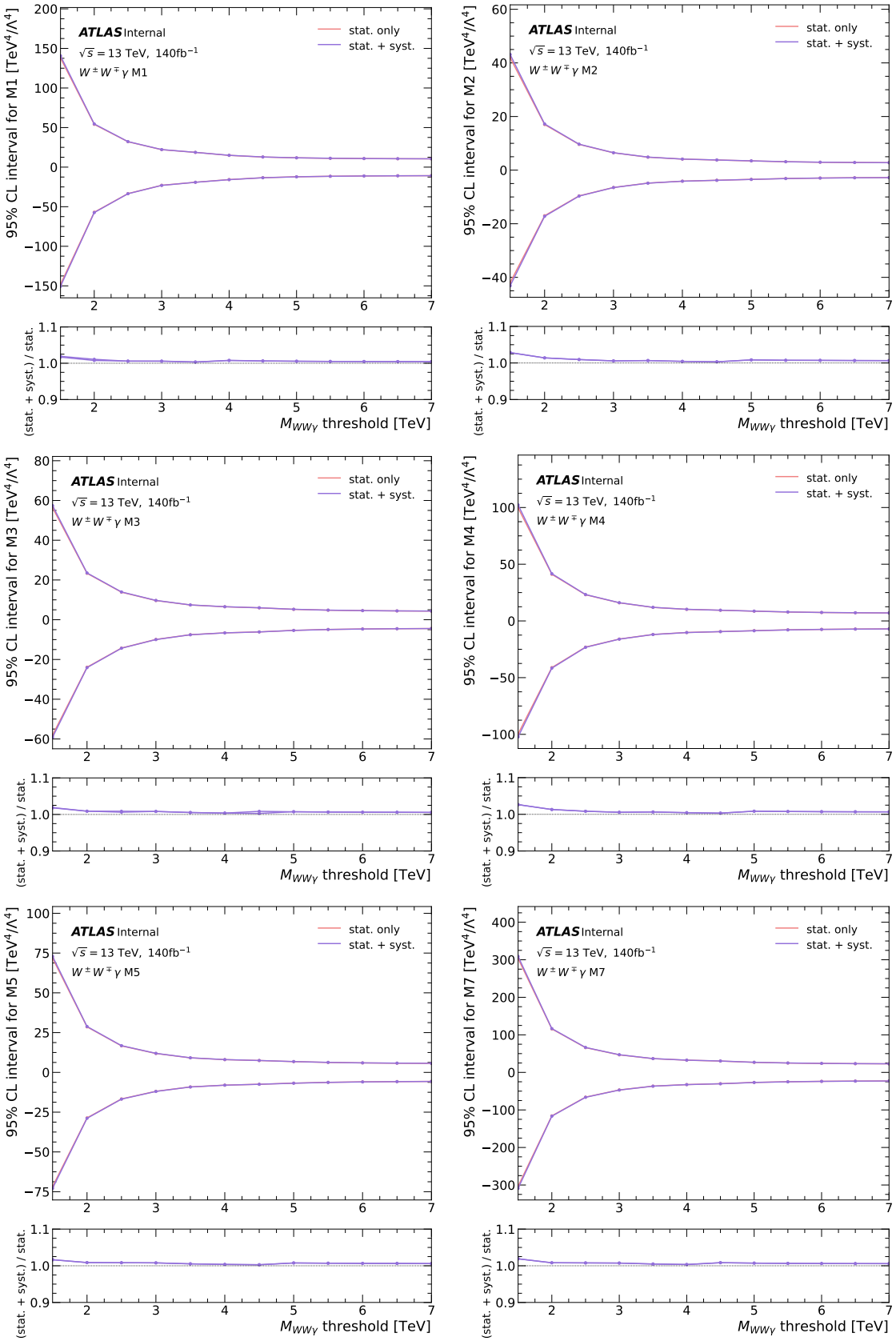

Figure 6.29: 95% CL upper and lower expected limits on Wilson coefficients vs. clipping energy.

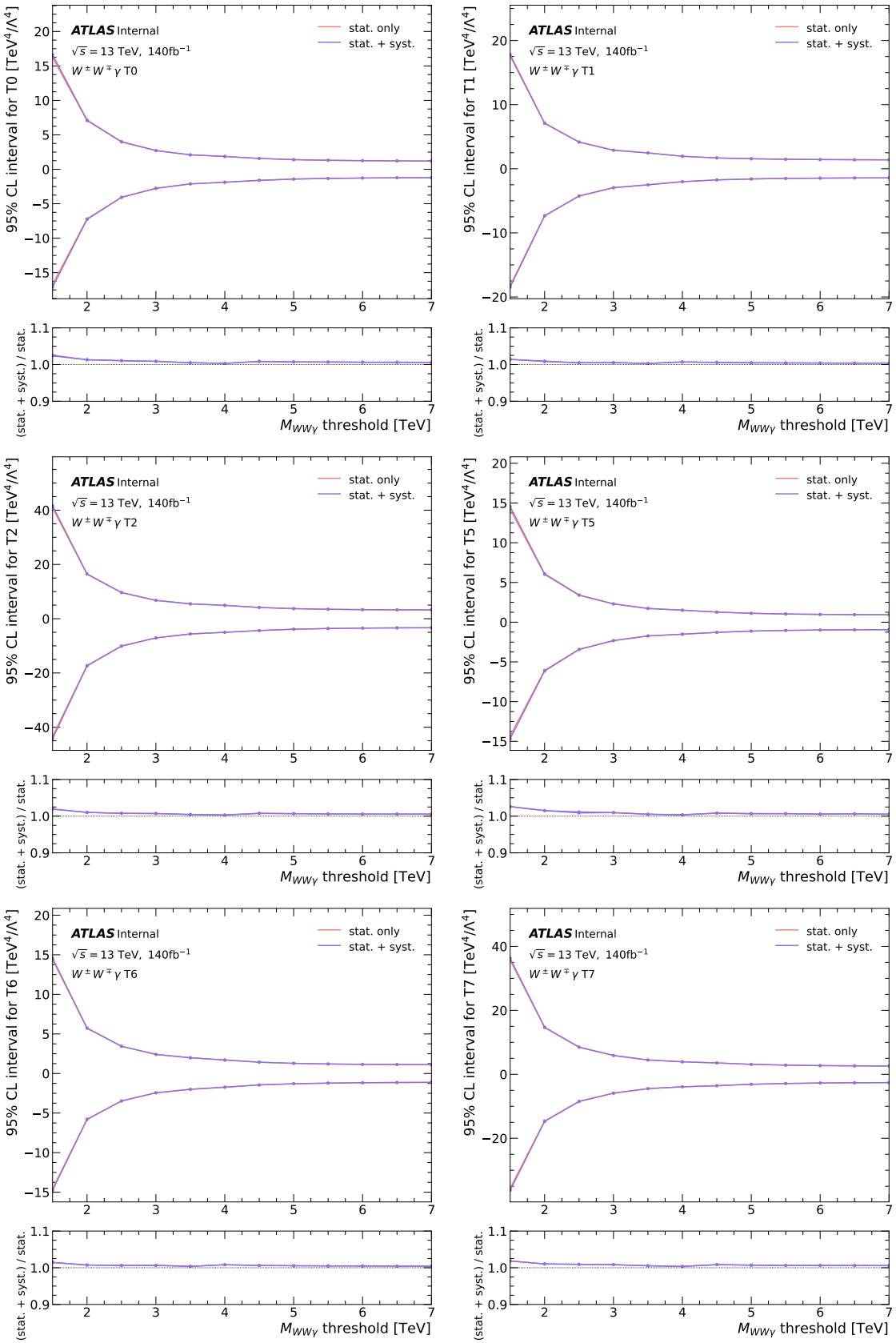

Figure 6.30: 95% CL upper and lower expected limits on Wilson coefficients vs. clipping energy.

Dipole form factor method

An alternative method of restoring unitarity is to introduce a form factor term[128] to the Wilson coefficient:

$$c_i \to \frac{c_i}{\left(1 + \frac{\sqrt{s}^2}{\Lambda_{\mathrm{FF}}^2}\right)^n}, \tag{6.2}$$

where Λ_{FF} and n are arbitrary model parameters. It is conventional to choose $n = 2$ for a dipole form factor, but Λ_{FF} remains an arbitary parameter. The form factor is implemented by re-weighting EFT events with the dipole form factor as a coefficeint, with parton-level $m(W^{\pm}W^{\mp}\gamma)$ representing $\sqrt{s}$. Figures 6.31 to 6.33 presents the Λ_{FF} dependence of the expected 95% CL upper and lower limits.

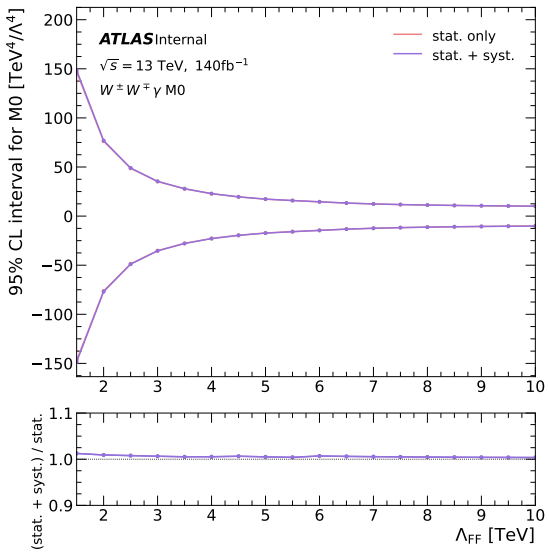

Figure 6.31: 95% CL upper and lower expected limits on Wilson coefficients vs. Λ_{FF}.

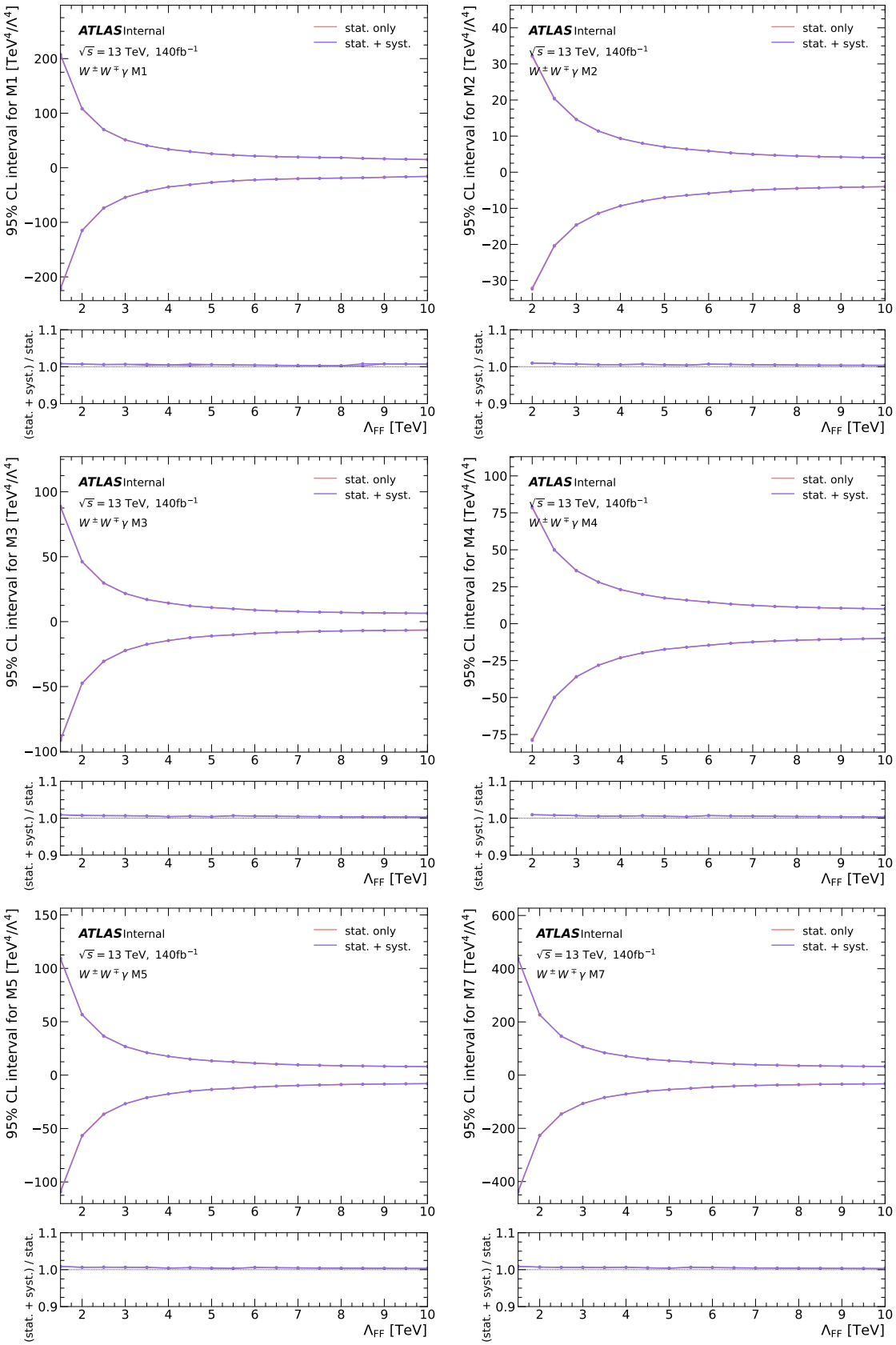

Figure 6.32: 95% CL upper and lower expected limits on Wilson coefficients vs. Λ_{FF}.

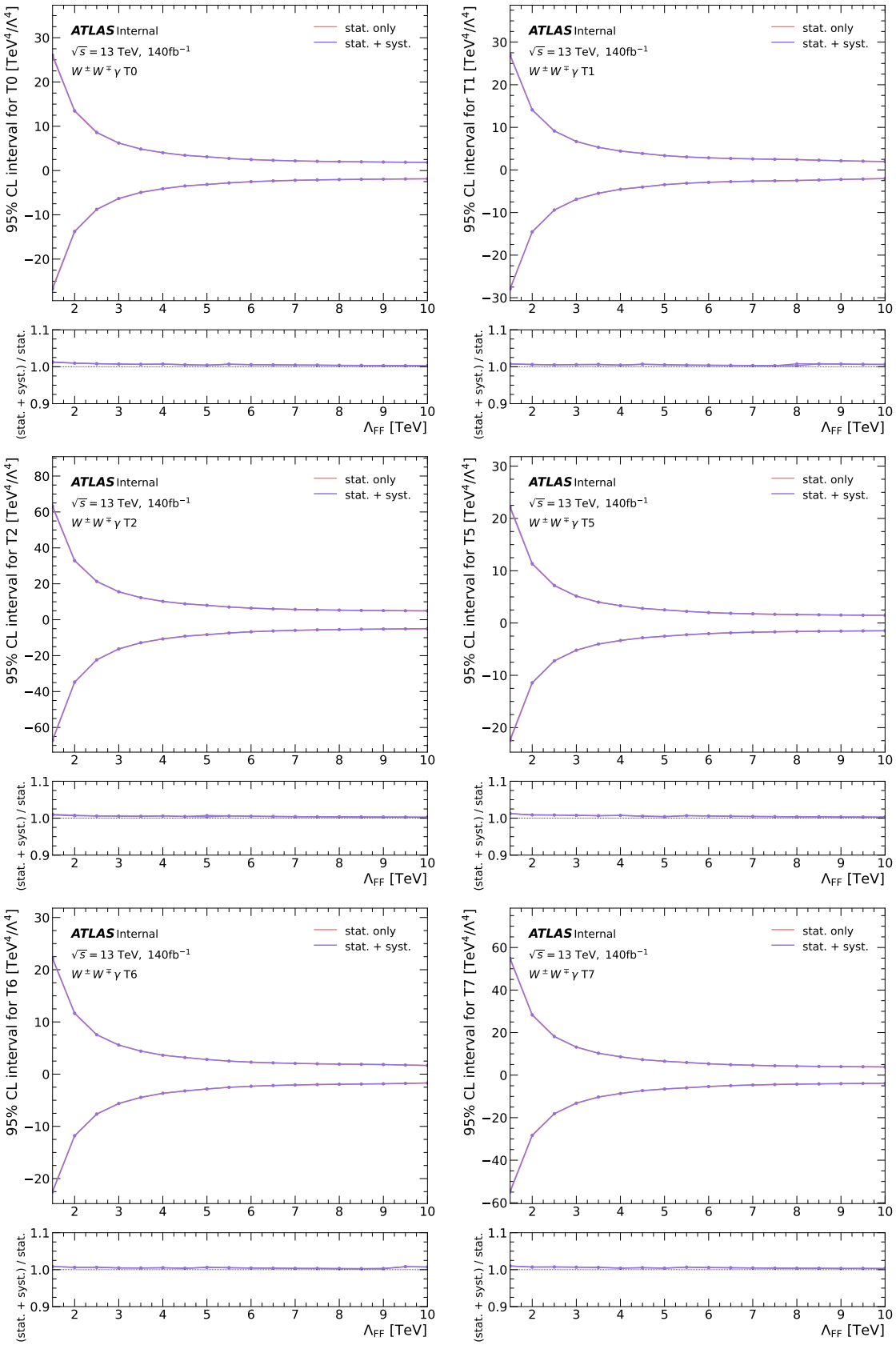

Figure 6.33: 95% CL upper and lower expected limits on Wilson coefficients vs. Λ_{FF}.

Chapter 7

Conclusion

This thesis presented a search for evidence of $W^{\pm}W^{\mp}\gamma$ production in $p-p$ collisions at $\sqrt{s}$ = 13 TeV at the LHC, using data recorded by the ATLAS experiment during LHC run-2 with 140 fb^{-1} of integrated luminosity. The search was done by analyzing events in which an opposite-charge electron-muon pair were detected along with a photon, with various event selection criteria applied in order to obtain as pure a dataset of $W^{\pm}W^{\mp}\gamma$ events as possible. MC simulations along with data-driven estimates of the expected backgrounds in the $e^{\pm}\mu^{\mp}\gamma$ channel estimate the dataset contains about 26% $W^{\pm}W^{\mp}\gamma$ signal and about 74% background, which are further separated with a machine learning algorithm trained on MC simulations. A maximum likelihood fit was performed on the output of the machine learning algorithm to determine the best-fit value of the $W^{\pm}W^{\mp}\gamma$ signal contribution to the $e^{\pm}\mu^{\mp}\gamma$ channel, as well as various nuisance parameters quantifying the background contributions and sources of systematic uncertainty. The expected cross section in the fiducial region is $10.5^{+23\%}_{-19\%}$ fb, with the experimental uncertainty dominated by statistical uncertainty. The CMS collaboration, ATLAS's sister experiment on the LHC, recently published a discovery of $W^{\pm}W^{\mp}\gamma$ production[129] using LHC run-2 data. They report an observed fiducial cross section of 6.0 $\pm$ 28% fb, with a different fiducial region definition than our $W^{\pm}W^{\mp}\gamma$ analysis. It is worth noting that they did not observe any significant deviation from the SM prediction.

Additionally, the run-2 data is used to set upper and lower expected limits at the 95% CL on 13 Wilson coefficients corresponding to 13 dimension-8 operators of an effective field theory extension of the Standard Model. These limits are presented in Table 6.2. Two methods were

used to restore unitarity to the EFT model, and the dependence of the Wilson coefficient expected upper and lower limits at the 95% CL on the two models' parameters are presented. This analysis is the first by the ATLAS experiment to present limits on dimension-8 Wilson coefficients with LHC run-2 data.

The only remaining step in the analysis is to unblind data in the $e^{\pm}\mu^{\mp}\gamma$ signal region, pending approval by the ATLAS collaboration, and re-run the fits to derive the observed fiducial cross section and observed upper and lower limits at the 95% CL on the 13 Wilson coefficients. These results will be published in the coming months in a paper currently in preparation. LHC run-3 is currently ongoing at $\sqrt{s} = 13$ TeV, and the ATLAS experiment is currently collecting data. In the future, the $W^{\pm}W^{\mp}\gamma$ analysis could be repeated using the run-3 dataset to tighten the uncertainties on this measurement and tighten the limits on EFT Wilson coefficients. Looking ahead further into the future, LHC run-4 is expected to begin in 2029 with the LHC upgraded to deliver much higher luminosity along with upgrades to the ATLAS detector to accommodate the increased pileup. While it is not clear whether further analysis of $W^{\pm}W^{\mp}\gamma$ production will yield any hints of physics beyond the Standard Model, it will remain an interesting channel to study the non-Abelian gauge structure of the SM.

Author's contributions

The ATLAS collaboration is a highly collective environment in which many people work together to contribute to common efforts. The contributions of Daniel Wilbern, the author of this thesis, to the $W^{\pm}W^{\mp}\gamma$ analysis include:

- Contributed to the software development effort for the $W^{\pm}W^{\mp}\gamma$ analysis
- Data processing on distributed computing systems
- Helped with the optimization of SR and CR definitions
- The $e \to \gamma$ fake estimate of Section 5.1.2
- Generation of $W^{\pm}W^{\mp}\gamma$ aQGC MC samples with MadGraph+Pythia
- Most of the aQGC analysis of Chapter 6

References

[1] ATLAS Collaboration, *Observation of a new particle in the search for the Standard Model Higgs boson with the ATLAS detector at the LHC*, Phys. Lett. B **716** (2012) 1, arXiv:1207.7214 [hep-ex]. 2.1

[2] CMS Collaboration, *A New Boson with a Mass of* 125 *GeV Observed with the CMS Experiment at the Large Hadron Collider*, Science **338** (2012) 1569–1575. 2.1

[3] Wikipedia, *Standard Model — Wikipedia, The Free Encyclopedia*, http://en.wikipedia.org/w/index.php?title=Standard%20Model, 2023. [Online; accessed 24-April-2023]. 2.1

[4] M. D. Schwartz, *Quantum Field Theory and the Standard Model*. Cambridge University Press, 3, 2014. 2.1

[5] E. P. Wigner, *On Unitary Representations of the Inhomogeneous Lorentz Group*, Annals Math. **40** (1939) 149–204. 2.1

[6] S. L. Glashow, *Partial Symmetries of Weak Interactions*, Nucl. Phys. **22** (1961) 579–588. 2.1, 2.2

[7] J. Goldstone, A. Salam, and S. Weinberg, *Broken Symmetries*, Phys. Rev. **127** (1962) 965–970. 2.1, 2.2

[8] S. Weinberg, *A Model of Leptons*, Phys. Rev. Lett. **19** (1967) 1264–1266. 2.1, 2.2

[9] C. N. Yang and R. L. Mills, *Conservation of Isotopic Spin and Isotopic Gauge Invariance*, Phys. Rev. **96** (1954) 191–195, https://link.aps.org/doi/10.1103/PhysRev.96.191. 2.1

[10] P. W. Higgs, *Broken Symmetries and the Masses of Gauge Bosons*, Phys. Rev. Lett. **13** (1964) 508–509. 2.1

[11] ATLAS Collaboration,, *Standard Model Summary Plots February 2022*,. 2.3

[12] E. Fermi, *An attempt of a theory of beta radiation. 1.*, Z. Phys. **88** (1934) 161–177. 2.2

[13] Particle Data Group Collaboration, R. L. Workman et al., *Review of Particle Physics*, PTEP **2022** (2022) 083C01. 2.2, 4.1.5, 4.2, 5.1.2

[14] R. P. Feynman and M. Gell-Mann, *Theory of the Fermi Interaction*, Phys. Rev. **109** (1958) 193–198, https://link.aps.org/doi/10.1103/PhysRev.109.193. 2.2

[15] C. Degrande, N. Greiner, W. Kilian, O. Mattelaer, H. Mebane, T. Stelzer, S. Willenbrock, and C. Zhang, *Effective Field Theory: A Modern Approach to Anomalous Couplings*, Annals Phys. **335** (2013) 21–32, arXiv:1205.4231 [hep-ph]. 2.2

[16] ATLAS Collaboration, *$ZZ \to \ell^+\ell^-\ell'^+\ell'^-$ cross-section measurements and search for anomalous triple gauge couplings in 13 TeV pp collisions with the ATLAS detector*, Phys. Rev. D **97** (2018) 032005, arXiv:1709.07703 [hep-ex]. 2.2

[17] ATLAS Collaboration, *Measurement of ZZ production in the $\ell\ell\nu\nu$ final state with the ATLAS detector in pp collisions at $\sqrt{s} = 13$ TeV*, JHEP **10** (2019) 127, arXiv:1905.07163 [hep-ex]. 2.2

[18] ATLAS Collaboration, *Measurement of the $Z\gamma \to \nu\bar{\nu}\gamma$ production cross section in pp collisions at $\sqrt{s} = 13$ TeV with the ATLAS detector and limits on anomalous triple gauge-boson couplings*, JHEP **12** (2018) 010, arXiv:1810.04995 [hep-ex]. 2.2

[19] ATLAS Collaboration, *Measurement of fiducial and differential W^+W^- production cross-sections at $\sqrt{s} = 13$ TeV with the ATLAS detector*, Eur. Phys. J. C **79** (2019) 884, arXiv:1905.04242 [hep-ex]. 2.2

[20] CMS Collaboration, *Measurements of the $pp \to ZZ$ production cross section and the $Z \to 4\ell$ branching fraction, and constraints on anomalous triple gauge couplings at $\sqrt{s} = 13$ TeV*, Eur. Phys. J. C **78** (2018) 165, arXiv:1709.08601 [hep-ex]. 2.2

[21] CMS Collaboration, *Electroweak production of two jets in association with a Z boson in proton–proton collisions at $\sqrt{s} = 13$ TeV*, Eur. Phys. J. C **78** (2018) 589, arXiv:1712.09814 [hep-ex]. 2.2

[22] CMS Collaboration, *Measurement of electroweak production of a W boson in association with two jets in proton–proton collisions at $\sqrt{s} = 13$ TeV*, Eur. Phys. J. C **80** (2020) 43, arXiv:1903.04040 [hep-ex]. 2.2

[23] CMS Collaboration, *Measurements of the $pp \to WZ$ inclusive and differential production cross section and constraints on charged anomalous triple gauge couplings at $\sqrt{s} = 13$ TeV*, JHEP **04** (2019) 122, arXiv:1901.03428 [hep-ex]. 2.2

[24] CMS Collaboration, *W^+W^- boson pair production in proton–proton collisions at $\sqrt{s} = 13$ TeV*, Phys. Rev. D **102** (2020) 092001, arXiv:2009.00119 [hep-ex]. 2.2

[25] CMS Collaboration, *Search for anomalous triple gauge couplings in WW and WZ production in lepton + jet events in proton–proton collisions at $\sqrt{s} = 13$ TeV*, JHEP **12** (2019) 062, arXiv:1907.08354 [hep-ex]. 2.2

[26] CMS Collaboration, *Measurements of $pp \to ZZ$ production cross sections and constraints on anomalous triple gauge couplings at $\sqrt{s} = 13$ TeV*, Eur. Phys. J. C **81** (2021) 200, arXiv:2009.01186 [hep-ex]. 2.2

[27] CMS Collaboration, *Search for the production of $W^\pm W^\pm W^\mp$ events at $\sqrt{s} = 13$ TeV*, Phys. Rev. D **100** (2019) 012004, arXiv:1905.04246 [hep-ex]. 2.2

[28] CMS Collaboration, *Search for anomalous electroweak production of vector boson pairs in association with two jets in proton–proton collisions at 13 TeV*, Phys. Lett. B **798** (2019) 134985, arXiv:1905.07445 [hep-ex]. 2.2, ??, ??, ??, ??, ??

[29] CMS Collaboration, *Measurements of production cross sections of WZ and same-sign WW boson pairs in association with two jets in proton–proton collisions at $\sqrt{s} = 13$ TeV*, Phys. Lett. B **809** (2020) 135710, arXiv:2005.01173 [hep-ex]. 2.2

[30] CMS Collaboration, *Evidence for electroweak production of four charged leptons and two jets in proton–proton collisions at $\sqrt{s} = 13$ TeV*, Phys. Lett. B **812** (2021) 135992, arXiv:2008.07013 [hep-ex]. 2.2

[31] CMS Collaboration, *Measurement of the electroweak production of $Z\gamma$ and two jets in proton–proton collisions at $\sqrt{s} = 13$ TeV and constraints on anomalous quartic gauge couplings*, Phys. Rev. D **104** (2021) 072001, arXiv:2106.11082 [hep-ex]. 2.2

[32] CMS Collaboration, *Measurement of the electroweak production of $W\gamma$ in association with two jets in proton–proton collisions at $\sqrt{s} = 13$ TeV*, arXiv:2212.12592 [hep-ex]. 2.2, ??, ??, ??, ??, ??, ??, ??, ??

[33] ATLAS Collaboration, *Measurements of $Z\gamma$ and $Z\gamma\gamma$ production in pp collisions at $\sqrt{s} = 8$ TeV with the ATLAS detector*, Phys. Rev. D **93** (2016) 112002, arXiv:1604.05232 [hep-ex]. 2.2

[34] ATLAS Collaboration, *Measurements of $W^{\pm}Z$ production cross sections in pp collisions at $\sqrt{s} = 8$ TeV with the ATLAS detector and limits on anomalous gauge boson self-couplings*, Phys. Rev. D **93** (2016) 092004, arXiv:1603.02151 [hep-ex]. 2.2

[35] ATLAS Collaboration, *Measurement of $W^{\pm}W^{\pm}$ vector-boson scattering and limits on anomalous quartic gauge couplings with the ATLAS detector*, Phys. Rev. D **96** (2017) 012007, arXiv:1611.02428 [hep-ex]. 2.2

[36] ATLAS Collaboration, *Search for triboson $W^{\pm}W^{\pm}W^{\mp}$ production in pp collisions at $\sqrt{s} = 8$ TeV with the ATLAS detector*, Eur. Phys. J. C **77** (2017) 141, arXiv:1610.05088 [hep-ex]. 2.2

[37] ATLAS Collaboration, *Search for anomalous electroweak production of WW/WZ in association with a high-mass dijet system in pp collisions at $\sqrt{s} = 8$ TeV with the ATLAS detector*, Phys. Rev. D **95** (2017) 032001, arXiv:1609.05122 [hep-ex]. 2.2

[38] ATLAS Collaboration, *Measurement of exclusive $\gamma\gamma \to W^{+}W^{-}$ production and search for exclusive Higgs boson production in pp collisions at $\sqrt{s} = 8$ TeV using the ATLAS detector*, Phys. Rev. D **94** (2016) 032011, arXiv:1607.03745 [hep-ex]. 2.2

[39] ATLAS Collaboration, *Study of $WW\gamma$ and $WZ\gamma$ production in pp collisions at $\sqrt{s} = 8$ TeV and search for anomalous quartic gauge couplings with the ATLAS experiment*, Eur. Phys. J. C **77** (2017) 646, arXiv:1707.05597 [hep-ex]. 2.2, ??

[40] CMS Collaboration, *A search for $WW\gamma$ and $WZ\gamma$ production and constraints on anomalous quartic gauge couplings in pp collisions at $\sqrt{s} = 8$ TeV*, Phys. Rev. D **90** (2014) 032008, arXiv:1404.4619 [hep-ex]. 2.2

[41] CMS Collaboration, *Study of vector boson scattering and search for new physics in events with two same-sign leptons and two jets*, Phys. Rev. Lett. **114** (2015) 051801, arXiv:1410.6315 [hep-ex]. 2.2

[42] CMS Collaboration, *Measurement of electroweak-induced production of $W\gamma$ with two jets in pp collisions at $\sqrt{s} = 8$ TeV and constraints on anomalous quartic gauge couplings*, JHEP **06** (2017) 106, arXiv:1612.09256 [hep-ex]. 2.2

[43] CMS Collaboration, *Measurement of the cross section for electroweak production of $Z\gamma$ in association with two jets and constraints on anomalous quartic gauge couplings in proton–proton collisions at $\sqrt{s} = 8$ TeV*, Phys. Lett. B **770** (2017) 380, arXiv:1702.03025 [hep-ex]. 2.2

[44] CMS Collaboration, *Measurements of the $pp \to W\gamma\gamma$ and $pp \to Z\gamma\gamma$ cross sections and limits on anomalous quartic gauge couplings at $\sqrt{s} = 8$ TeV*, JHEP **10** (2017) 072, arXiv:1704.00366 [hep-ex]. 2.2

[45] O. J. P. Éboli and M. C. Gonzalez-Garcia, *Classifying the bosonic quartic couplings*, Phys. Rev. D **93** (2016) 093013, arXiv:1604.03555 [hep-ph]. 2.2, 4.3

[46] E. d. S. Almeida, O. J. P. Éboli, and M. C. Gonzalez–Garcia, *Unitarity constraints on anomalous quartic couplings*, Phys. Rev. D **101** (2020) 113003, arXiv:2004.05174 [hep-ph]. 2.2, 2.2, 2.1

[47] ATLAS Collaboration,, *ATLAS: A 25-Year Insider Story of the LHC Experiment*. World Scientific, 2019. 3

[48] *LHC Machine*, JINST **3** (2008) S08001. 3.1

[49] E. Mobs, *The CERN accelerator complex. Complexe des accélérateurs du CERN*, https://cds.cern.ch/record/2197559, General Photo. 3.1

[50] *Public atlas luminosity results for run-2 of the LHC*, https://twiki.cern.ch/twiki/bin/view/AtlasPublic/LuminosityPublicResultsRun2. 3.2, 3.3

[51] J. Pequenao, *Computer generated image of the whole ATLAS detector*, 2008. 3.4, 3.6

[52] ATLAS Collaboration, G. Aad et al., *The ATLAS Experiment at the CERN Large Hadron Collider*, JINST **3** (2008) S08003. 3.2, 3.8

[53] CMS Collaboration, D. Barney, *CMS Slice*, https://cds.cern.ch/record/2628641. 3.5

[54] ATLAS Collaboration,, *ATLAS Fact Sheet : To raise awareness of the ATLAS detector and collaboration on the LHC*, 2010. 3.2.1

[55] ATLAS Collaboration, A. R. Martínez, *The Run-2 ATLAS Trigger System*, J. Phys. Conf. Ser. **762** (2016) 012003. 3.2.1

[56] ATLAS Collaboration, M. Capeans, G. Darbo, K. Einsweiller, M. Elsing, T. Flick, M. Garcia-Sciveres, C. Gemme, H. Pernegger, O. Rohne, and R. Vuillermet, *ATLAS Insertable B-Layer Technical Design Report*, tech. rep., 2010. https://cds.cern.ch/record/1291633. 3.2.2

[57] ATLAS Collaboration,, *Technical Design Report for the ATLAS Inner Tracker Strip Detector*, tech. rep., CERN, Geneva, 2017. https://cds.cern.ch/record/2257755. 3.2.2

[58] M. Brice, *Installing the ATLAS calorimeter. Vue centrale du détecteur ATLAS avec ses huit toroides entourant le calorimètre avant son déplacement au centre du détecteur*, 2005. 3.7

[59] ATLAS Collaboration,, *ATLAS magnet system: Technical Design Report, 1*. Technical design report. ATLAS. CERN, Geneva, 1997. https://cds.cern.ch/record/338080. 3.2.4

[60] T. A. Collaboration, *ATLAS Event Displays Repository*, https://atlaspo.cern.ch/public/event_display/, 2023. [Online; accessed 24-April-2023]. 4.1

[61] ATLAS Collaboration, *Performance of the ATLAS track reconstruction algorithms in dense environments in LHC Run 2*, Eur. Phys. J. C **77** (2017) 673, arXiv:1704.07983 [hep-ex]. 4.1.1

[62] ATLAS Collaboration, *Training and validation of the ATLAS pixel clustering neural networks*, ATL-PHYS-PUB-2018-002, 2018, https://cds.cern.ch/record/2309474. 4.1.1

[63] R. Frühwirth, *Application of Kalman filtering to track and vertex fitting*, Nuclear Instruments and Methods in Physics Research Section A: Accelerators, Spectrometers, Detectors and Associated Equipment **262** (1987) 444–450, https://www.sciencedirect.com/science/article/pii/0168900287908874. 4.1.1

[64] ATLAS Collaboration, *Early Inner Detector Tracking Performance in the 2015 Data at* $\sqrt{s} = 13$ *TeV*, ATL-PHYS-PUB-2015-051, 2015, https://cds.cern.ch/record/2110140. 4.2

[65] ATLAS Collaboration, *Vertex Reconstruction Performance of the ATLAS Detector at* $\sqrt{s} = 13$ *TeV*, ATL-PHYS-PUB-2015-026, 2015, https://cds.cern.ch/record/2037717. 4.2

[66] ATLAS Collaboration, *Reconstruction of primary vertices at the ATLAS experiment in Run 1 proton–proton collisions at the LHC*, Eur. Phys. J. C **77** (2017) 332, arXiv:1611.10235 [hep-ex]. 4.1.1

[67] W. Lampl et al., *Calorimeter Clustering Algorithms: Description and Performance*, ATL-LARG-PUB-2008-002, 2008, https://cds.cern.ch/record/1099735. 4.1.2

[68] ATLAS Collaboration, *Topological cell clustering in the ATLAS calorimeters and its performance in LHC Run 1*, Eur. Phys. J. C **77** (2017) 490, arXiv:1603.02934 [hep-ex]. 4.1.2, 4.3

[69] ATLAS Collaboration, *Electron reconstruction and identification in the ATLAS experiment using the 2015 and 2016 LHC proton–proton collision data at* $\sqrt{s} = 13$ *TeV*, Eur. Phys. J. C **79** (2019) 639, arXiv:1902.04655 [hep-ex]. 4.1.3

[70] ATLAS Collaboration, *Electron and photon performance measurements with the ATLAS detector using the 2015–2017 LHC proton–proton collision data*, JINST **14** (2019) P12006, arXiv:1908.00005 [hep-ex]. 4.1.3, 4.4, 4.5, 4.6

[71] ATLAS Collaboration, *Improved electron reconstruction in ATLAS using the Gaussian Sum Filter-based model for bremsstrahlung*, ATLAS-CONF-2012-047, 2012, https://cds.cern.ch/record/1449796. 4.1.3

[72] ATLAS Collaboration, *Electron and photon energy calibration with the ATLAS detector using 2015–2016 LHC proton–proton collision data*, JINST **14** (2019) P03017, arXiv:1812.03848 [hep-ex]. 4.1.3

[73] ATLAS Collaboration, *Muon reconstruction and identification efficiency in ATLAS using the full Run 2 pp collision data set at* $\sqrt{s} = 13$ *TeV*, Eur. Phys. J. C **81** (2021) 578, arXiv:2012.00578 [hep-ex]. 4.1.4

[74] ATLAS Collaboration, *Muon reconstruction performance of the ATLAS detector in proton–proton collision data at* $\sqrt{s} = 13$ *TeV*, Eur. Phys. J. C **76** (2016) 292, arXiv:1603.05598 [hep-ex]. 4.7

[75] ATLAS Collaboration, *Jet reconstruction and performance using particle flow with the ATLAS Detector*, Eur. Phys. J. C **77** (2017) 466, arXiv:1703.10485 [hep-ex]. 4.1.5, 4.8

[76] M. Cacciari, G. P. Salam, and G. Soyez, *The anti-*k_t *jet clustering algorithm*, JHEP **04** (2008) 063, arXiv:0802.1189 [hep-ph]. 4.1.5

[77] ATLAS Collaboration, *Jet energy scale and resolution measured in proton–proton collisions at* $\sqrt{s} = 13$ *TeV with the ATLAS detector*, Eur. Phys. J. C **81** (2020) 689, arXiv:2007.02645 [hep-ex]. 4.1.5

[78] ATLAS Collaboration, *Tagging and suppression of pileup jets with the ATLAS detector*, ATLAS-CONF-2014-018, 2014, https://cds.cern.ch/record/1700870. 4.1.5

[79] ATLAS Collaboration, *ATLAS flavour-tagging algorithms for the LHC Run 2 pp collision dataset*, arXiv:2211.16345 [physics.data-an]. 4.1.5, 4.8

[80] ATLAS Collaboration, E_T^{miss} *performance in the ATLAS detector using 2015–2016 LHC pp collisions*, ATLAS-CONF-2018-023, 2018, https://cds.cern.ch/record/2625233. 4.1.6

[81] ATLAS Collaboration, *Performance of missing transverse momentum reconstruction with the ATLAS detector using proton–proton collisions at* $\sqrt{s} = 13$ *TeV*, Eur. Phys. J. C **78** (2018) 903, arXiv:1802.08168 [hep-ex]. 4.9

[82] GEANT4 Collaboration, S. Agostinelli, et al., *GEANT4 – a simulation toolkit*, Nucl. Instrum. Meth. A **506** (2003) 250. 4.3

[83] ATLAS Collaboration, *The ATLAS Simulation Infrastructure*, Eur. Phys. J. C **70** (2010) 823, arXiv:1005.4568 [physics.ins-det]. 4.3

[84] T. Sjöstrand, S. Mrenna, and P. Skands, *A brief introduction to PYTHIA 8.1*, Comput. Phys. Commun. **178** (2008) 852–867, arXiv:0710.3820 [hep-ph]. 4.3, 4.3, 4.3, 4.3

[85] ATLAS Collaboration, *The Pythia 8 A3 tune description of ATLAS minimum bias and inelastic measurements incorporating the Donnachie–Landshoff diffractive model*, ATL-PHYS-PUB-2016-017, 2016, https://cds.cern.ch/record/2206965. 4.3

[86] ATLAS Collaboration, *Luminosity determination in pp collisions at* $\sqrt{s} = 13$ *TeV using the ATLAS detector at the LHC*, arXiv:2212.09379 [hep-ex]. 4.3

[87] ATLAS Collaboration, *Performance of the ATLAS trigger system in 2015*, Eur. Phys. J. C **77** (2017) 317, arXiv:1611.09661 [hep-ex]. 4.3

[88] ATLAS Collaboration, *Performance of electron and photon triggers in ATLAS during LHC Run 2*, Eur. Phys. J. C **80** (2020) 47, arXiv:1909.00761 [hep-ex]. 4.3

[89] ATLAS Collaboration, *Performance of the ATLAS muon triggers in Run 2*, JINST **15** (2020) P09015, arXiv:2004.13447 [hep-ex]. 4.3

[90] ATLAS Collaboration, *ATLAS data quality operations and performance for 2015–2018 data-taking*, JINST **15** (2020) P04003, arXiv:1911.04632 [physics.ins-det]. 4.3

[91] ATLAS Collaboration, *Selection of jets produced in* 13 *TeV proton–proton collisions with the ATLAS detector*, ATLAS-CONF-2015-029, 2015, https://cds.cern.ch/record/2037702. 4.3

[92] E. Bothmann et al., *Event generation with Sherpa 2.2*, SciPost Phys. **7** (2019) 034, arXiv:1905.09127 [hep-ph]. 4.3, 4.3, 4.3, 4.3, 4.3

[93] NNPDF Collaboration, R. D. Ball et al., *Parton distributions for the LHC run II*, JHEP **04** (2015) 040, arXiv:1410.8849 [hep-ph]. 4.3, 4.3, 4.3, 4.3, 4.3, 4.3, 4.3, 4.3

[94] T. Gleisberg and S. Höche, *Comix, a new matrix element generator*, JHEP **12** (2008) 039, arXiv:0808.3674 [hep-ph]. 4.3, 4.3, 4.3, 4.3, 4.3

[95] F. Buccioni, J.-N. Lang, J. M. Lindert, P. Maierhöfer, S. Pozzorini, H. Zhang, and M. F. Zoller, *OpenLoops 2*, Eur. Phys. J. C **79** (2019) 866, arXiv:1907.13071 [hep-ph]. 4.3, 4.3, 4.3, 4.3, 4.3

[96] F. Cascioli, P. Maierhöfer, and S. Pozzorini, *Scattering Amplitudes with Open Loops*, Phys. Rev. Lett. **108** (2012) 111601, arXiv:1111.5206 [hep-ph]. 4.3, 4.3, 4.3, 4.3, 4.3

[97] A. Denner, S. Dittmaier, and L. Hofer, *COLLIER: A fortran-based complex one-loop library in extended regularizations*, Comput. Phys. Commun. **212** (2017) 220–238, arXiv:1604.06792 [hep-ph]. 4.3, 4.3, 4.3, 4.3, 4.3

[98] S. Schumann and F. Krauss, *A parton shower algorithm based on Catani–Seymour dipole factorisation*, JHEP **03** (2008) 038, arXiv:0709.1027 [hep-ph]. 4.3, 4.3, 4.3, 4.3, 4.3

[99] S. Höche, F. Krauss, M. Schönherr, and F. Siegert, *A critical appraisal of NLO+PS matching methods*, JHEP **09** (2012) 049, arXiv:1111.1220 [hep-ph]. 4.3, 4.3, 4.3, 4.3, 4.3

[100] S. Höche, F. Krauss, M. Schönherr, and F. Siegert, *QCD matrix elements + parton showers. The NLO case*, JHEP **04** (2013) 027, arXiv:1207.5030 [hep-ph]. 4.3, 4.3, 4.3, 4.3, 4.3

[101] S. Catani, F. Krauss, B. R. Webber, and R. Kuhn, *QCD Matrix Elements + Parton Showers*, JHEP **11** (2001) 063, arXiv:hep-ph/0109231. 4.3, 4.3, 4.3, 4.3, 4.3

[102] S. Höche, F. Krauss, S. Schumann, and F. Siegert, *QCD matrix elements and truncated showers*, JHEP **05** (2009) 053, arXiv:0903.1219 [hep-ph]. 4.3, 4.3, 4.3, 4.3, 4.3

[103] J. Alwall, R. Frederix, S. Frixione, V. Hirschi, F. Maltoni, O. Mattelaer, H. S. Shao, T. Stelzer, P. Torrielli, and M. Zaro, *The automated computation of tree-level and next-to-leading order differential cross sections, and their matching to parton shower simulations*, JHEP **07** (2014) 079, arXiv:1405.0301 [hep-ph]. 4.3, 4.3

[104] O. Eboli and M. Gonzalez-Garcia, *Anomalous Gauge Coupling*, https://feynrules.irmp.ucl.ac.be/wiki/AnomalousGaugeCoupling, Accessed 2023-03-31. 4.3

[105] ATLAS Collaboration, *ATLAS Pythia 8 tunes to 7 TeV data*, ATL-PHYS-PUB-2014-021, 2014, https://cds.cern.ch/record/1966419. 4.3, 4.3

[106] P. Artoisenet, R. Frederix, O. Mattelaer, and R. Rietkerk, *Automatic spin-entangled decays of heavy resonances in Monte Carlo simulations*, JHEP **03** (2013) 015, arXiv:1212.3460 [hep-ph]. 4.3

[107] D. J. Lange, *The EvtGen particle decay simulation package*, Nuclear Instruments and Methods in Physics Research Section A: Accelerators, Spectrometers, Detectors and Associated Equipment **462** (2001) 152–155, BEAUTY2000, Proceedings of the 7th Int. Conf. on B-Physics at Hadron Machines. 4.3, 4.3

[108] S. Dulat, T.-J. Hou, J. Gao, M. Guzzi, J. Huston, P. Nadolsky, J. Pumplin, C. Schmidt, D. Stump, and C. P. Yuan, *New parton distribution functions from a global analysis of quantum chromodynamics*, Phys. Rev. D **93** (2016) 033006, arXiv:1506.07443 [hep-ph]. 4.3

[109] P. Nason, *A new method for combining NLO QCD with shower Monte Carlo algorithms*, JHEP **11** (2004) 040, arXiv:hep-ph/0409146. 4.3

[110] S. Frixione, P. Nason, and C. Oleari, *Matching NLO QCD computations with parton shower simulations: the POWHEG method*, JHEP **11** (2007) 070, arXiv:0709.2092 [hep-ph]. 4.3

[111] S. Alioli, P. Nason, C. Oleari, and E. Re, *A general framework for implementing NLO calculations in shower Monte Carlo programs: the POWHEG BOX*, JHEP **06** (2010) 043, arXiv:1002.2581 [hep-ph]. 4.3

[112] S. Frixione, G. Ridolfi, and P. Nason, *A positive-weight next-to-leading-order Monte Carlo for heavy flavour hadroproduction*, JHEP **09** (2007) 126, arXiv:0707.3088 [hep-ph]. 4.3

[113] R. D. Ball et al., *Parton distributions with LHC data*, Nucl. Phys. B **867** (2013) 244, arXiv:1207.1303 [hep-ph]. 4.3

[114] E. Re, *Single-top Wt-channel production matched with parton showers using the POWHEG method*, Eur. Phys. J. C **71** (2011) 1547, arXiv:1009.2450 [hep-ph]. 4.3

[115] S. Frixione, E. Laenen, P. Motylinski, C. White, and B. R. Webber, *Single-top hadroproduction in association with a W boson*, JHEP **07** (2008) 029, arXiv:0805.3067 [hep-ph]. 4.3

[116] C. Anastasiou, L. Dixon, K. Melnikov, and F. Petriello, *High-precision QCD at hadron colliders: Electroweak gauge boson rapidity distributions at next-to-next-to leading order*, Phys. Rev. D **69** (2004) 094008, arXiv:hep-ph/0312266. 4.3

[117] T. Chen and C. Guestrin, *XGBoost: A Scalable Tree Boosting System*, http://doi.acm.org/10.1145/2939672.2939785. 5.2

[118] C. M. Bishop, *Pattern Recognition and Machine Learning (Information Science and Statistics)*. Springer-Verlag, Berlin, Heidelberg, 2006. 5.6

[119] HEP Software Foundation Collaboration, J. Apostolakis et al., *HEP Software Foundation Community White Paper Working Group - Detector Simulation*, arXiv:1803.04165 [physics.comp-ph]. 5.2

[120] ATLAS Collaboration,, *Search for third-generation vector-like leptons in pp collisions at $\sqrt{s} = 13$ TeV with the ATLAS detector*, arXiv:2303.05441 [hep-ex]. 5.2

[121] ROOT Collaboration, K. Cranmer, G. Lewis, L. Moneta, A. Shibata, and W. Verkerke, *HistFactory: A tool for creating statistical models for use with RooFit and RooStats*, tech. rep., New York U., New York, 2012. https://cds.cern.ch/record/1456844. 5.3

[122] L. Moneta, K. Belasco, K. Cranmer, S. Kreiss, A. Lazzaro, D. Piparo, G. Schott, W. Verkerke, and M. Wolf, *The RooStats Project*, 2011. 5.3

[123] W. Verkerke and D. Kirkby, *The RooFit toolkit for data modeling*, 2003, arXiv:physics/0306116 [physics.data-an]. 5.3

[124] R. Brun and F. Rademakers, *ROOT – An object oriented data analysis framework*, Nucl. Instrum. Meth. A **389** (1997) 81 – 86. 5.3

[125] G. Cowan, K. Cranmer, E. Gross, and O. Vitells, *Asymptotic formulae for likelihood-based tests of new physics*, Eur. Phys. J. C **71** (2011) 1554, arXiv:1007.1727 [physics.data-an]. 5.3

[126] C. Bierlich et al., *Robust Independent Validation of Experiment and Theory: Rivet version 3*, SciPost Phys. **8** (2020) 026, arXiv:1912.05451 [hep-ph]. 5.3.3

[127] S. S. Wilks, *The Large-Sample Distribution of the Likelihood Ratio for Testing Composite Hypotheses*, The Annals of Mathematical Statistics **9** (1938) 60 – 62, https://doi.org/10.1214/aoms/1177732360. 6.3

[128] O. J. P. Eboli, M. C. Gonzalez-Garcia, and S. M. Lietti, *Bosonic quartic couplings at CERN LHC*, Phys. Rev. D **69** (2004) 095005, arXiv:hep-ph/0310141. 6.4

[129] CMS Collaboration,, *Observation of $WW\gamma$ production and constraints on Higgs couplings to light quarks in proton-proton collisions at $\sqrt{s} = 13$ TeV*, tech. rep., CERN, Geneva, 2023. https://cds.cern.ch/record/2853299. 7